Summer 8-2022

Investigation of Transport Behavior in Two-Dimensional Ferroelectric Heterostructures

Pradeep Chaudhary
University of Nebraska-Lincoln, pradeep.chaudhary@huskers.unl.edu

---

Chaudhary, Pradeep, "Investigation of Transport Behavior in Two-Dimensional Ferroelectric Heterostructures" (2022). *Theses, Dissertations, and Student Research: Department of Physics and Astronomy*. 60.
https://digitalcommons.unl.edu/physicsdiss/60

INVESTIGATION OF TRANSPORT BEHAVIOR IN TWO-DIMENSIONAL FERROELECTRIC HETEROSTRUCTURES

by

Pradeep Chaudhary

A DISSERTATION

Presented to the Faculty of
The Graduate College at the University of Nebraska
In Partial Fulfillment of Requirements
For the Degree of Doctor of Philosophy

Major: Physics and Astronomy
Under the Supervision of Professor Alexei Gruverman

Lincoln, Nebraska

August 2022

INVESTIGATION OF TRANSPORT BEHAVIOR IN TWO-DIMENSIONAL FERROELECTRIC HETEROSTRUCTURES

Pradeep Chaudhary, Ph. D.

University of Nebraska, 2022

Advisor: Alexei Gruverman

This dissertation summarizes an investigation of the polarization-related electronic transport behavior in the ferroelectric thin films and two-dimensional (2D) materials heterostructures using Scanning Probe Microscopy (SPM) techniques.

The polarization-related resistive switching in hafnium oxide thin films-based ferroelectric tunnel junction has been demonstrated by employing semiconducting MoS_2 as a top electrode. We explored a coupling between the semiconducting properties of MoS_2 and the polarization of $Hf_{0.5}Zr_{0.5}O_2$ resulted in an enhanced tunneling electroresistance effect of up to 3 orders of magnitude. These results provide a possible pathway for the fabrication of high-density non-volatile memory devices. These results are presented in Chapter 3.

Resistive switching control using conducting domain walls as functional elements has been investigated using graphene/$LiNbO_3$ heterostructures. One approach involves the modulation of resistance through the manipulation of domain wall density using super-coercive voltage. This approach requires higher energy to switch the polarization and can induce high leakage current that makes it deleterious. To overcome this drawback, we have developed a new approach that involves tuning of domain wall conductivity by a sub-

coercive voltage without altering the domain configuration. These results are presented in Chapter 4.

Chapter 5 describes modulation of the transport behavior of 2D MoS_2 junctions by mechanical stress induced by the sharp probe of atomic force microscope (AFM). We show that the junction resistance can be reversibly tuned by up to 4 orders of magnitude by altering the mechanical force applied via AFM tip. Additionally, we show that AFM tip generates strain gradient inducing flexoelectric effect that leads to an enhancement of photovoltaic effect.

Finally, we have discovered stable room temperature ferroelectricity with out-of-plane polarization in trigonally distorted 1T”-MoS_2. Here, the polarization switching has been realized by the mechanical load applied via AFM probe. The piezoelectric and the electrical properties of MoS_2 flakes are probed. Moreover, we show that flipped flakes of 1T”-MoS_2 samples consist of monolayers of randomly oriented polarization, showing the possibility of head-head or tail-tail configuration. These results are presented in Chapter 6.

ACKNOWLEDGEMENTS

There are many people who have provided their invaluable help and support that have helped me to thrive during my graduate studies. Below, I would like to acknowledge those great people for their significant role in my scientific career.

First, I would like to extend my sincere gratitude to my adviser Prof. Alexei Gruverman who has always provided me with enormous support and effective guidance in all my research works. His constant input and feedback in my research have led me to think more critically about any research problems. I am highly indebted to my adviser for his resolute supervision and invaluable mentorship that has always motivated me toward the arena of success.

I would also like to thank my supervisory committee members: Prof. Alexei Gruverman, Prof. Evgeny Tsymbal, Prof. Peter Dowben, Prof. Stephen Ducharme, and Prof. Alexander Sinitskii for their guidance and support during my Ph.D. I am very much thankful to them for reading the draft of my dissertation and providing their insightful comments and feedback.

I heartily appreciate the significant contribution from my collaborators, in particular, Prof. Alexey Lipatov for teaching me the important skills on the two-dimensional materials deposition and helping with the discussion and interpretation of results, Prof. Alexander Sinitskii for granting me the opportunity to work in his laboratory and providing the samples for our research, Prof. Evgeny Tsymbal for providing the theoretical support towards the interpretation of our experimental results, Prof. Andrei Zenkevich for providing the samples, and Prof. Jeffrey Shield for assisting us with electron microscopy measurements.

I would also like to acknowledge my former Prof. Tao Li, current group members: Dr. Haidong Lu, Pratyush Buragohain, Ohheum Bak, Anarta Roy, and visiting scholar: Dr. Zhao Guan for the useful discussions, suggestions, help, and support. Mainly, I am very much grateful to Dr. Haidong Lu who has constantly guided me through the experimental details and assisted me with intellectual discussion and input towards the interpretation of the results. I would also like give my sincere thanks to my friend Bret Gergely for reading through this dissertation. Also, I would like to thank to the students and staff of the department of physics and astronomy for their immense help during my graduate studies.

Finally, I would like to dedicate this achievement to my beautiful wife for her warm support and unconditional love that always kept me motivated and energized throughout this Ph.D. journey. My parents' strong hope for me and their strong encouragement has always provided me the impetus to keep progressing during my Ph.D. Last but not least, I am also thankful to my sons Evan Chaudhary and Ethan Chaudhary for their immaculate love and beautiful smile that always motivated me for the next steps.

Preface

The results presented in Chapter 3 are published in *Applied Physics Letters.* (P. Chaudhary, P. Buragohain, M. Kozodaev, S. Zarubin, V. Mikheev, A. Chouprik, A. Lipatov, A. Sinitskii, A. Zenkevich, and A. Gruverman, Appl. Phys. Lett. **118**, 083106 (2021)).

The results of Chapter 4 have been published in *Nano Letters* (P. Chaudhary, H. Lu, A. Lipatov, Z. Ahmadi, J. P. V. McConville, A. Sokolov, J. E. Shield, A. Sinitskii, J. M. Gregg, and A. Gruverman, Nano Lett. **20**, 5873 (2020)).

The results shown in Chapter 5 have been published in *Nano Letters.* (P. Chaudhary, H. Lu, M. Loes, A. Lipatov, A. Sinitskii, and A. Gruverman, Nano Lett. **22**, 1047 (2022)).

The results of Chapter 6 have been published in *npj 2D Materials and Applications.* (A. Lipatov, P. Chaudhary, Z. Guan, H. Lu, G. Li, O. Crégut, K. D. Dorkenoo, R. Proksch, S. C. Hertel, D. -F. Shao, E. Y. Tsymbal, J. Íñiguez, A. Sinitskii, and A. Gruverman, npj 2D Mater. Appl. **6**, 18 (2022)).

Table of Contents

List of Figures

List of Table

Chapter 1

Introduction

1.1 Piezoelectric materials

Piezoelectricity is a material property characterized by an accumulation of surface polarization charges upon the application of mechanical stress. The materials that exhibit the aforementioned behavior are referred to as piezoelectric materials. Piezoelectric materials are non-centrosymmetric and do not have a center of inversion, due to which applied stress induces an asymmetric distribution of charges. Under the applied mechanical stress, the center of the positive and negative charges in the unit cell does not coincide, leading to a separation of charges, thereby inducing polarization. Similarly, a converse piezoelectric effect implies that an applied electric field can also lead to mechanical deformation in the material. The piezoelectric coefficient (d_{ij}) is used to determine the piezoelectric response of various materials. The direct and converse piezoelectricity can be summarized by the following mathematical equations [1]:

$$\text{Direct Piezoelectric effect: } P_i = d_{ijk}^{D}\sigma_{jk} \tag{1.1}$$

$$\text{Converse Piezoelectric effect: } x_{ij} = d_{kij}^{C}E_k \tag{1.2}$$

where, P_i, σ_{jk}, x_{ij}, E_k, d_{ijk}^{D}, and d_{jki}^{C} are polarization, stress tensor, strain tensor, electric field, direct piezoelectric coefficient tensor and converse piezoelectric coefficient tensor respectively. The piezoelectric coefficient is a tensor of rank 3. If the piezoelectric coefficient is measured along the direction of the applied electric field, then it is called the longitudinal piezoelectric coefficient, which is commonly denoted by d_{33} in matrix notation. Similarly, the piezoelectric coefficient measured perpendicular to the direction of the applied electric field is called the transverse piezoelectric coefficient. The other piezoelectric coefficient related to the shear deformation of the materials is called the shear piezoelectric coefficient. The longitudinal piezoelectric coefficient (d_{33}) is of significant interest in the research. For example, lead zirconate titanate ($Pb(Zr, Ti)O_3$) has been reported to show a large value (~100 pm/V) of longitudinal piezoelectric coefficient [2].

In the converse piezoelectric effect, the electric field-induced strain usually shows a butterfly-like loop resembling its hysteretic behavior under a dc bias sweep. Theoretically, for the pure piezoelectric effect, strain changes linearly with the electric field when the polarization and electric field are in the same direction, and the sign of the piezoelectric coefficient changes abruptly when the polarization is switched due to the applied electric field [Fig. 1.1a] [3]. The piezoelectric coefficient can be determined by plotting the strain-electric field hysteresis loop. The slope of the linear section indicates its magnitude. The experimental curve is plotted in figure 1.1b. This can be compared to the theoretical case in figure 1.1a. The deviation from the theoretical case is mostly due to the presence of different polarization components (P_x, P_y, P_z) and due to the gradual switching of polarization at its switching voltage.

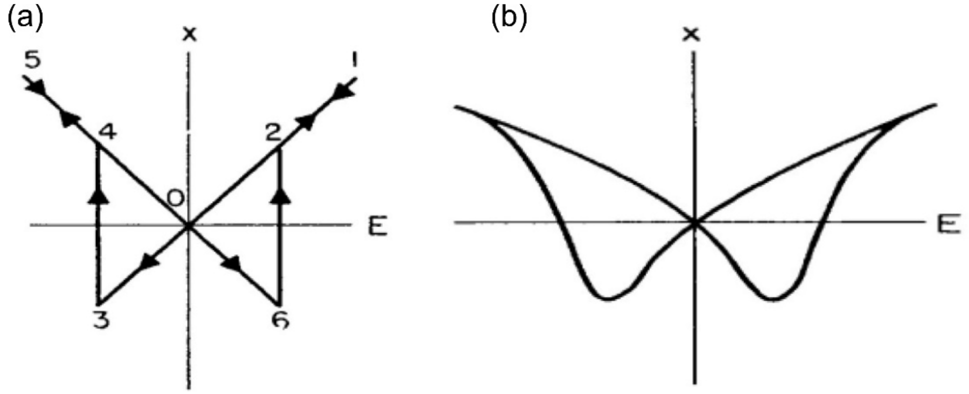

Figure 1.1: Strain-electric field piezoelectric hysteresis loops. (a) Ideal strain loop based on theory, (b) experimental strain loop taken on Pb(Zr,Ti)O_3. This figure is taken from reference [3].

Piezoelectricity is a linear electromechanical coupling between the strain and electric field. Piezoelectric materials have been used for various applications in different electromechanical devices such as actuators, transducers, acoustic wave sensors, piezoelectric scanners of scanning probe microscope (will be discussed in Chapter 2) etcetera. Besides piezoelectricity, a different electromechanical phenomenon called electrostriction [4, 5] deals with the quadratic coupling between the strain and electric field or polarization. The strain produced in the material due to the electrostriction can be written as [5]:

$$x_{ij} = M_{ijkl}E_kE_l \tag{1.3}$$

$$x_{ij} = Q_{ijkl}P_kP_l \tag{1.4}$$

where, M_{ijkl} and Q_{ijkl} and are the electrostrictive coefficients that couple the strain with the electric fields (E_k, E_l) and polarization (P_k, P_l) respectively. Electrostriction is a universal property that can occur in any kind of material and is not restricted by the symmetry of materials. The key difference between piezoelectricity and electrostriction is that in electrostriction, the strain does not change the sign when the polarization is reversed. This is because of the quadratic dependence on the electric field or polarization.

1.2 Ferroelectric materials

Ferroelectric materials are a special class of piezoelectric materials that have spontaneous polarization, which can be switched by different external stimuli such as electric field [6], strain gradient [7], optical illumination [8], etcetera. This property of the ferroelectric materials is called ferroelectricity. Spontaneous polarization is defined as the total electric dipole moment per unit volume of the unit cell. In the absence of an electric field, the presence of the non-zero polarization associated with the permanent electric dipole is called spontaneous polarization (P_s). Usually, the two or more polarization states in the ferroelectric materials are energetically equivalent and can be switched between them. Typically, the surface-bound polarization charges in the ferroelectric materials are compensated by the screening charges from the surrounding adsorbates.

In general, the occurrence of ferroelectricity in a material can be explained from the structural phase transition point of view [9, 10, 11]. Typically, at a transition temperature or Curie temperature (T_c), most ferroelectrics undergo a structural phase transition from the high-symmetry paraelectric phase ($P_s = 0$) at high-temperature ($T > T_c$) to a low symmetry ferroelectric phase ($P_s > 0$) at low-temperature ($T < T_c$). For example, lead titanate ($PbTiO_3$) is an archetype perovskite (structure: ABO_3; A is cation at corners, B is a central cation, and O is oxygen anion) ferroelectric that undergoes a phase transition from a paraelectric cubic phase to a ferroelectric tetragonal phase at 490°C [12]. The phase transition to a ferroelectric phase at T_c is usually accompanied by various types of anomalies in properties such as dielectric anomaly, a large increase in dielectric constant given by $\varepsilon = \frac{C}{T-T_0}$, where C is Curie constant, $T_0 \leq T_c$, anomalies in specific heat capacity, piezoelectric, and elastic constants [13]. All ferroelectrics, by default, exhibit piezoelectric effect and pyroelectric effect, a change in the value of the polarization with respect to the temperature.

In crystals, symmetry plays a vital role in describing the relationship between the properties and structures of the materials. In physics, symmetry is defined as the invariance of the fundamental properties of the materials under some physical transformations that include translation, rotation, reflection, and inversion. In crystallography, the crystals are classified into 7 different categories: triclinic, monoclinic, orthorhombic, tetragonal, rhombohedral, hexagonal, and cubic. The symmetry and physical properties of a crystal can be described by 32-point groups and 230-space groups [14]. Out of 32-point groups, 11 are centrosymmetric, and the rest 21 of them are non-centrosymmetric. Except for the 432-point group, the other 20-point groups exhibit piezoelectricity and are also called piezoelectric point groups. Only 10 out of 20 piezoelectric point groups have a polar axis and display ferroelectricity. Such 10 polar point groups are: 1, 2, m, 2mm, 4, 4mm, 3, 3m, 6, and 6mm, and these polar point groups accommodate all the ferroelectric materials.

1.2.1 Fundamental properties of ferroelectrics

1.2.1.1 Ferroelectric domains and domain walls

During the phase transition from paraelectric to ferroelectric phase, small regions with a finite polarization are formed in the materials. All the electric dipoles are aligned in the same direction within each region, called a domain. Domains with the opposite polarization orientation are separated by a nanoscopic boundary or interface called a domain wall (DW). The formation and the size of the domains in ferroelectrics depend upon the electrical and mechanical boundary conditions. Typically, the bound polarization charges in the material produce a depolarizing field ($E_d = \frac{P}{\varepsilon}$, where P is polarization and ε is dielectric constant) that is aligned antiparallel to the polarization direction. The magnitude of the depolarizing field can be an order of magnitude higher than the coercive voltage; thus, it can easily destabilize the ferroelectricity if the polarization charges are not screened.

The ferroelectric materials can minimize the depolarizing field by screening the polarization charges from the atmospheric adsorbates or the conducting electrodes. Complete screening of polarization charges can stabilize the ferroelectric material in a single-domain state. Another mechanism of ferroelectric stabilization involves forming the antiparallel domains separated by 180^0 DWs. Electrically neutral DWs are energetically favorable over the charged DWs. In the absence of screening charges, unbound polarization charges at the charged DW can increase the system's electrostatic energy (depolarizing energy), making it electrostatically incompatible. The smaller size of the domains reduces the depolarizing field significantly. In general, the size or width of the domain is mainly governed by the interaction between the domain energy ($E = Uw,$ where U is the volume energy density of the domain and w is the width of the domain), and the energy of domain walls ($E = \frac{\sigma d}{w}$, where σ is the energy density per unit area of the wall, d is the thickness of ferroelectric film). Minimization of the total energy with respect to w gives the Kittel's law [15, 16]:

$$w = \sqrt{\frac{\sigma d}{U}} \tag{1.5}$$

Equation 1.5 shows that the domain width scales linearly with the square root of the film thickness d, σ, and inversely with the square root of U. This equation assumes that the DWs do not have a finite width. However, in reality, DWs in ferroelectrics have a finite thickness (δ) of several nanometers, which leads to the modification of the square root dependence of the domain width as $w = \sqrt{G\delta d}$, where G is dimensionless constant [17].

The formation of the DWs can also occur due to the minimization of the elastic energy of the system. A typical example includes 90^{o} head-to-tail (H-T) DWs, commonly called ferroelastic DWs, which can be formed to relieve the elastic energy resulting from the mechanical stress applied to ferroelectric films. It has been demonstrated that domain walls in $PbTiO_3$ minimize the depolarizing energy and elastic energy via the formation of the 180^{o} ferroelectric DWs and 90^{o} ferroelastic DWs [16]. The functionality of domain and DW in ferroelectrics may be used for different device applications, such as resistive switching devices, that show an abrupt change in resistance, which will be discussed in Chapters 3 and 4.

1.2.1.2 Polarization switching and ferroelectric hysteresis curves

The domain switching in ferroelectrics occurs via nucleation and growth/expansion of the domains with opposite polarization, lateral motion of the domain walls, and coalescence of the domains. Different theoretical models have been proposed to explain the mechanism of the polarization switching in ferroelectrics: Kolmogorov-Avrami-Ishibashi (KAI) model [18] that includes the domain switching via nucleation followed by the lateral expansion of domains through domain wall motion, and nucleation-limited switching (NLS) model [19] that considers switching through the nucleation of domains, and intrinsic switching that occurs through the intrinsic motion of the domain walls in the electric field [20]. An intrinsic domain wall motion has been explained in terms of the domain wall creep at an applied electric field and temperature [20]. In the high-field regime, the size of the critical nucleus and the nucleation barrier approach zero, leading to polarization switching dominated by domain wall motion that exhibits a nearly linear dependence on electric field and a weaker dependence on temperature [20]. But at the low-field regime, a large critical size of the domain nucleus and high nucleation barrier favor polarization switching dominated via nucleation, and domain wall creep exhibits an Arrhenius temperature dependence [20].

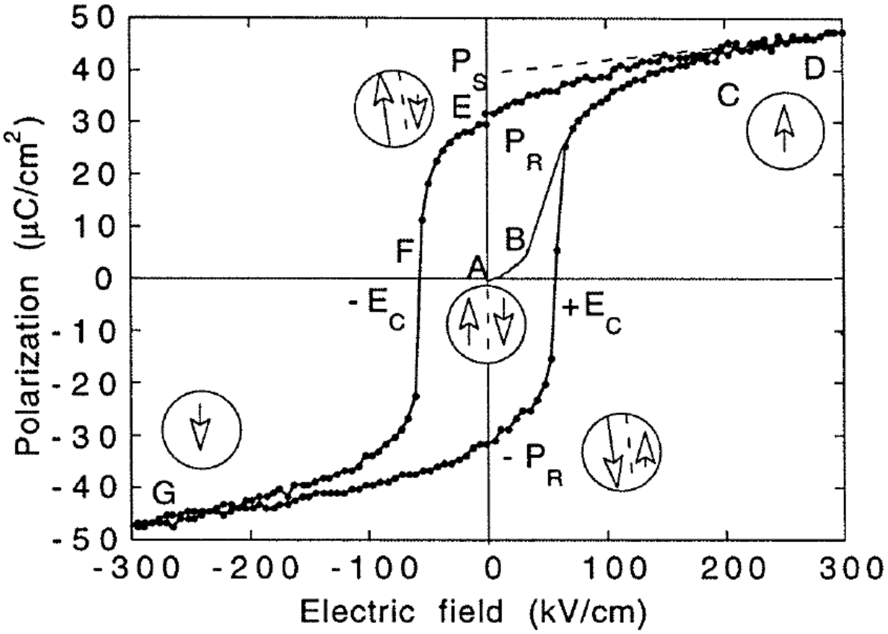

Figure 1.2: The ferroelectric P-E hysteresis loop. This figure is taken from reference [1].

It is typical for the ferroelectric materials to exhibit a hysteresis during the polarization switching. An example of the ferroelectric polarization versus electric field (P-E) hysteresis loop is shown in Figure 1.2. In experiments, the P-E hysteresis curve can be obtained by using the Sawer-Towyer method [21]. The occurrence of a hysteresis explains the non-linear dependence of polarization with the electric field. Suppose we subject a material initially with zero polarization to a sweep of a dc electric field. Initially, for the low value of an electric field, polarization ramps up linearly with the applied electric field showing dielectric behavior (segment AB). An increase in the positive applied electric field initiates a polarization alignment along the field direction (segment BC). Further increment of the positive field saturates the polarization value, called spontaneous polarization (segment CD). If we reduce the electric field, the polarization does not retrace along the DCBA path; instead, it follows a new route along DE. For negative values of the applied electric field, the polarization starts to switch in the opposite direction (segment EF). A non-zero value of the polarization at the zero electric field is called remanent polarization, denoted by P_R at point E. Further increment in the strength of the applied negative electric field switches the polarization and aligns it along the direction of the negative field. The field at which the value of polarization reduces to zero is called the coercive field. In the coercive field, the volume fraction of the domains with upward and downward polarization remains equal. Higher values of the negative applied field completely reverse the polarization orientation (segment FG). Upon the reversal in the direction of the applied field, the polarization acquires a negative value of remanent polarization ($-P_R$). Application of the positive electric field again switches the polarization back. This is how a complete P-E hysteresis curve is obtained.

An ideal P-E hysteresis curve is symmetric about the coercive field and remanent polarization, that is, $+E_c = -E_c$ and $+P_R = -P_R$. However, in actual experiments, the shape of the hysteresis can be affected by multiple factors: film thickness, defects, sample preparation conditions, measurement environmental conditions, and thermal treatment.

This can affect the experimentally measured values of coercive fields and remanent polarization. In this thesis, we will study the polarization switching and electronic transport properties of domains and DWs in ferroelectric thin films: hafnium zirconium oxide ($Hf_{0.5}Zr_{0.5}O_2$) and lithium niobate ($LiNbO_3$) (Chapters 3 and 4), and mechanical switching of polarization in the ferroelectric phase of two-dimensional (2D) molybdenum disulphide (MoS_2) (Chapter 6).

1.3 Two-dimensional transition metal dichalcogenides: Molybdenum disulfide

Prompted by the discovery of graphene by Novoselov et al, in 2004 [22], there has been a significant increase in research in the novel 2D materials due to their potential applications in energy harvesting, nanoelectronics, and optoelectronics devices. This includes 2D transition metal dichalcogenides (TMDs) with molecular formula MX_2, where M is a transition metal (such as Mo, W), and X is a chalcogen atom (such as S, Se, Te). Few examples of 2D TMDs are MoS_2, molybdenum diselenide ($MoSe_2$), tungsten disulphide (WS_2), tungsten ditelluride (WTe_2). 2D TMDs are layered materials, in which the transition metal (M) and chalcogen atoms (X) are bonded by a strong in-plane covalent bond within the monolayer and a weaker van der Walls bond between the adjacent interlayers. Unlike graphene that is a gapless semimetal, 2D TMDs are semiconductors with band gaps ranging from 1 to 2.5 eV with potential application in ultrathin low-power transistors [23, 24].

Out of 2D TMDs, MoS_2 is the most widely studied TMD due to its robust physical, electronic, and mechanical properties. Depending on the arrangement of Mo and S atoms, MoS_2 has several polymorphs: (i) 2H-MoS_2 that has trigonal prismatic coordination of Mo atoms, (ii) 1T-MoS_2 that has octahedral coordination of Mo atoms, (iii) 1T'-MoS_2, in which Mo atoms are distorted [Fig. 1.3]. The structures of MoS_2 can also be explained in terms of the stacking atomic planes of S and Mo atoms that form an S-Mo-S monolayer. 2H-MoS_2 has an ABA stacking, in which two atomic planes of S atoms exactly lie above the Mo atomic plane in a direction perpendicular to the S-Mo-S layer. On the other hand, 1T-MoS_2 consists of an ABC stacking, in which the S atom on the top atomic plane is rotated by 180^o with respect to the S atoms of the bottom plane in the same S-Mo-S layer. 1T'-MoS_2 phase further includes the distortion of the Mo atom, which further modifies the position of S atoms along the z-direction. Thermodynamically, the 2H phase of MoS_2 is more stable than that of the 1T phase of MoS_2.

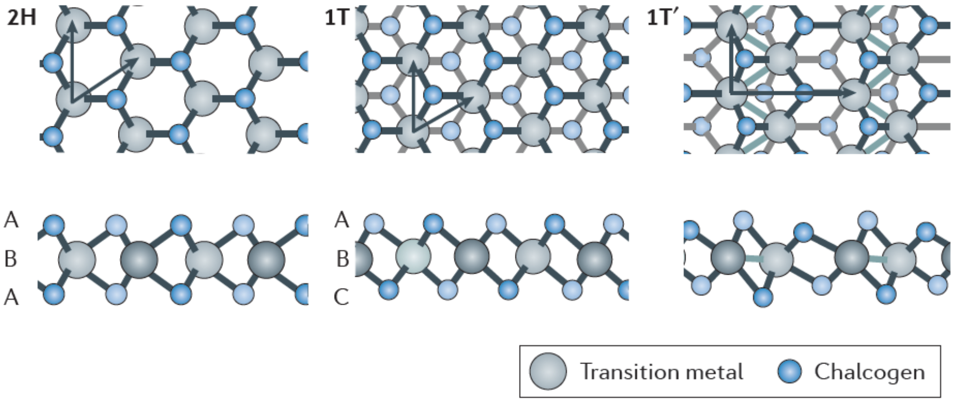

Figure 1.3: Structure of transition metal dichalcogenides. This figure is taken from reference [23].

The studies of the electronic band structures show that monolayer of 2H-MoS_2 (~0.65 nm thick) is a semiconductor with a direct band gap (~1.8 eV) while bulk 2H-MoS_2 has an indirect band gap (~1.3 eV) [25, 26, 27]. The presence of a band gap in 2H-MoS_2 enables its use as an active element in field-effect transistors (FET) [28]. The band gap of

2H-MoS_2 can be continuously tuned by the mechanical strain [29]. 2H-MoS_2 grown on SiO_2/Si substrate has been shown to have higher carrier mobility (~700 $cm^2V^{-1}s^{-1}$), high current on/off ratio of ~10^7 – 10^8, and significant optical absorption (~10^7/m for visible light) that makes it a potential candidate for the electronic and optoelectronic applications [30]. It is to be noted that 1T-MoS_2 is metallic, which displays a conductivity 10^7 times higher than semiconducting 2H-MoS_2 [31].

Apart from the promising electronic properties, freely suspended MoS_2 nanosheet (5-25 monolayers) has been demonstrated to have Young's modulus of elasticity (~330 ± 70 GPa) [32] while monolayer MoS_2 has an elasticity of ~270 ±100 GPa [33]. The value of Young's modulus of elasticity for MoS_2 exceeds the values for the stainless steel (~204 GPa) [34] and graphene oxide (~207 GPa) [35] showing the mechanical flexibility and strength of MoS_2.

1.4 Applications of ferroelectrics and 2D materials

In recent years, there has been a lot of progress regarding the commercial applications of ferroelectrics and 2D materials in nanoelectronic devices, logic devices, and memory devices. Ferroelectric domains and their polarization switching, P-E hysteresis, and the domain walls have been demonstrated as the basis for the non-volatile memory functionality in the device applications. One of the important applications of ferroelectrics includes the development of non-volatile memory devices. Ferroelectric random-access memory (FRAM) [36] is an example of a non-volatile random access memory device that is built in the same way as dynamic random-access memory (DRAM). FRAM is similar to DRAM in construction except that FRAM uses a ferroelectric layer such as $Pb(Zr,Ti))O_3$ instead of any dielectric layer. A FRAM memory cell typically comprises a ferroelectric capacitor and a transistor. Binary information is stored in the given polarization state of the ferroelectric capacitor. The information is read by using a polarization switching voltage to switch the polarization of the ferroelectric, thus allows a destructive read-out of the information. The FRAM offers several benefits: low power consumption, high writing speed, the high endurance of write-erase cycles, and better data reliability. However, unlike DRAM, FRAM offers lower storage capacity, and the destructive read-out of the information always requires the write-after-read architecture.

The other type of non-volatile memory based on the ferroelectrics is a ferroelectric field-effect transistor (FFET) that has a similar structure as a metal-oxide-semiconductor field-effect transistor (MOSFET). In an FFET, a gate dielectric is replaced by a ferroelectric layer, and the polarization of the ferroelectric layer controls the conductivity of the channel between the drain and source. The FFET offers a fast operation speed, high information storage capacity, and a non-destructive read-out of stored information.

Similarly, 2D TMDs have unique physical, mechanical, electronic, and optical properties that make them attractive for their applications in flexible electronics, sensing, optoelectronics, and photovoltaic devices. A solar cell based on the monolayer of MoS_2 on p-doped Si (p-Si) substrate has been demonstrated and is believed to work due to the formation of the built-in electric field at the MoS_2/p-Si interface that induces the separation of the photogenerated charge carrier leading to the photovoltaic performance [37]. Also, Wu et al, have demonstrated that the presence of piezoelectricity in the monolayer of MoS_2 can be used to form a prototype MoS_2-nanogenerator to harvest the electrical energy by applying an external strain [38]. Moreover, 2D TMDs have higher mechanical endurance towards the applied strain (up to 10% before breaking) [33], making them suitable for strain-induced electronics and optoelectronics applications. Application of the strain in 2D TMDs not only tunes the band gap of the material but also tunes the carrier concentration, carrier separation, diffusion, and recombination leading to the piezotronics devices [39, 40].

Furthermore, pairing the functional 2D TMDs materials and the ferroelectrics to form a hybrid structure may reveal some exciting phenomena due to the coupling of their material properties. The interaction between the ferroelectric polarization and semiconducting properties in MoS_2-$Pb(Zr,Ti)O_3$ FFET has led to hysteresis in the conductivity yielding a high OFF/ON ratio [41]. Similarly, a polarization-dependent conductance of MoS_2 in $MoS_2/BaTiO_3/SrRuO_3$ vertical junctions has enabled an abrupt change in the electronic transport with the resistance ratio (OFF/ON) up to 10^4 [42]. A prototype of a new programmable semiconductor device with MoS_2 as a conducting channel and $Pb(Zr,Ti)O_3$ as a ferroelectric gate has been shown using $MoS_2/Pb(Zr,Ti)O_3$ FFET where controlling the density of the nanoscale local domains written in $Pb(Zr,Ti)O_3$ film underneath MoS_2 continuously alters the in-plane conductivity [43].

References

---

[1] D. Damjanovic, Rep. Progr. Phys. **61**, 1267 (1998).

[2] Y. Saito, H. Takao, T. Tani, T. Nonoyama, K. Takatori, T. Homma, T. Nagaya, and M. Nakamura, Nature **432**, 84 (2004).

[3] F. Jona, and G. Shirane, *Ferroelectric Crystals*, (Dover, New York, 1993).

[4] H. F. Kay, Rep. Prog. Phys. **18**, 230 (1955).

---

[5] R. E. Newnham, V. Sundar, R. Yimnirun, J. Su, and Q. M. Zhang, J. Phys. Chem B **101**, 10141 (1997).

[6] A. Gruverman, D. Wu, H. Lu, Y. Wang, H. W. Jang, C. M. Folkman, M. Ye. Zhuralev, D. Felker, M. Rzchowki, C. -B. Eom, and E. Y. Tsymbal, Nano. Lett. **9**, 3539 (2009).

[7] H. Lu, C. -W. Bark, D. Esque de los Ojos, J. Alcala, C. B. Eom, G. Catalan, and A. Gruverman, Science **336**, 59 (2012).

[8] T. Li, A. Lipatov, H. Lu, H. Lee, J. -W. Lee, E. Torun, L. Wirtz, C. -B. Eom, J. Iniguez, A. Sinitskii, and A. Gruverman, Nat. Commun. **9**, 3344 (2018).

[9] A. F. Devonshire, Phil. Mag. **42**, 1065 (1951).

[10] L. D. Landau, Phys. Z. Sowjet. **11**, 545 (1937).

[11] V. Ginzburg, Zh. Dksp. Teor. Fiz. **15**, 739 (1945).

[12] G. Shirane, and S. Hoshino, J. Phys. Soc. Japan **6**, 265 (1951).

[13] M. E. Lines, and A. M. Glass, *Principles and Applications of Ferroelectrics and Related Materials*, (Oxford: Clarendon, New York, 1979).

[14] G. Burns and A. M. Glazer, *Space Groups for Solid State Scientists*, (Academic Press, Waltham, 2013).

[15] C. Kittel, Phys. Rev. **70**, 965 (1946).

[16] G. Catalan, Rev. Mod. Phys. **84**, 0034 (2012).

[17] J. F. Scott, J. Phys. Condens. Matter **18**, R361 (2006).

[18] Y. Ishibashi and Y. Takagi, J. Phys. Soc. Jpn. **31**, 506 (1971).

[19] A. K. Tagantsev, I. Stolichnov, N. Setter, J. S. Cross, and M. Tsukada, Phys. Rev. B **66**, 214109 (2002).

[20] S. Liu, I. Grinberg, and A. M. Rappe, Nature **534**, 360 (2016).

---

[21] C. B. Sawyer, and C. H. Tower Phys. Rev. **35,** 269 (1930).

[22] K. S. Novoselov, A. K. Geim, S. V. Morozov, D. Jiang, Y. Zhang, S. V. Dubonos, I. V. Grigorieva, and A. A. Firsov, Science **306**, 666 (2004).

[23] S. Manzeli, D. Ovchinnikov, D. Pasquier, O. V. Yazyev, and A. Kis, Nat. Rev. Mater. **2**, 17033 (2017).

[24] W. Choi, N. Choudhary, G. H. Han, J. Park, D. Akinwande, and Y. H. Lee, Mater. Today **20**, 116, (2017).

[25] M. Chhowalla, H. Y. Shin, G. Eda, L. -J. Li, K. P. Loh, and H. Zhang, Nat. Chem. **5**, 263 (2013).

[26] K. F. Mak, C. Lee, J. Hone, J. Shan, and T. F. Heinz, Phys. Rev. Lett. **105**, 136805 (2010).

[27] D. -S. Tsai, K. -K. Liu, D. -H. Lien, M. -L. Tsai, C. -F. Kang, C. -A. Lin, L. -J. Li, and J. -H. He, ACS Nano **7**, 3905 (2013).

[28] X. Tong, E. Ashalley, F. Lin, H. Li, and Z. M. Wang, Nanomicro. Lett. **7**, 203 (2015).

[29] H. J. Conley, B. Wang, J. I. Ziegler, R. F. Haglund, J. Sokrates, T. Pantelides, and K. I. Bolotin, Nano Lett. **13**, 3626 (2013).

[30] M. S. Fuhrer, and J. Hone, Nat. Nanotechnol. **8**, 146 (2013).

[31] R. Kappera, D. Voiry, S. E. Yalcin, W. Jen, M. Acerce, S. Torrel, B. Branch, S. Lei, W. Chen, S. Najmei, J. Lou, P. M. Ajayan, G. Gupta, A. D. Mohite, and M. Chhowalla, APL Mater. **2**, 092516 (2014).

[32] A. C. -Gomez, M. Poot, G. A. Steele, H. S. J. van der Zant, N. Agrait, and G. R. -Bollinger, Adv. Mater. **24**, 772 (2012).

[33] S. Bertolazzi, J. Brivio, and A. Kis, ACS Nano **5**, 9703 (2011).

---

[34] D. Peckner, and I. M. Bernstein, *Handbook of Stainless Steels*, (McGraw-Hill book Company, New York, 1977).

[35] J. W. Suk, R. D. Piner, J. An, and R. S. Ruoff, ACS Nano **4**, 6557 (2010).

[36] T. Eshita, W. Wang, K. Nomura, K. Nakamura, H. Saito, H. Yamaguchi, S. Mihara, Y. Hikosaka, Y. Kataoka, and M. Kojima, Jpn. J. Appl. Phys. **57**, 11UA01 (2018).

[37] M. -L. Tsai, S. -H. Su, J. -K. Chang, D. -S. Tsai, C. -H. Chen, C. -I. Wu, L. -H. Li, L. -J. Chen, and J. -H. He, ACS Nano **8**, 8317 (2014).

[38] W. Wu, L. Wang, Y. Li, F. Zhang, L. Lin, S. Niu, D. Chenet, X. Zhang, Y. Hao, T. F. Heinz, J. Hone, and L. Wang, Nature **514**, 470 (2014).

[39] F. Xue, L. Chen, J. Chen, J. Liu, L. Wang, M. Chen, Y. Pang, X. Yang, G. Gao, J. Zhai, and Z. L. Wang, Adv. Mater. **28**, 3391 (2016).

[40] F. Xue, L. Yang, M. Chen, J. Chen, X. Yang, L. Wang, L. Chen, C. Pan, and Z. L. Wang, NPG Asia Mater. **9**, e418 (2017).

[41] A. Lipatov, P. Sharma, A. Gruverman, and A. Sinitskii, ACS Nano **9**, 8089 (2015).

[42] T. Li, P. Sharma, A. Lipatov, H. Lee, J. -W. Lee, M. Y. Zhuralev, T. R. Paudel, Y. A. Geneko, C. -B. Eom, E. Y. Tsymbal, A. Sinitskii, and A. Gruverman, Nano Lett. **17**, 922 (2017).

[43] A. Lipatov, T. Li, N. S. Vorobeva, A. Sinitskii, and A. Gruverman, Nano Lett. **19**, 3194 (2019).

Chapter 2

Experimental Methods

In this research, the polarization-related electronic transport properties in the ferroelectric thin films coupled with two-dimensional materials are studied using the atomic force microscopy (AFM) technique, one of the scanning probe microscopy (SPM) techniques. AFM has been widely employed in its various advanced operating modes such as piezoresponse force microscopy (PFM), Kelvin probe force microscopy (KPFM), electrostatic force microscopy (EFM), and conductive AFM (CAFM) to explore the various properties of the materials.

2.1 Scanning Probe Microscopy

SPM is a surface analysis technique that uses a sharp probe that is scanned over the surface of the sample and measures the nanoscopic properties of the surface by detecting the tip-surface interaction. SPM has emerged as a powerful scientific tool for the characterization and manipulation of different properties of the material at nanometer or atomic scales spatial resolution. For instance, SPM can be used for nanoscale domain imaging and their manipulation in ferroelectrics, probing the local surface charges and surface potential in semiconductors and ferroelectrics, and analyzing mechanical and electromechanical properties of the materials. The first invention of the SPM can be dated back to 1982, when two researchers, G. Binnig and H. Rohrer, working at the IBM Zurich Research Laboratory, invented the scanning tunneling microscope (STM) [1]. They were awarded the Nobel Prize for this significant invention. STM consists of a very sharp conductive probing tip that makes a raster scan over the surface of conducting material, a piezoelectric scanner that controls the vertical and lateral motion of the tip, a current amplifier to measure the tunneling current, and feedback electronics that adjusts the tip-sample distance during scanning. The working principle of STM is based on quantum tunneling of the electron across a thin barrier between the STM tip and the sample under the application of a small bias applied between the tip and sample. The tunneling current has an exponential dependence on the tip-sample separation and the work function:

$$I_t \propto V\rho_s(\epsilon_F)\exp\left[\left(-\frac{2}{\hbar}\sqrt{2m\varphi}\right)z\right] \tag{2.1}$$

where V is applied voltage, $\rho_s(\epsilon_F)$ is the local density of states near the Fermi level of the sample, φ is the effective local work function, and z is the tip-sample separation, which is typically a few nanometers. This relationship (2.1) is, of course, only approximated as it ignores the symmetry, wave vector, and tip that all do play a role. During scanning, the tunneling current is kept constant using a feedback loop system by adjusting the tip-sample separation. The internal circuits record and analyze such adjustments, and a final 2D map of the electronic structure density of the surface is produced.

2.1.1 Atomic Force Microscopy and its working principle

STM has been widely used in exploring the multitude of materials properties such as surface roughness, defects, and studying catalytic reactions on the surface [2]. However, STM is still limited to semiconducting or conducting materials. To overcome this drawback of the STM, in 1986, Binig, Quate, and Gerber [3] invented the AFM that senses the tip-sample interaction forces instead of the tunneling current as in STM. AFM can be used to image all kinds of materials, either conducting or insulating, such as polymers, ceramics, glass, and biological specimens at an atomic or nanoscale resolution. Different advanced operating modes of AFM have been developed to explore material properties such as morphological, mechanical, electrical, electromechanical, magnetic, and optical properties.

Like STM, AFM consists of a cantilever with a sharp probe/tip that is raster-scanned over the surface of a material. A schematic of a conventional AFM system is shown in Fig. 2.1. It basically consists of an ultrasharp AFM tip mounted on a cantilever, a piezoelectric scanner that monitors the x, y, and z motion of the sample stage, a position-sensitive 4-quadrant photodetector system, and feedback electronics. A laser beam is shined on the back of the AFM cantilever that reflects the beam into the 4-quadrant array of position-sensitive photodetectors. As the AFM tip scans the surface, the tip-sample force of interaction changes, which leads to a change in the deflection of the cantilever, which is detected by the photodetectors. A feedback loop adjusts the vertical motion (z-motion) of the cantilever to maintain the constant cantilever deflection, hence constant tip-sample force. The reflected laser beams are recorded, analyzed, and used to create a high-resolution image of the topography.

Depending upon the tip-sample separation distance, the AFM tip interacts with the sample surface via various kinds of forces that may be short-range and long-range forces. Typical examples of such interacting forces are short-range repulsive force, van der Walls force, covalent force, magnetic force, electrostatic force, and capillary force.

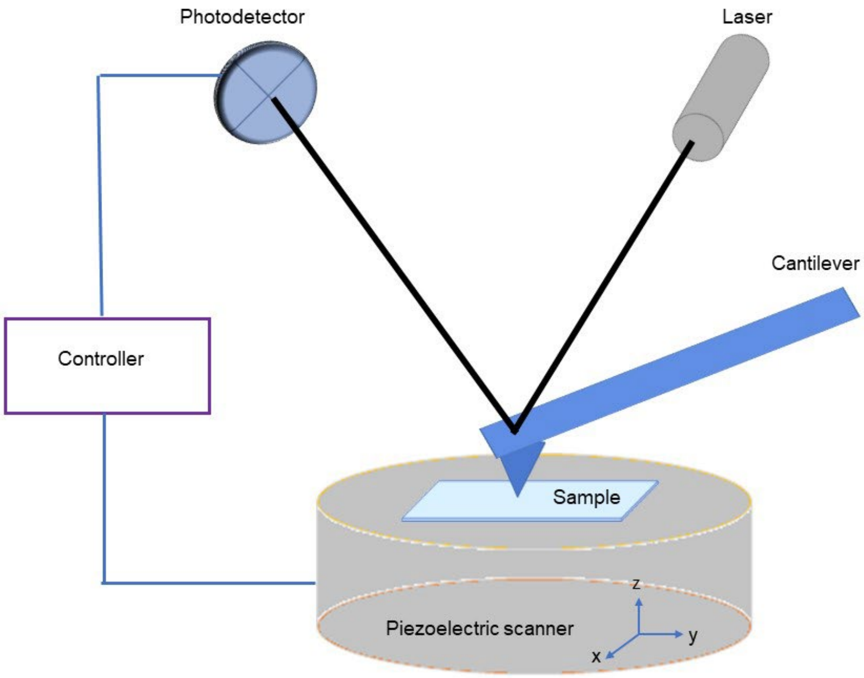

Figure 2.1: A schematic of AFM set-up.

When the AFM tip is held in contact with the surface, a superposition of the electronic wavefunctions of the tip and sample leads to a short-range repulsive force between the tip and sample. As the tip is lifted a few tens of nanometers above the surface, then van der Waals attractive force between the tip and sample dominates. For very large separation (> 100 nm), the magnitude of the interacting forces decays and is no longer detected by AFM.

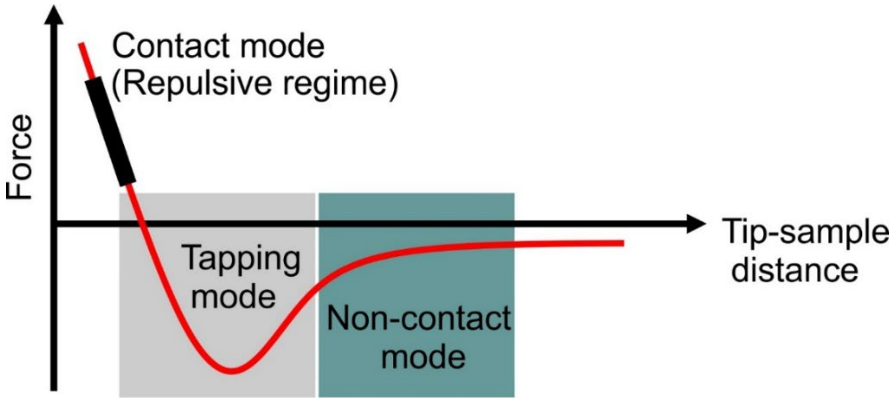

Figure 2.2: The force versus distance curve showing the different regions operating at different basic modes.

2.1.1.1 Non-contact mode

In this mode, the AFM tip is located tens of nanometers above the surface of the sample. The cantilever is mounted on a piezoelectric actuator that excites the cantilever at its resonant frequency; therefore, this mode is also called a dynamic mode. The resonance characteristics such as oscillation amplitude, frequency ($w_r = \sqrt{\frac{k}{m}}$, where k is the spring constant and m is the mass of the cantilever), and phase are changed due to the tip-sample interaction forces during scanning. A feedback loop helps maintain the cantilever's constant oscillation amplitude by adjusting the separation distance between the AFM tip and the sample surface. The AFM tip interacts with the sample surface via an attractive force in this mode.

Imaging in this mode allows obtaining the morphological information of the surface, such as topography, surface roughness, grain size, and thickness. It is non-destructive and can also be used to image soft samples like organic crystals and biological specimens.

2.1.1.2 Contact mode

Contact mode is a static mode in which the AFM tip is placed in contact with the sample surface and maintains a constant force during scanning. The tip load can be calculated from Hooke's law ($F = kx$), where k is the spring constant and x is the bending of the cantilever. A constant scanning force is maintained by keeping a constant deflection of the cantilever. The tip-sample contact force is repulsive short-range as it originates due to the overlap of the electronic orbitals of the tip and sample surface. Typical cantilevers used in these operating modes have a spring constant value of 0.01- 5 N/m.

This contact mode can be used to obtain the topographic image and the adhesion forces of the material. The main drawback of this mode is that it is destructive as the tip-induced lateral forces can easily remove the loosely bonded surface adsorbates from the top surface of the materials.

2.1.2 Piezoresponse Force Microscopy

Ferroelectric materials allow a wealth of technological applications in high-density data storage [4, 5] and non-volatile memory [6]. The exploration of the ferroelectric properties such as domain switching, nucleation rate, imprint, polarization fatigue, and retention are therefore very crucial for electronic applications. Different characterization techniques such as polarized optical microscopy [7], scanning transmission electron microscopy (STEM) [8, 9], scanning second harmonic generation (SSHG) [10], scanning electron microscopy [11], and surface etching [12] have been developed for imaging the domain structures in ferroelectrics. However, the optical approaches, such as polarized optical microscopy and SSHG, are only suitable for bulk ceramics and single crystals where the domain size exceeds the wavelength of the light used. Investigating domain structures in ferroelectric thin films becomes challenging as domain size scales down with the film thickness or grain size, making them as small as tens of nanometers. Similarly, the electron microscopy technique suffers from the complex sample preparation tool, surface charging, and higher energy of electrons can easily alter the pristine domain configuration. To overcome these difficulties, piezoresponse force microscopy (PFM) has evolved as a powerful tool for non-destructive and nanoscale imaging of the domains, domain walls, and their manipulation. The spatial resolution of the domain imaging in PFM can be lowered to tens of nanometers.

In 1992, P. Guthner and K. Dransfeld demonstrated the seminal work to image the locally polarized domains created by dc poling of ferroelectric thin polymer films of vinylidene fluoride and trifluroethylene (VDF-TrFE) [13]. In 1996, Gruverman et al, first introduced the term "piezoresponse" and discussed the nanoscale visualization of domains in the ferroelectric thin films [14, 15]. Since then, PFM has become a standard imaging tool for the nanoscale studies of domain structures and their manipulation in ultrathin ferroelectric thin films [16], ferroelectric capacitors [17], and biological specimens [18].

2.1.2.1 Theory of PFM

PFM is based on the detection of local electromechanical deformation of the surface of ferroelectric material via the converse piezoelectric effect. Specifically, an applied electric field via AFM tip on the ferroelectric surface will result in the local mechanical deformation of the sample. A type of mechanical deformation, either expansion, contraction, or shear, is governed by the relative orientation of the external electric field, the polarization vector, and the sign of the piezoelectric coefficient. The strain due to the mechanical deformation is linearly coupled with the applied electric field, which is described as [19, 20]:

$$s_j = d_{ij} E_i \tag{2.1}$$

where s_j is the strain, d_{ij} is the converse piezoelectric coefficient tensor and E_i is the applied electric field. Furthermore, the piezoelectric coefficient (d_{ij}) is related to the ferroelectric polarization as [21]:

$$d_{ij} = 2 \in_{im} Q_{jmk} P_k \tag{2.2}$$

where $\in_{im}$ is a dielectric constant tensor, Q_{jmk} is electrostriction coefficient tensor, and P_k is polarization vector. For a ferroelectric material with a tetragonal symmetry (point group: 4mm), the non-vanishing components of the piezoelectric coefficients are coupled with the spontaneous polarization as [2120]:

$$d_{33} = 2 \in_{33} Q_{33} P_3 \tag{2.3a}$$

$$d_{31} = 2 \in_{33} Q_{13} P_3 \tag{2.3b}$$

$$d_{15} = 2 \in_{11} Q_{44} P_3 \tag{2.3c}$$

where d_{33} is the longitudinal piezoelectric coefficient measured along the polar axis when the external electric field is aligned parallel to the polar axis, d_{31} is transverse piezoelectric coefficient measured when the direction of the external electric field is perpendicular to its polar axis, and d_{15} is the shear coefficient associated with the shear deformation of the sample.

The longitudinal piezoelectric coefficient (d_{33}) is of major interest in ferroelectrics. If an electric field is applied to the ferroelectric material in the z-direction, then equation (2.1) can be rewritten as:

$$s_3 = d_{33} E_3 \tag{2.4}$$

But,

$$E_3 = \frac{V}{L} \tag{2.5}$$

where V is the applied voltage across the sample and L is the thickness of the film. Further, the z-component of the strain (s_3) can be computed as

$$``s_3 = \frac{\Delta z}{L} \tag{2.5a}$$

From equation (2.4) - (2.6), it can be obtained that:

$$\Delta z = d_{33} V \tag{2.6}$$

Equation (2.6) gives the linear coupling between the out-of-plane deformation (z-component) and the applied voltage. For upward polarization orientation, $\Delta z > 0$ (expansion of the sample) and $d_{33} > 0$, but for the downward polarization, $\Delta z < 0$ (contraction of the sample) and $d_{33} < 0$. Thus, equation (2.6) can be re-written as:

$$\Delta z = \pm d_{33} V \tag{2.6a}$$

This suggests that linear coupling between the piezoelectric coefficient and ferroelectric polarization can be exploited to detect the domain polarity by determining the sign of deformation (Δz). The ± sign indicates the opposite sign of the piezoelectric coefficient for the two oppositely polarized domains.

Usually, ferroelectric materials have a value of the piezoelectric coefficient in the order of tens of pm/V, so the static deformation due to the applied dc voltage is typically in the sub-nanometer range, which makes it exceedingly difficult to detect the static piezoresponse. For instance, the piezoelectric coefficient of BTO thin films is 50 pm/V [22] and in the static piezoresponse mode kept at 1V dc bias, the value of the bias-induced static deformation is only 50 pm. The detection of such a small displacement (pm – Å) will be masked by the surface roughness that can be several nanometers in size, hence making it very difficult to image the domains in static piezoresponse mode. A remedy to this problem is using the PFM in dynamic mode with an ac modulation voltage (at a few hundred kHz) applied through the probing tip. The PFM tip is used to apply the alternating voltage (hence, the alternating electric field) across the sample causing it to vibrate locally at the modulation frequency of applied bias. The electromechanical vibration is detected and is amplified by the lock-in technique, thus making it more efficient for domain imaging.

For an ac voltage applied between the tip and the sample:

$$V = V_{dc} + V_{ac}cost(wt) \tag{2.7}$$

the piezoresponse is measured as the first harmonic component of cantilever deflection, which is:

$$z = z_{dc} + A_{1w}\cos{(wt + \varphi)} \tag{2.8}$$

where, z_{dc} is the dc component of cantilever deflection and φ is the phase difference between the applied ac bias and the cantilever deflection. The value of φ provides information on the polarization orientation of the probing domain underneath the tip. For the ferroelectric films with c^- domains where the polarization is pointing downward, an application of positive voltage causes the sample to expand. This, in turn, keeps the piezoresponse in phase with the applied ac voltage, that is, $\varphi = 0^\circ$. On the other hand, for the c^+ domains with upward polarization, a positive voltage causes contraction of the surface, which causes piezoresponse to be out-of-phase with the applied voltage, that is, $\varphi = 180^\circ$. An illustration of this phase relationship between the piezoresponse and the ac voltage is demonstrated in Fig. 2.3. The amplitude A_{1w} gives a measure of the bias-induced mechanical deformation of the sample and its value depends upon the tip-sample geometry and material properties.

Throughout this research, the PFM has been operated in the dynamic mode to investigate the polarization phenomena in the ferroelectrics, 2D materials, and their heterostructures.

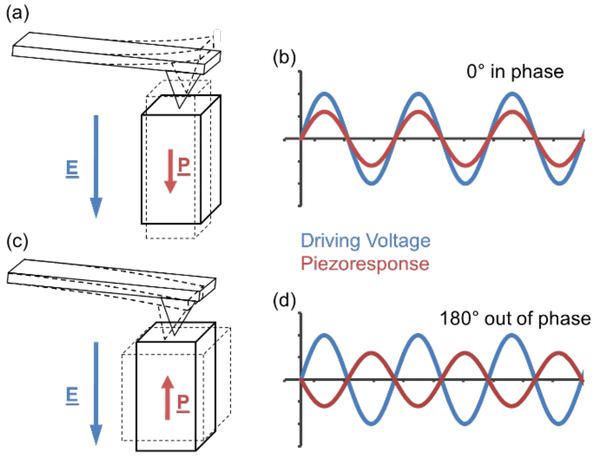

Figure 2.3: The schematics of phase mapping between the piezoresponse and driving voltage. (a,b) in-phase on c^- domain, (c,d) out-of-phase on c^+ domain. This figure is taken from reference [23].

The PFM detects the mechanical displacement of the cantilever due to the surface vibration induced by an ac bias. The vertical deflection of the cantilever ($z = d_{33}V_{ac}\cos{(wt + \varphi)}$) is detected in vertical PFM (VPFM) mode, which measures the out-of-plane polarization component due to the longitudinal piezoelectric coefficient (d_{33}). But the lateral-torsional motion of the cantilever ($x = d_{15}V_{ac}\cos{(wt + \varphi)}$) is detected in the lateral PFM (LPFM) mode that measures the in-plane polarization component due to the piezoelectric coefficient's shear component (d_{15}). Simultaneous detection of bias-induced expansion/contraction and shear deformation of sample is done using vector PFM that combines VPFM and LPFM. Vector PFM can be used to reconstruct the three-dimensional (3D) polarization distribution in polycrystalline films.

Both VPFM and LPFM are described by the amplitude and phase images that carry vital information about the ferroelectric properties. The amplitude signal portrays the information about the magnitude of polarization, showing a finite, non-zero value at the domains and a minimum or virtually zero value at the domain wall. Similarly, the PFM phase reveals the information about the direction of polarization of domains, showing a 180° contrast across the domain wall. A typical example of VPFM and LPFM images taken on $PbTiO_3$ film is shown in Fig. 2.4.

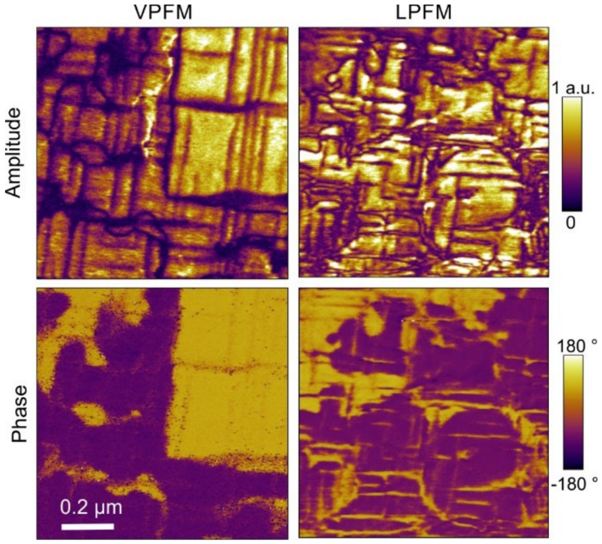

Figure 2.4: The VPFM and LPFM on $PbTiO_3$(90 nm)/$SrRuO_3$/$KTiO_3$.

In real-time experiments, the cantilever deflection can be affected by the true piezoelectric effect and extrinsic effects such as capacitive and non-local electrostatic contributions. Accounting for these effects, the resultant amplitude of vibration of the cantilever in PFM mode is [24]:

$$A = A_{piezo} + A_{cap} + A_{nl} \tag{2.9}$$

where, A_{piezo} is true electromechanical response arising from the converse piezoelectric effect, A_{cap} is due to the capacitive interaction between the AFM tip and sample surface, and A_{nl} is due to the non-local electrostatic contribution between the tip and sample. The extrinsic effects can be minimized by using short and stiff cantilevers, using top electrodes on the film surface, and maintaining zero dc bias during PFM measurements [24].

2.1.2.2 Experimental set-up for PFM

PFM allows the control of domain imaging and its manipulation at the nanoscale level. PFM is operated in contact mode where a conductive AFM tip is placed in contact with the sample surface. The probe (tip) performs the dual function where it acts as an actuator for the application of an electric field to excite the sample and simultaneously acts as a sensor to detect the local piezoelectric deformation induced by an applied electric field. The local piezoelectric deformation is monitored as a cantilever deflection that changes the position of the reflected laser beam onto the array of photodetectors. A schematic of the experimental set-up of PFM is shown in Fig. 2.5.

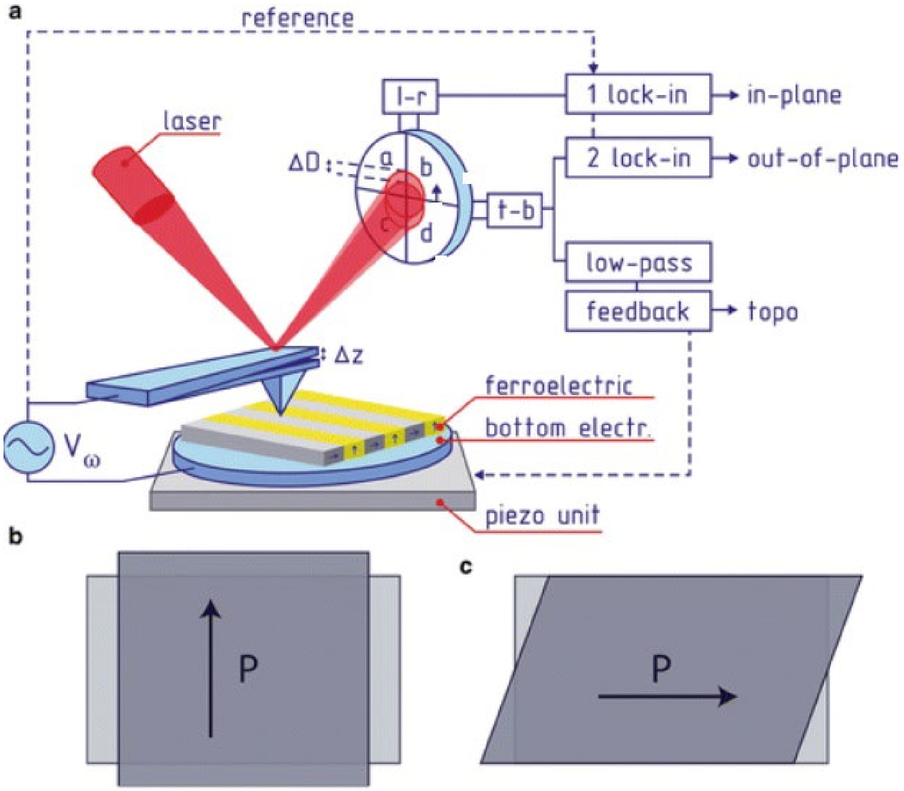

Figure 2.5: A schematic of PFM set-up. This figure is taken from reference [25].

2.1.2.3 Dual AC Resonance Tracking PFM

In AFM, the tip-sample interaction can change the resonance frequency of the cantilever, when the tip is scanning above the sample surface. One of the frequency tracking methods that is commonly used in non-contact AFM is the phase-locked loop method that considers the phase difference between the driving source and response signals as an error signal for the feedback loop. The feedback circuit adjusts the driving frequency to maintain a constant phase for the cantilever deflection. For successful frequency tracking by the phase-locked loop method, the amplitude and phase of driving force should be independent of the position of the tip relative to the sample surface and the frequency of driving voltage. However, in PFM, the phase-locked loop detection strategies do not work as the amplitude and phase of the local response are related to the material properties of ferroelectrics. The cantilever deflection will exhibit a 180° phase contrast (Equation 2.8) for the antiparallel domains; hence it cannot be used as a feedback signal.

A commonly used method to overcome this difficulty with PFM is referred to as the dual ac resonance tracking (DART) method [26] [Fig. 2.6]. In DART-PFM, two ac driving voltages with oscillation frequencies f_1 (slightly below the contact resonance frequency f_0) and f_2 (slightly above f_0) are applied between the conductive tip and bottom electrode of the sample. These driving voltages are used as reference signals by the two internal lock-in amplifiers and the piezoresponse signal is recorded as amplitudes A_1 and A_2, and phases φ_1 and φ_2 at two frequencies f_1 and f_2 by the lock-in amplifiers. The amplitude difference ($\Delta A = A_2 - A_1$) is used as an input to the feedback for tracking of contact resonance frequency during the scanning. Typically, the frequencies f_1 and f_2 are chosen such that the frequency difference ($\Delta f = f_2 - f_1 \geq 2BW$), where BW is the imaging bandwidth that is typically in the order of 5 – 10 kHz.

Typically in ferroelectrics, the amplitude of electromechanical vibration of a sample is only a few tens of picometers. This makes it difficult to detect small vibrations in non-resonant, constant frequency PFM, especially if the materials have a small piezoelectric coefficient. But in the DART-PFM mode, as the imaging of ferroelectric domains is done at or close to the resonant frequency, the electromechanical response is amplified by around 2 – 3 orders of magnitude following the equation ($A = d_{33} V_{ac} Q$); where the quality factor (Q) of the resonance usually has values in the range 10-100. Moreover, topographic crosstalk in the piezoresponse can be minimized by operating slightly below the resonant frequency, instead of at the resonance. This also results in the enhancement of the signal-to-noise ratio when the imaging is conducted slightly off resonance. The DART-PFM mode is, therefore, particularly useful in studying the domain imaging and its manipulation in the ferroelectric materials with weaker piezoelectric coefficients such as ultrathin ferroelectric thin films and the two-dimensional ferroelectrics.

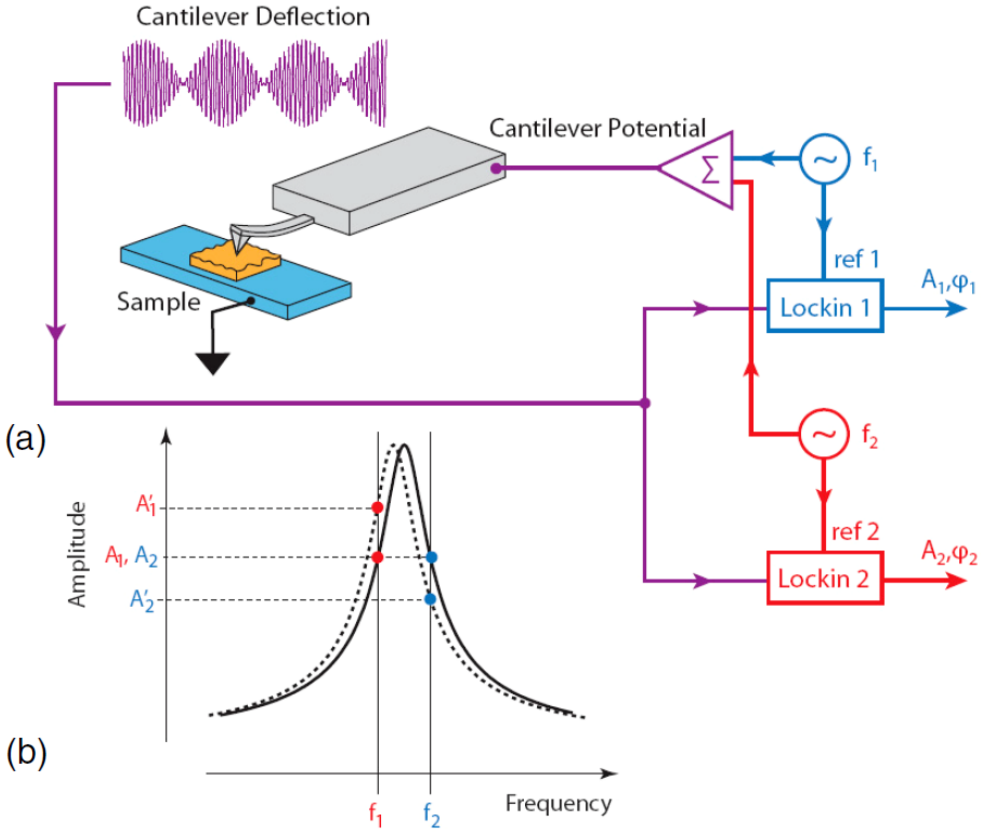

Figure 2.6: A schematic for DART-PFM mode. This figure is taken from reference [26].

2.1.2.4 Switching Spectroscopy PFM

Switching Spectroscopy PFM (SS-PFM) is a technique that provides quantitative information about the polarization switching parameters by obtaining the local piezoelectric hysteresis loops in the ferroelectric materials. SSPFM measures the local ferroelectric hysteresis loops by applying the dc triangular waveform along with the ac modulation bias via the PFM tip at a fixed location on the sample surface. In ferroelectrics, the local hysteresis loop is a signature of switchable polarization. Also, it offers quantitative information about the switching parameters such as coercive bias (or coercive field), imprint, and nucleation bias. The local ferroelectric hysteresis loop obtained in SS-PFM is a nanoscopic analog of the macroscopic polarization-voltage (P-V) hysteresis loop.

Based on the nature of the applied dc voltage, there are two different modes for acquiring the PFM hysteresis loops, which are continuous mode (or step mode) and pulsed mode [27] [Fig. 2.7]. In the continuous mode, the piezoelectric hysteresis loop is obtained by applying ac bias simultaneously with continuously increasing and decreasing dc voltage in the form of steps. This resulting hysteresis is referred to as a bias-on hysteresis. It is strongly influenced by the electrostatic force of interaction between the cantilever and the sample surface caused by the applied dc bias. The step mode is suitable for the ferroelectric capacitors where the electrostatic interaction is significantly reduced due to the screening. On the other hand, in pulsed mode, the dc voltage pulse is turned on and off periodically along with the ac modulation voltage for the hysteresis measurement. The piezoelectric hysteresis loop is recorded during the zero-dc bias; thus, it is called a bias-off hysteresis. Since the electrostatic and the capacitive contribution to the piezoelectric response is reduced at the zero bias, the bias-off hysteresis is preferred over the bias-on hysteresis during the SS-PPFM studies in the ferroelectric thin films and the 2D ferroelectrics.

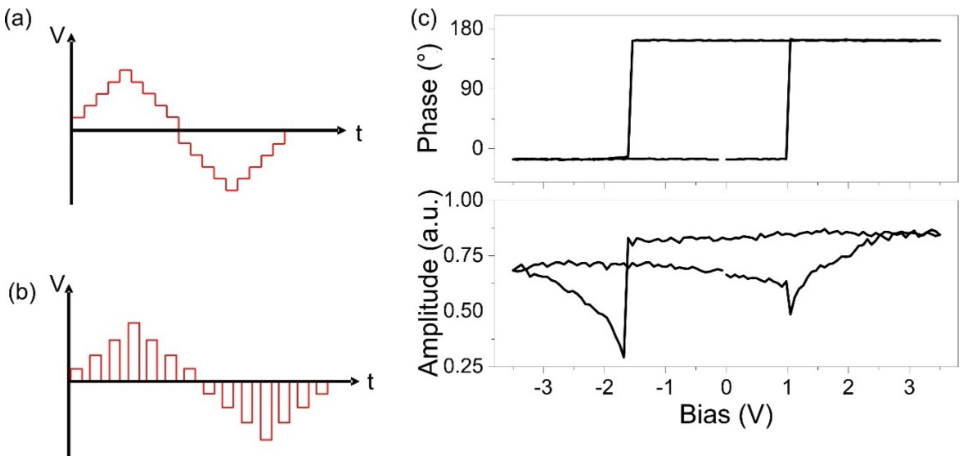

Figure 2.7: The operation of PFM spectroscopy in two different modes. (a) Step mode, (b) Pulsed mode. (c) A bias-off hysteresis obtained on PZT (30nm)/LSMO/STO.

2.1.3 Conductive Atomic Force Microscopy

Conductive AFM (CAFM) is used to measure the local electrical current (conductivity) across the sample using a constant dc bias applied between the AFM tip and the sample. CAFM was first used by Murrell et al, in the 1990s for the local electrical characterization in SiO_2 gate dielectrics [28]. CAFM is operated in a contact mode, where a conducting AFM tip maintains contact with a constant force on the sample surface. Additionally, the conductive AFM tip is connected to a highly sensitive trans-impedance operational amplifier, a current-to-voltage converter, to measure the current from sub-pA to tens of nano-amps.

In CAFM, a topographic image of the sample surface is obtained by using contact mode. An additional local current map is simultaneously obtained in response to the constant dc bias applied between the AFM tip and the bottom electrode of the sample. Local current-voltage (I-V) spectroscopic measurements can be performed by applying a dc voltage sweep (usually bipolar triangular waveform) to the sample while sensing the current from the AFM tip. The I-V characteristics curves facilitate measuring the differential resistance ($R = \frac{dV}{dI}$) of the sample.

CAFM has various applications in nanoscale studies of electrical conductivity in metals, semiconductors, and insulators. It can be used to investigate the local electrical transport functionality such as resistive switching in ferroelectrics, domain wall conductivity in ferroelectrics, photovoltaic effect in halide perovskites such as methylammonium lead bromide ($MAPbBr_3$), $CsPbBr_3$, and local tip induced stress modulation of resistance in 2D materials.

2.1.4 Electrostatic Force Microscopy

Electrostatic force microscopy (EFM) is a surface imaging technique used to map the surface charges present in the sample. This is based on the electrostatic interaction between the AFM tip and the sample surface due to the dc bias applied to the AFM tip. Assuming a capacitor system formed by the tip and the sample, this electrostatic interaction is expressed as [29]:

$$F = \frac{1}{2}\frac{\partial C}{\partial z}V^2 \tag{2.10}$$

where C is capacitance, V is voltage and $\frac{\partial C}{\partial z}$ is capacitance gradient.

EFM is operated in a non-contact AFM mode and follows the dual-pass measurement approach. In the first pass, the AFM tip scans over the sample surface in non-contact or tapping mode to generate the topographic image. In the second pass, also called the nap pass, the AFM tip is lifted at a constant height of 30 nm – 50 nm above the sample surface and senses the electrostatic forces due to the applied dc bias while following the topographic trace. The vibration of the tip over the sample leads to the tip-sample capacitance gradient ($\frac{\partial C}{\partial z}$) during scanning in the nap pass. This generates a force gradient, that leads to the shift of the resonant frequency ($\Delta w = \frac{w_0}{2k}\frac{\partial F}{\partial z}$) of the oscillating cantilever [29]. An attractive force arises between the AFM tip and the sample surface. This causes a positive force gradient that shifts the resonance frequency in the direction of increasing force. On the other hand, a repulsive force will result in a negative gradient that shifts the resonance in the opposite direction. This leads to changes in the oscillation amplitude and frequency of the AFM probe are detected by the lock-in amplifier and are recorded as EFM amplitude and phase.

In ferroelectric materials, EFM is commonly used to investigate the sign of the surface screening charges, which screens the bound polarization charges of ferroelectrics, mapping the polarization. It also provides information about surface charges. EFM can tell us about trapped, injected or induced charges and also the effective charge density.

2.1.5 Kelvin Probe Force Microscopy

Kelvin Probe Force Microscopy (KPFM) is an AFM imaging mode used to produce a map of a surface potential. This is done by measuring the contact potential difference between the AFM probe and the sample at a nanometer spatial resolution. Mathematically, this contact potential difference can be expressed as [29, 30]:

$$V_{CPD} = \frac{(\varphi_{tip} - \varphi_{sample})}{-e} \tag{2.11}$$

where φ_{tip} and φ_{sample} are the work functions of the tip and the sample, and e is the electronic charge. Like EFM, imaging in KPFM is also done in a dual-pass approach. The first pass is used to map the topography in tapping mode, and in the nap pass, the AFM tip is lifted at a constant height (30 nm – 50 nm) above the sample surface. An ac voltage is applied between the tip and the sample that causes an oscillation of the cantilever at its tapping frequency. To null this oscillation, an external dc bias having the same magnitude but opposite polarity to the V_{CPD} is applied. This dc nulling voltage quantitatively measures the contact potential difference between the tip and the sample. In general, the first harmonic component of the electrostatic force between the tip and the sample is expressed as [29, 30]:

$$F_{1w} = \frac{\partial C}{\partial z}(V_{dc} + V_{CPD})V_{ac}\sin(wt) \tag{2.12}$$

In KPFM, the feedback nullifies this oscillating force by applying the dc bias to the tip such that $V_{tip} = -V_{CPD}$.

In ferroelectrics, KPFM can be an indispensable tool for investigating the surface screening charges and the surface potential of the opposite polarization states in the ferroelectric tunnel junctions. Also, it effectively explores the effects of the photogenerated charge carriers on the surface potential in photovoltaic studies.

2.1.6 Typical Experimental Conditions used in this Research

AFM imaging experiments and transport measurements were conducted using an Asylum Research AFM system (MFP 3D). PFM imaging was done using the conductive Pt or Pt/Ir metal-coated AFM probes that typically have a stiffness of around 1.2 N/m to 5.5 N/m and resonance frequency (60 – 90 kHz). PFM measurements were performed with an ac modulation voltage of 0.3 – 0.8V, scan rate of 0.8 – 1 Hz, and a nominal tip load of 50 – 100 nN. The higher tip loading forces ranging from several hundreds of nN up to 2 μN were applied for mechanical writing and stress-induced resistance modulation. CAFM maps and I-V spectroscopy measurements were generally performed with Pt or Pt/Ir-coated sharp AFM probes with a tip radius of 20-30 nm. Additionally, I-V characteristics curves were also obtained on $MoS_2/Pt/SiO_2/Si$ samples using conductive diamond probes that have a tip radius in a range from 100-200 nm, which is an order of magnitude higher than that of Pt-coated tips of radius (20-30 nm). A summary of the AFM probes, their parameters, and the materials used in this research is shown in table 2.1. For the photovoltaic studies on 2D materials, a white light source (SOLA, Lumencor) with an output power of ~ 18 mW was used to illuminate the sample at a maximum light intensity of ~ 200 mW/cm^2.

Thin flakes of graphene and MoS_2 were exfoliated mechanically using the scotch tape method. The flakes were deposited directly onto a ferroelectric or a conductive substrate inside a glovebox filled with Nitrogen gas. An optical microscopy technique identified the location of the several layered thick flakes, and the advanced studies on their electronic transport were done using AFM.

Table 2.1: Description of AFM probes used in this research.

Cantilever type	PPP-EFM	HQ:NSC18/PT	CDT-NCLR-10
Manufacturer	Nanosensors	Micromasch	Nanosensors
Spring constant (units: N/m)	0.5 – 9.5 (Typical: 2.8)	1.2 – 5.5 (Typical: 2.8)	21 – 98 (Typical: 72)
Tip coating	Pt/Ir	Pt	Conductive Diamond
Resonance frequency Min. – Max. (units: kHz)	45 – 115 (Typical: 75)	60 – 90 (Typical: 75)	146 – 236 (Typical: 210)
Tip radius (units: nm)	< 25	< 30	100 – 200
AFM mode	Non-contact AFM, Contact AFM, PFM, CAFM, KPFM, EFM	CAFM (I-V characterization using sharp tip)	CAFM (I-V characterization using dull tip)
Materials studied	Graphene/$LiNbO_3$/Pt, $MoS_2/Hf_{0.5}Zr_{0.5}O_2$/W, 1T” -$MoS_2$/Pt/$SiO_2$/Si	MoS_2/Pt/SiO_2/Si	MoS_2/Pt/SiO_2/Si

References

---

[1] G. Binnig, H. Rohrer, Ch. Gerber, and E. Weibel, App. Phys. Lett. **40**, 178 (1982).

[2] F. Besenbacher, J. V. Lauritsen, and S. Wendt, Nano Today **2**, 30 (2007).

[3] G. Binnig, C. F. Quate, and Ch. Gerber, Phys. Rev. Lett. **56**, 930 (1986).

---

[4] T. Tybell, P. Paruch, T. Giamarchi, and J.-M. Triscone, Phys. Rev. Lett. **89**, 097601 (2002).

[5] T. Tybell, C. H. Ahn, and J.-M. Triscone, Appl. Phys. Lett. **72**, 1454 (1998).

[6] J. Scott, *Ferroelectric Memories* (Springer, Berlin, 2000).

[7] V. Y. Shur, A. Gruverman, V. V. Letuchev, E. L. Rumyantsev, and A. L. Subbotin, Ferroelectrics **98**, 29 (1989).

[8] Q. H. Zhang, L. J. Wang, X. K. Wei, R. C. Yu, L. Gu, A. Hirata, M. W. Chen, C. Q. Jin, Y. Yao, Y. G. Wang, and X. F. Duan, Phys. Rev. B **85**, 020102 (2012).

[9] C.-L. Jia, S.-B. Mi, K. Urban, I. Vrejoiu, M. Alexe, and D. Hesse, Nat. Mater. **7**, 57 (2008).

[10] S. Denev, T. Lummen, E. Barnes, A. Kumar, V. Gopalan, J. Am. Ceram. Soc. **94**, 2699 (2011).

[11] G. Y. Robinson, and R. M. White, Appl. Phys. Lett. **10**, 320 (1967).

[12] J. A. Hooton, and W. J. Merz, Phys. Rev. **98**, 409 (1955).

[13] P. G¨uthner, and K. Dransfeld, Appl. Phys. Lett. **61** 1137 (1992).

[14] A. Gruverman, O. Auciello, H. Tokumoto, Appl. Phys. Lett. **69**, 3191 (1996).

[15] A. Gruverman, O. Kolosov, J. Hatano, K. Takahashi, and H. Tokumoto, J. Vac. Sci. Technol. B **13**, 1095 (1995).

[16] T. Tybell, C. H. Ahn, and J.-M. Triscone, Appl. Phys. Lett. 75, 856(1999).

[17] C. S. Ganpule, A. Stanishevsky, S. Aggarwal, J. Melngailis, E. Williams, and R. Ramesh, Appl. Phys. Lett. 75, 3874 (1999).

[18] S. V. Kalinin, B. J. Rodriguez, J. Shin, S. Jesse, V. Grichko, T. Thundat, A. P. Baddorf, and A. Gruverman, Ultramicroscopy **106**, 334 (2006).

---

[19] A. Gruverman, in *Nanoscale Phenomenon in Ferroelectric Thin Films*, edited by Seungbum Hong (Kluwer Academic Publishers, Dordrecht, 2004).

[20] A. F. Devonshire, Philos. Mag. **42**, 1065 (1951).

[21] S. Hong, (eds). *Nanoscale Phenomenon in Ferroelectric Thin Films* (Springer, New York, 2004).

[22] V. Thery, A. Bayart, J. -F. Blach, P. Roussel, and S. Saitzek. Appl. Surf. Sci. **351**, 480 (2015).

[23] *https://en.wikipedia.org/wiki/Piezoresponse_force_microscopy*

[24] S. V. Kalinin, and D. A. Bonnell, Phys. Rev. B **65**, 125408 (2002).

[25] B. J. Rodriguez, S. V. Kalinin, D. Pelegov, and A. L. Kholkin, *Piezoresponse Force Microscopy and Spectroscopy. In: Bhushan B. (eds) Encyclopedia of Nanotechnology* (Springer, Dordrecht, 2015).

[26] B. J. Rodriguez, C. Callahan, S. Kalinin, and R. Proksch, Nanotechnology **18**, 475504 (2007).

[27] S. Hong, J. Woo, H. Shin, J. U. Jeon, Y. E. Pak, E. L. Colla, N. Setter, E. Kim, and K. No, J. Appl. Phys. **89**, 1377 (2001).

[28] M. P. Murell, M. E. Welland, S. J. O'Shea, T. M. H. Wong, J. R. Barnes., and A. W. McKinnon, Appl. Phys. Lett. **62**, 786 (1993).

[29] S. Sadewasser, and T. Glatzel, Kelvin Probe Force Microscopy, (Springer, Vol 65, Basel, 2017).

[30] W. Melitz, J. Shen, A. C. Kummel, S. Lee, Surf. Sci. Rep. **66**, 1 (2011).

Chapter 3

Resistive switching in ultrathin ferroelectric thin films

3.1 Resistive Switching

Resistive switching is a physical phenomenon characterized by a sudden change in the material's resistance due to the applied electric bias. The peculiar characteristic of resistive switching is a non-volatile change in the resistance that is manifested as the non-linear hysteretic current-voltage (I-V) characteristics curves. This makes it very promising for the development of the non-volatile resistive random-access memory (RRAM) for information storage systems and processing. A typical resistive switching device is realized through a metal/dielectric/metal capacitor-like structure where the applied electric field tunes the electrical resistance of the dielectric layer. Resistive switching has been widely demonstrated in diverse materials such as oxides (HfO_2, CuO), manganites ($LaCaMnO_3$), and oxide-perovskites ($SrTiO_3$) [1, 2]. The resistive switching can be driven by diverse mechanisms, such as electrochemical or redox reactions [1, 3], Schottky barrier modulation [4], crystal phase transformation [5], and electric field-induced filament formation [6].

3.2 Ferroelectric Tunnel Junctions

Ferroelectric materials possess the spontaneous polarization that can be reversed by an electric field, the strain gradient, and the optical illumination [7, 8, 9]. The stability and switchability of the polarization in ultrathin ferroelectric films can be exploited to make a polarization-enabled resistive switching device such as ferroelectric tunnel junctions (FTJ). An FTJ consists of a nanometer-thick ferroelectric layer sandwiched between the two conducting electrodes such that electrons can easily tunnel across this thin insulating ferroelectric barrier. An FTJ is characterized by a figure of merit called tunneling electroresistance (TER), defined as $TER = \frac{R_{OFF}-R_{ON}}{R_{ON}}$, where R_{ON} is the junction resistance measured for the polarization state with a high tunneling current (ON state), whereas R_{OFF} is the junction resistance measured for the opposite polarization state with a lower tunneling current (OFF state). The very concept of the FTJ was first demonstrated as a polar switch by Esaki et al [10]. A schematic of an FTJ is shown in Fig. 3.1 [11].

The electroresistance effect in FTJs can be explained by three different mechanisms as illustrated in Fig. 3.1: electrostatic effect, interface effect, and strain effect. The electrostatic effect originates from the incomplete screening of the bound polarization charges by the metallic electrodes. Incomplete screening of polarization charges results in a finite depolarizing field [12]. This depolarizing field further changes in direction upon polarization switching. Consequently, upon polarization reversal, the electrostatic potential profile seen by the conduction electrons changes, leading to a change in the transmission probability of the tunneling electrons. Similarly, the interface effect considers the displacement of ions within the few unit cells of the metallic electrodes at the electrode/ferroelectric interface in FTJs. The flipping of ferroelectric polarization in FTJs can alter the position of the interfacial ions, which strongly influences the tunneling probability of the transport electrons. The piezoelectric effect includes a change in mechanical deformation (expansion or contraction) of the sample upon polarization reversal, leading to a change in the thickness of the ferroelectric barrier.

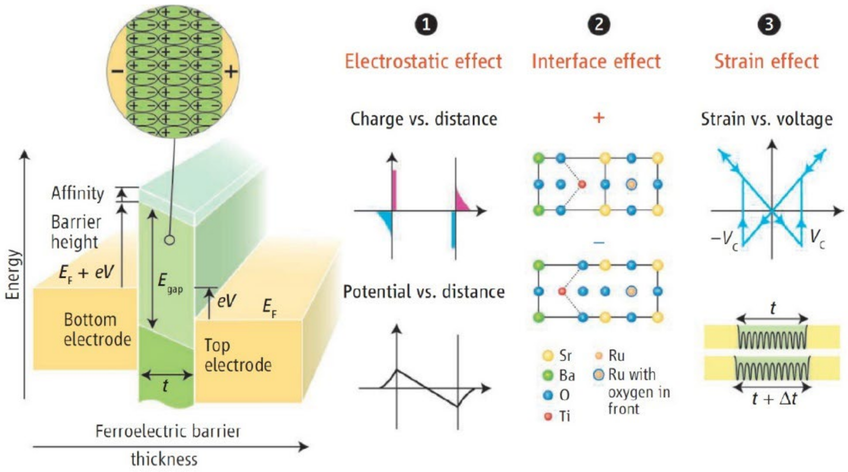

Figure 3.1: A schematic diagram of a ferroelectric tunnel junction, which consists of two-electrodes separated by a nanometer-thick ferroelectric barrier. (E_{gap} is the energy gap. E_f is the fermi energy, V is the applied voltage, V_c is the coercive voltage, t is the barrier thickness, and Δt is the thickness variation under an applied field. This figure is taken from reference [11].

Experimentally, FTJs can be realized by considering ultrathin ferroelectric thin films with a thickness of several nanometers. The electronic transport in FTJs can occur via direct tunneling, Fowler-Nordheim (F-N) tunneling, and thermionic emission [Fig. 3.2a] [13, 14]. Direct tunneling occurs at a low voltage, close to the zero-bias range, while F-N tunneling occurs at a relatively high voltage range. With the increase in ferroelectric barrier thickness, the direct tunneling decreases exponentially, and the thermionic emission dominates the electronic transport. For the thermionic emission, the sign of the electroresistance at the positive and negative voltage range changes [Fig. 3.2b].

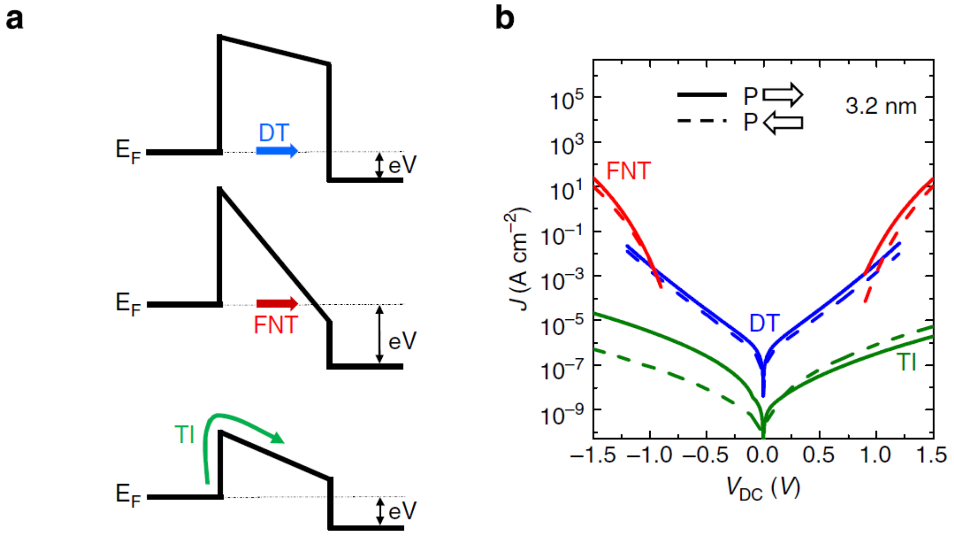

Figure 3.2: Demonstration of different electronic transport mechanisms through ultrathin ferroelectrics. (a) direct tunneling (DT), Fowler-Nordheim tunneling (FNT), and thermionic emission (TI), (b) Corresponding current density (J) versus voltage (V_{dc}) curves in Cu/$BaTiO_3$ (3.2 nm)/$SrRuO_3$. This figure is taken from reference [14].

FTJs can be used to develop the next-generation non-volatile memory and logic devices [15]. A giant electroresistance [12], non-destructive read-out of the information, high scalability, high speed, and low power consumption may facilitate the application of FTJs in RRAM.

3.2.1 Electroresistance Effect in Perovskite-based FTJs

Traditionally, most of the research in FTJs has considered the ferroelectric thin films with perovskite structure. A typical example of it includes graphene/$BaTiO_3$/$La_{0.67}Sr_{0.33}MnO_3$ (graphene/BTO/LSMO) ferroelectric tunnel junctions (FTJs), where the downward polarization state (P_{down}) was found to be highly conducting with respect to the upward polarization (P_{up}) state, resulting in an enhanced TER of around 6000 [16]. It has been also demonstrated that when one of the conducting metallic electrodes, such as Co or Pt [17, 18], is replaced by a doped semiconductor, the TER value increases by 2-3 orders of magnitude due to charge accumulation or depletion at the ferroelectric/semiconductor interface [19, 20]. Such enhanced TER of ~ 10^4 has been achieved by employing BTO-based FTJs with MoS_2, a 2D semiconducting transition metal dichalcogenide, as one of the electrodes [21] with the P_{down} state showing a higher conductivity than the P_{up} state. An interplay between ferroelectric polarization and electronic properties of MoS_2 can result in unusual functionalities. For instance, optically-induced changes of the electronic properties in MoS_2 in MoS_2/BTO/$SrRuO_3$ FTJs via the creation of electron-hole pair result in polarization reversal enabling an optical electroresistance effect [9]. Charge accumulation or depletion at the MoS_2/BTO interface can tune the conductivity of MoS_2, leading to an asymmetric switching of polarization in MoS_2/BTO/$SrRuO_3$ FTJs and gradual change in TER magnitude [21]. In MoS_2/PZT-based devices, a memristive behavior has been demonstrated based on ferroelectric field effect and fine tunability of device resistance through writing/erasing electrically poled nano-domains [22]. The ferroelectric field-effect transistors employing MoS_2 have been shown to exhibit a negative capacitance effect [23, 24, 25]. Despite these advantages, perovskite FE thin films have poor compatibility with complementary metal-oxide-semiconductor (CMOS) technology [26].

3.2.2 Electroresistance Effect in HfO_2-based FTJs

The major drawback of the perovskite-based ferroelectric thin films can be overcome by using ferroelectric hafnium oxide (HfO_2) thin films. The high scalability and compatibility of HfO_2 with the CMOS make it a very promising candidate for future memory device applications. Resistive switching phenomena have been demonstrated in

HfO_2-based films with different dopants [27, 28, 29, 30, 31, 32, 33, 34, 35, 36, 37, 38]. However, most reports on this topic involve HfO_2 films with metal or heavily doped semiconducting electrodes with TER limited to below 100 [29, 34].

The results explained in this Chapter have been published in ref. [39].

3.2.2.1 Enhancement of Electroresistance in MoS_2/ $Hf_{0.5}Zr_{0.5}O_2$ Junctions

In this Chapter, we report a sizable TER of $\sim 10^3$ at 0.8 V read bias in the $MoS_2/Hf_{0.5}Zr_{0.5}O_2$/W/Si heterojunctions detected by a combination of piezoresponse force microscopy (PFM) [40] and conductive atomic force microscopy (c-AFM). A high conductance (ON state) was observed for the polarization in $Hf_{0.5}Zr_{0.5}O_2$ (HZO) oriented toward MoS_2 (upward polarization), while a low conductance (OFF state) was obtained when the polarization was directed away from MoS_2 (downward polarization). The observed effect, which could be described by a Fowler-Nordheim tunneling process, is a result of coupling between the HZO polarization and semiconducting properties of MoS_2 that leads to the modulation of the effective barrier width and height via reversible accumulation/depletion of electrons at the MoS_2/HZO interface.

High-quality 4.5-nm-thick HZO thin films were grown by atomic layer deposition on a Si substrate, using tungsten as a bottom electrode. Thin MoS_2 flakes were mechanically exfoliated from a single crystal using adhesive tape [41] and were deposited on a bare HZO surface inside a nitrogen-filled glovebox. Macroscopic electrical characterization was carried out using a combination of a Keysight 33621A arbitrary waveform generator and a Tektronix TDS 3014B oscilloscope. All biases mentioned in this Chapter are given with respect to the top electrode.

Polarization switchability was initially tested by PFM on the bare HZO surface. Figure 3.3a shows that local PFM hysteresis loops in the as-grown films are shifted to the left indicating a switchable polarization with a preference for the downward state. Next, to quantify the remanent polarization, the TiN top electrodes with Al capping layers were deposited on the HZO film producing an Al/TiN/HZO/W capacitor structure. After the wake-up procedure [42], the macroscopic measurements using the positive-up-negative-down (PUND) technique yielded the remanent polarization (P_r) value of ~13 μC/cm^2 [Fig. 3.3b], which is close to the P_r value of ~17-20 μC/cm^2 reported in the literature [43, 44].

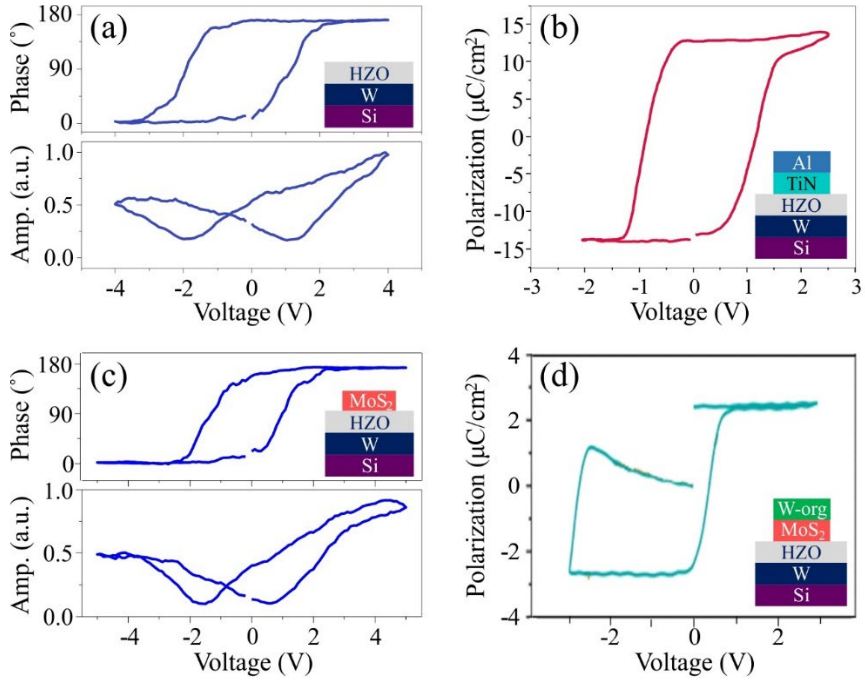

Figure 3.3: Local and macroscopic piezoelectric hysteresis loops. (a) Local PFM phase and amplitude hysteresis loops acquired on bare HZO film surface, (b) a macroscopic remanent P-V loop measured in an Al/TiN/HZO/W capacitor, (c) local PFM phase and amplitude hysteresis loops acquired on the MoS_2/HZO/W heterojunction, (d) a remanent

P-V loop measured in a W-org/MoS_2/HZO/W device. [Data Courtesy: Anastasia Chouprik for (d)]. This figure is taken from reference [39].

After confirming the ferroelectric properties of the HZO films with metal electrodes, the switching behavior of the HZO film with a ~ 4.8 nm thick MoS_2 flake as a top electrode was tested by local PFM spectroscopic measurements. The butterfly-type PFM amplitude loop indicates the switchability of HZO underneath MoS_2 [Fig. 3.3c]. Similar to the as-grown HZO film with a bare surface [Fig. 3.3a], the PFM loops exhibit a horizontal shift toward the negative bias. Note that the PFM hysteresis loop in Fig. 3.3c is a representative loop out of multiple loops taken at multiple locations in each device. To enable macroscopic testing of the MoS_2/HZO/W heterojunction, a tungsten top electrode along with a buffer organic layer was deposited on MoS_2. The P-V loops obtained on such a device reveal a P_r of around 3 $\mu C/cm^2$ in the pristine state, confirming that the ferroelectricity was still preserved after the transfer of MoS_2 onto the HZO film [Fig. 3.3d]. The lower P_r observed in this device might be due to the lower conductivity of the semiconducting MoS_2 electrodes compared to the metallic electrodes resulting in incomplete switching of the polarization in the voltage range of the measurement.

PFM studies have been used to confirm the domain switching and the stability of the polarization in HZO films. PFM imaging of MoS_2/HZO/W in the pristine state reveals a uniform downward polarization state of the ferroelectric film [Figs. 3.4a,b]. After the application of a negative (-4.8 V, 1 s) pulse to MoS_2 via a conductive tip, the whole volume of HZO underneath the MoS_2 flake switched to the upward polarization, which is manifested by the 180° inversion in the PFM phase contrast [Fig. 3.4d]. The upward polarization state is stable against multiple consecutive scans. The PFM amplitude signal of that state is larger than that of MoS_2/HZO/W polarized downward [Fig. 3.4c]. Polarization of MoS_2/HZO/W can be switched by application of a positive (+4.8V, 1s) pulse but only partially [Figs. 3.4e,f]. This incomplete switching of polarization of HZO film underneath MoS_2 is likely due to the change in the electronic properties of MoS_2 mediated by HZO polarization (see discussion below). Reduction in the conductivity of MoS_2 in the depletion mode prevents the applied voltage to drop entirely across the HZO film, thereby leading to an incomplete polarization switching. In addition, the possibility of charge injection/trapping at the MoS_2/HZO interface, which can lead to domain pinning [45], cannot be ruled out.

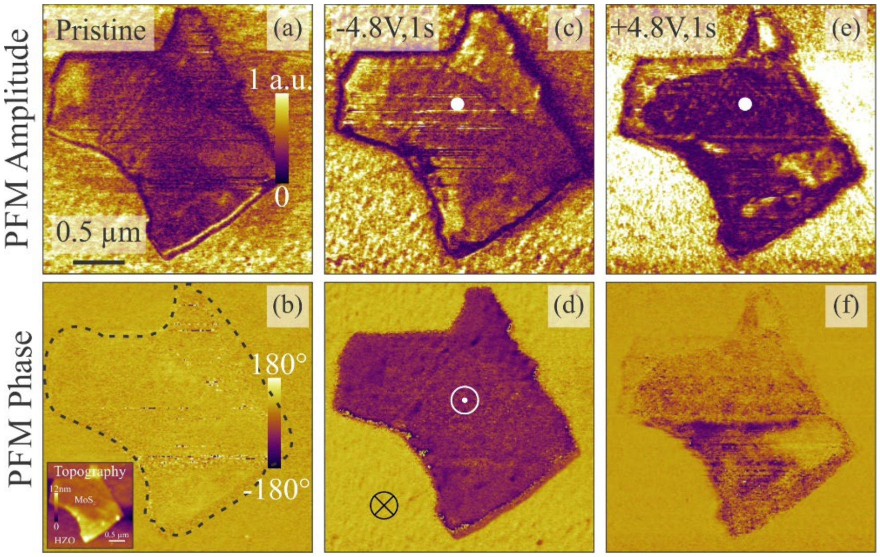

Figure 3.4: Switchability of the $MoS_2/Hf_{0.5}Zr_{0.5}O_2$/W heterojunction. PFM amplitude images (a,c,e) and PFM phase images (b,d,f) obtained in: (a,b) pristine state, (c,d) after -4.8 V pulse, and (e,f) after +4.8 V pulse. The pulse duration is 1 s. The inset and the dashed line in (b) represent the topography of the MoS_2 flake on the HZO surface and the boundary

of the MoS_2 flake, respectively. The white dots in (c) and (e) represent the location of the PFM tip during pulse application. This figure is taken from reference [39].

To explore the resistive switching in the MoS_2/HZO/W heterojunctions, conductivity measurements for fully polarized up and down states were performed by acquiring local current-voltage (I-V) curves in the c-AFM mode. During the I-V measurements, a bipolar triangular waveform with the pulse amplitude of 0.8 V is applied to MoS_2/HZO/W and the current through the junction is collected from the bottom electrode and amplified. For the pristine MoS_2/HZO/W heterojunction in the downward polarization state, the I-V curves reveal negligible current flow indicating a high resistance (OFF) state [Fig. 3.5a, red curve]. On the other hand, in the MoS_2/HZO/W heterojunction polarized upward by application of the -4.8 V pulse, the current shows significant enhancement at a read bias above +/-0.25 V [Fig. 3.5a, black curve] indicating that the device was brought to a low resistance (ON) state. The semi-log I-V curve in Fig. 3.5a and the corresponding R_{OFF}/R_{ON} vs bias plot in Fig. 3.5b show approximately 3 orders of magnitude current increase at a read bias of -0.8 V. That the enhanced TER was due to the semiconducting MoS_2 layer is confirmed by the lack of any resistive switching behavior in the Al/TiN/HZO/W device [Fig 3.5a, inset]. The TER ratio of ~10^3 observed in MoS_2/HZO/W is at least an order of magnitude larger than the TER values reported for HZO-based FTJs with metallic (Pt, TiN, Au) or heavily-doped Si semiconducting electrodes [29, 30, 33]. Numerous I-V plots were taken at multiple locations on the MoS_2 flakes for the upward and downward HZO polarization states and were found to bear reproducible results. Similar reproducibility was observed for multiple MoS_2/HZO/W heterojunctions. Moreover, I-V testing was done at the lower read bias range (±0.8V) to avoid polarization switching in the HZO film underneath MoS_2 and minimize the effect of possible oxygen vacancy migration [34]. Incomplete switching of polarization may reduce the ultimate TER ratio of ~10^3 but at the same time opens a possibility of tuning the electroresistance effect by modulating the fraction of the switched polarization [21].

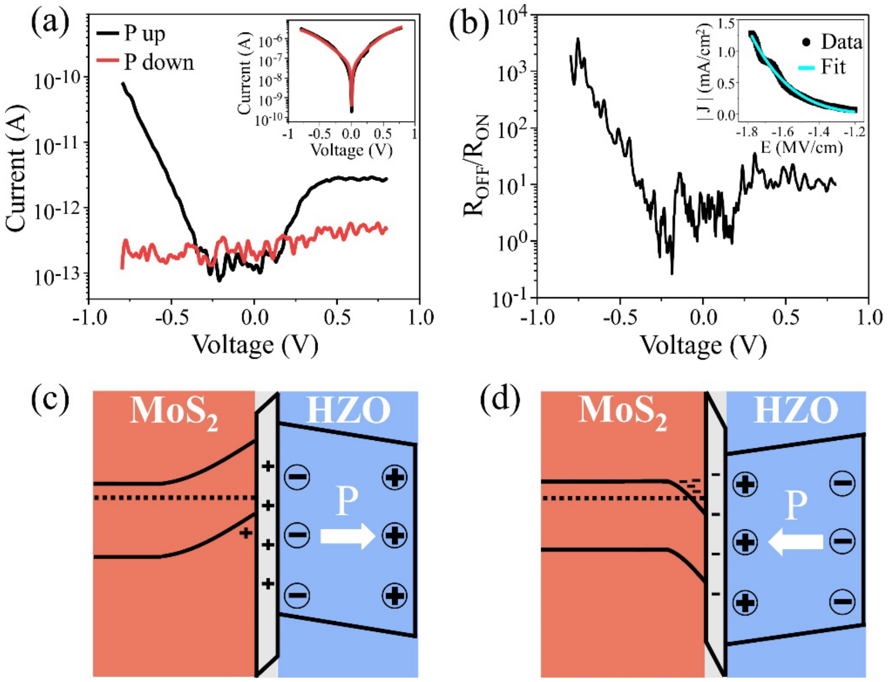

Figure 3.5: Resistive switching behavior of the $MoS_2/Hf_{0.5}Zr_{0.5}O_2/W$ tunnel junctions. (a) I-V curves obtained for the opposite polarization states illustrating a polarization-dependent resistive switching behavior. Inset: I-V characteristics for the two polarization states measured on an Al/TiN/HZO/W device, showing the absence of resistive switching when metallic top and bottom electrodes are used. (b) R_{OFF}/R_{ON} ratio as a function of a DC bias. The inset shows fitting of the current density by Fowler-Nordheim tunneling. (c,d) Schematics of the band structure of the MoS_2/HZO device for different polarization directions. This figure is taken from reference [39].

Interestingly, the resistive switching of the MoS_2/HZO/W heterojunctions displays an opposite behavior in terms of the TER sign as compared to that observed in the MoS_2/BTO/$SrRuO_3$ FTJs [21], which exhibit the ON state for the downward polarization of BTO and the OFF state for the upward polarization. The opposite TER sign can be explained by assuming the n-type conductivity of MoS_2 on top of HZO, which is consistent with earlier reports [46, 47, 48]. The n-type conductivity in MoS_2 was suggested to be induced by interfacial oxygen vacancies at the MoS_2/HfO_2 interface, resulting in the creation of donor levels close to the conduction band edge of MoS_2 [46]. Such oxygen vacancies have also been reported earlier in the HZO thin films [49, 50] and attributed to the redox reactions at the top electrode/HZO interface during annealing [49]. The formation of oxygen vacancies across the film thickness cannot be ruled out either. We note that the exfoliation and deposition of the MoS_2 flakes in different gas environments (ambient conditions used for MoS_2/BTO fabrication in Ref. [21] and dry nitrogen conditions used in this study for MoS_2/HZO) could have also played a role in the opposite TER sign by affecting the composition of the adsorbate molecular layer at the MoS_2/HZO interface, which is known to have a strong effect on the FTJ properties [16]. Furthermore, the presence of an interfacial non-polar dielectric layer at the electrode/ferroelectric interface in FTJs can change the barrier height from a low to high value during polarization switching, consequently resulting in an enhanced TER [51].

The underlying mechanism of the observed resistive switching effect can be explained by considering the accumulation or depletion of electrons (majority carriers in n-type MoS_2) at the MoS_2/HZO interface. When MoS_2/HZO is polarized downward, electrons at the MoS_2/HZO interface will be depleted and the top negative bound polarization charge of HZO at the MoS_2/HZO interface will be screened by positive impurity ions or defects at the interface [Fig. 3.5c]. An increase in the width of the depletion layer at the MoS_2/HZO interface will increase the effective barrier width, thus providing a larger resistance to the current flow through the heterojunction. In contrast, when the polarization is pointing towards the MoS_2 (upward), the positive bound polarization charge will induce an accumulation of electrons at the MoS_2/HZO interface accompanied by a decrease in the effective barrier width [Fig. 3.5d]. Synchrotron-based hard X-ray photoemission spectroscopy (HAXPES) studies have revealed a lower Schottky barrier height when polarization is upward as compared to the downward polarization state [49, 52]. The net effect will be an increase in the current flow through the heterojunction, giving rise to an enhanced electroresistance ratio. Resistive switching could be also affected by band bending at the MoS_2/HZO interface. It has been shown earlier [20] that in $SrRuO_3$/BTO/n-$SrTiO_3$ FTJs, reversible metallization of the BTO barrier caused by band bending would result in a decrease of the effective barrier width by 2-unit cells producing a sizable TER. Likely, such an effect might also occur at the MoS_2/HZO interface, and the polarization orientation corresponding to the ON state is consistent with the theoretical predictions. A lack of a parabolic shape in the conductance (dI/dV) vs voltage plots rule out direct tunneling through the device [53]. A current increase at higher biases is consistent with the Fowler-Nordheim tunneling (FNT) mechanism [13, 54]. Reasonable fitting of the field dependence of current density by the FNT equation [13]: $j_{FN} \sim E^2 * \exp(-B/E)$, ($B = \frac{8\pi\sqrt{2m_{HZO}}\phi^{3/2}}{3he}$, where ϕ is the barrier height, m_{HZO} is the effective electron mass in HZO, E is the electric field, e is an electronic charge, and h is the Planck's constant) suggests that such a tunneling mechanism is highly plausible [Fig. 3.5b, inset].

The value of the constant B was obtained from the fitting, which enabled us to determine the quantity $\sqrt{m_{HZO}}\phi^{3/2}$. Using $m_{HZO} = 0.1m_e$ [55], where m_e is the free electron mass, the interfacial barrier height was found to be ~ 0.64 eV. A similar barrier height of ~ 0.7 eV at the top TiN/HZO interface with the polarization upward was measured in the TiN/HZO/TiN capacitor structures using in-operando HAXPES [52]. The FNT mechanism was also found to be responsible for conduction at high fields in Ti/Al_2O_3/HZO/p-Si heterojunctions [33], although the authors of that study did not specify the barrier height in their devices. Additionally, oxygen vacancy movement in the HfO_2-based ferroelectric thin films under applied electric fields has been demonstrated earlier [27, 34] and such movement could, in principle, contribute to the observed conductivity. However, given the absence of measurable current (within the resolution of our experimental setup) for the downward polarization state, a contribution of oxygen vacancies migration to the observed conductivity can be ruled out.

3.3 Conclusion

In conclusion, a sizeable TER ratio of $\sim 10^3$ was measured in the MoS_2/HZO/W heterojunctions. The observed electroresistance effect can be ascribed to the Fowler-Nordheim tunneling mechanism and polarization-induced modulation of the potential barrier due to accumulation/depletion of majority carriers at the MoS_2/HZO interface. These results were published in reference [39]. This work opens further avenues for exploiting functionalities emerging from combing technologically relevant HfO2-based ferroelectrics with 2D semiconductors.

References

---

[1] R. Waser, and M. Aono, Nat. Mater. **6**, 833 (2007).

[2] Z. Wang, H. Wu, G. W. Burr, C. S. Hwang, K. L. Wang, Q. Xia, and J. J. Yang, Nat. Rev. Mater. **5**, 173 (2020).

[3] R. Waser, R. Dittmann, G. Staikov, and K. Szot, Adv. Mater. **21**, 2632 (2009).

[4] A. Sawa, T. Fujii, M. Kawasaki, and Y. Tokura, Appl. Phys. Lett. **85**, 4073 (2004).

[5] M. Uttig, and N. Yamada, Nat. Mater. **6**, 824 (2007).

[6] Y. Ma, D. Li, A. A. Herzing, D. A. Cullen, B. T. Sneed, K. L. More, N. T. Nuhfer, J. A. Bain, and M. Skowronski, ACS Appl. Mater. Interfaces **10**, 23187 (2018).

[7] A. Gruverman, D. Wu, H. Lu, Y. Wang, H. W. Jang, C. M. Folkman, M. Ye. Zhuralev, D. Felker, M. Rzchowski, C. -B. Eom, and E. Y. Tsymbal, Nano Lett. **9**, 3539 (2009).

[8] H. Lu, C. -W. Bark, D. E. Ojos, J. Alcala, C. -B. Eom, Science **336**, 59 (2012).

[9] T. Li, A. Lipatov, H. Lu, H. Lee, J. -W. Lee, E. Torun, L. Wirtz, C. -B. Eom, J. Iniguez, A. Sinitskii, and A. Gruverman, Nat. Commun. **9**, 3344 (2018).

[10] L. Esaki, R. B. Laibowitz, P. J. Stiles, IBM Tech. Discl. Bull. **13**, 2161 (1971).

[11] E. Y. Tsymbal, and H. Kohlstedt, Science **313**, 181 (2006).

[12] M. Y. Zhuralev, R. F. Sabirianov, S. S. Jaswal, and E. Y. Tsymbal, Phys. Rev. Lett. **94**, 246802 (2005).

[13] D. Pantel, and M. Alexe, Phys. Rev. B **82**, 134105 (2010).

[14] V. Gracia, and M. Bibes, Nat. Commun. **5**, 4289 (2014).

[15] J. F. Scott, Science **315**, 954 (2007).

[16] H. Lu, A. Lipatov, S. Ryu, D. J. Kim, H. Lee, M. Y. Zhuralev, C. B. Eom, E. Y. Tsymbal, A. Sinitskii, and A. Gruverman, Nat. Commun. **5**, 5518 (2014).

---

[17] D. J. Kim, H. Lu, S. Ryu, S. Lee, C. W. Bark, C. B. Eom, and A. Gruverman, Appl. Phys. Lett. **103**, 142908 (2013).

[18] D. Pantel, H. Lu, S. Goetze, P. Werner, D. J. Kim, A. Gruverman, D. Hesse, and M. Alexe, Appl. Phys. Lett. **100**, 232902 (2012).

[19] Z. Wen, C. Li, D. Wu, A. Li, and N. Ming, Nat. Mater. **12**, 617 (2013).

[20] X. Liu, J. D. Burton, and E. Y. Tsymbal, Phys. Rev. Lett. **116**, 197602 (2016).

[21] T. Li, P. Sharma, A. Lipatov, H. Lee, J.-W. Lee, M. Y. Zhuravlev, T. R. Paudel, Y. A. Genenko, C.-B. Eom, E. Y. Tsymbal, A. Sinitskii, and A. Gruverman, Nano Lett. **17**, 922 (2017).

[22] A. Lipatov, T. Li, N. S. Vorobeva, A. Sinitskii, and A. Gruverman, Nano Lett. **19**, 3194 (2019).

[23] F. A. McGuire, Y.-C. Lin, K. Price, G. B. Rayner, S. Khandelwal, S. Salahuddin, and A. D. Franklin, Nano Lett. **17**, 4801 (2017).

[24] M. Si, C.-J. Su, C. Jiang, N. J. Conrad, H. Zhou, K. D. Maize, G. Qiu, C.-T. Wu, A. Shakouri, M. A. Alam, and P. D. Ye, Nat. Nanotechnol. **13**, 24 (2018).

[25] X. Liu, R. Liang, G. Gao, C. Pan, C. Jiang, Q. Xu, J. Luo, X. Zou, Z. Yang, L. Liao, and Z. L. Wang, Adv. Mater. **30**, 1800932, (2018).

[26] M. H. Park, H. J. Kim, Y. J. Kim, W. Lee, T. Moon, K. D. Kim, and C. S. Hwang, Appl. Phys. Lett. **105**, 072902 (2014).

[27] S. Starschich, S. Menzel, and U. Böttger, Appl. Phys. Lett. **108**, 032903 (2016).

[28] B. Max, M. Pešić, S. Slesazeck, and T. Mikolajick, J. Appl. Phys**. 123**, 134102 (2018).

---

[29] F. Ambriz-Vargas, G. Kolhatkar, M. Broyer, A. Hadj-Youssef, R. Nouar, A. Sarkissian, R. Thomas, C. Gomez-Yáñez, M. A. Gauthier, and A. Ruediger, ACS Appl. Mater. Interfaces **9**, 13262 (2017).

[30] A. Chouprik, A. Chernikova, A. Markeev, V. Mikheev, D. Negrov, M. Spiridonov, S. Zarubin, A. Zenkevich, Microelectron. Eng. **178**, 250 (2017).

[31] H. Y. Yoong, H. Wu, J. Zhao, H. Wang, R. Guo, J. Xiao, B. Zhang, P. Yang, S. J. Pennycook, N. Deng, X. Yan, and J. Chen, Adv. Funct. Mater. **28**, 1806037 (2018).

[32] L. Chen, T.-Y. Wang, Y.-W. Dai, M.-Y. Cha, H. Zhu, Q.-Q. Sun, S.-J. Ding, P. Zhou, L. Chua, and D. W. Zhang, Nanoscale **10**, 15826 (2018).

[33] H. Ryu, H. Wu, F. Rao, and W. Zhu, Sci. Rep. **9**, 20383 (2019).

[34] V. Mikheev, A. Chouprik, Y. Lebedinskii, S. Zarubin, Y. Matveyev, E. Kondratyuk, M. G. Kozodaev, A. M. Markeev, A. Zenkevich, and D. Negrov, ACS Appl. Mater. Interfaces **11**, 32108 (2019).

[35] Y. Wei, S. Matzen, T. Maroutian, G. Agnus, M. Salverda, P. Nukala, Q. Chen, J. Ye, P. Lecoeur, and B. Noheda, Phy. Rev. Appl. **12**, 031001 (2019).

[36] J. Yoon, S. Hong, Y. W. Song, J.-H. Ahn, and S.-E. Ahn, Appl. Phys. Lett. **115**, 153502 (2019).

[37] M. C. Sulzbach, S. Estandía, X. Long, J. Lyu, N. Dix, J. Gàzquez, M. F. Chisholm, F. Sánchez, I. Fina, and J. Fontcuberta, Adv. Electron. Mater. **6**, 1900852 (2020).

[38] V. Mikheev, A. Chouprik, Y. Lebedinskii, S. Zarubin, A. M. Markeev, A. V. Zenkevich, and D. Negrov, *Nanotechnology* **31**, 215205 (2020).

[39] P. Chaudhary, P. Buragohain, M. Kozodaev, S. Zarubin, V. Mikheev, A. Chouprik, A. Lipatov, A. Sinitskii, A. Zenkevich, and A. Gruverman, Appl. Phys. Lett. **118**, 083106 (2021).

[40] A. Gruverman, M. Alexe, and D. Meier, Nat. Commun. **10**, 1661 (2019).

[41] K. S. Novoselov, D. Jiang, F. Schedin, T. J. Booth, V. V. Khotkevich, S. V. Morozov, and A. K. Geim., Proc. Natl Acad. Sci. USA. **102**, 10451 (2005).

[42] T. Schenk, U. Schroeder, M. Pešić, M. Popovici, Y. V. Pershin, and T. Mikolajick, ACS Appl. Mater. Interfaces, **6**, 19744 (2014).

[43] J. Müller, T. S. Böscke, U. Schröder, S. Mueller, D. Brauhaus, U. Böttger, L. Frey, and T. Mikolajick, Nano Lett. **12**, 4318 (2012).

[44] H. J. Kim, M. H. Park, Y. J. Kim, Y. H. Lee, T. Moon, K. D. Kim, S. D. Hyun, and C. S. Hwang, Nanoscale **8**, 1383 (2016).

[45] W. L. Warren, D. Dimos, B. A. Tuttle, G. E. Pike, R. W. Schwartz, P. J. Clews, and D. C. McIntyre, J. Appl. Phys. **77**, 6695 (1995).

[46] A. Rai, A. Valsaraj, H. C. P. Movva, A. Roy, E. Tutuc, L. F. Register, and S. K. Banerjee, 2015 73rd Annual Device Research Conference (DRC), Columbus, OH, 189 (2015).

[47] P. Zhao, A. Khosravi, A. Azcatl, P. Bolshakov, G. Mirabelli, E. Caruso, C. L. Hinkle, P. K. Hurley, R. M. Wallace, and C. D. Young, 2D Mater. **5**, 031002 (2018).

[48] K. M. Price, S. Najmaei, C. E. Ekuma, R. A. Burke, M. Dubey, and A. D. Franklin, ACS Appl. Nano Mater. **2**, 4085 (2019).

[49] Y. Matveyev, V. Mikheev, D. Negrov, S. Zarubin, A. Kumar, E. D. Grimley, J. M. LeBeau, A. Gloskovskii, E. Y. Tsymbal, and A. Zenkevich, Nanoscale **11**, 19814 (2019).

[50] A. Chouprik, M. Spiridonov, S. Zarubin, R. Kirtaev, V. Mikheev, Y. Lebedinskii, S. Zakharchenko, and D. Negrov, ACS Appl. Electron. Mater. **1**, 275 (2019).

[51] M. Ye. Zhuralev, Y. Wang, S. Maekawa, and E. Y. Tsymbal, Appl. Phys. Lett. **95**, 052902 (2009).

[52] Y. Matveyev, D. Nergov, A. Chernikova, Y. Lebedinskii, R. Kirtaev, S. Zarubin, E. Suvorova, A. Gloskovskii, and A. Zenkevich, ACS Appl. Mater. Interfaces, **9**, 43370 (2017).

[53] W. F. Brinkman, R.C. Dynes, and J.M. Rowell, J. Appl. Phys. **41**, 1915 (1970).

[54] P. Maksymovych, S. Jesse, P. Yu, R. Ramesh, A.P. Baddorf, and S.V. Kalinin, Science **324**, 1421 (2009).

[55] S. Monaghan, P.K. Hurley, K. Cherkaoui, M.A. Negara, and A. Schenk, Solid-State Electronics **53**, 438 (2009)

Chapter 4

Low-Voltage Domain Wall Memristors in Ultrathin Graphene/$LiNbO_3$/Pt Capacitors

4.1 Memristors

In Chapter 3, we demonstrated a polarization-dependent resistive switching in $Hf_{0.5}Zr_{0.5}O_2$ (HZO)-based ferroelectric tunnel junction (FTJ), where the resistance changes by 3 orders of magnitude when the polarization of HZO is switched from the downward polarization state (OFF state) to the upward polarization state (ON state). In FTJs, each polarization state corresponds to a non-volatile resistance state (ON or OFF) with a fixed value. The other type of resistive switching device is a memristor, an abbreviation of a memory resistor, that exhibits a continuous change of resistance under varying voltage pulse amplitude or pulse duration. The memristor remains in its last resistance state when the current stops flowing through the circuit. The ability to encode the biasing history and multiple analog resistance states make the memristors suitable for future neuromorphic computation architectures. In 1971, Leon Chua introduced the memristor as a fourth circuit element after resistor, capacitor, and inductor [1]. Metal-oxides-based memristors have been demonstrated in Pt/TiO_2/Pt capacitors due to the electric field-induced migration of oxygen vacancies at the Pt/TiO_2 interface [2]. Memristive functionalities have also been explained through other diverse mechanisms such as field-induced trapping or de-trapping of defects at the interface [3], formation and rupture of filaments due to applied electric field [4], and phase changes between the crystalline and amorphous forms [5].

Similarly, ferroelectric memristors may be achieved either by controlling the density of conducting ferroelectric domains and domain walls or due to the polarization-induced accumulation/depletion of charges at the electrode/ferroelectric. For example, in Au/Co/$BaTiO_3$/$La_{0.67}Sr_{0.33}MnO_3$/$NdGaO_3$ (Au/Co/BTO/LSMO/NGO) heterostructures, domains have been shown to exhibit tunable resistance due to the field-induced accumulation/dissipation of oxygen vacancies at Co/BTO interface. This accumulation/dissipation of oxygen vacancies further reduces the barrier height resulting in memristive behavior [6]. Similarly, a memristive behavior has also been achieved by controlling the volume fraction of the switched domains in Co/Au/BTO/LSMO [7]. In addition, the polarization-coupled interfacial trapping/de-trapping of defects can lead to the modification of the Schottky barrier height at the electrode/ferroelectric interface, which in turn can yield a hysteretic I-V and tunable resistance [8]. Apart from these, a continuously tunable resistance has also been achieved through the writing/erasure of the conducting domain walls in ferroelectrics [9, 10, 11, 12, 13, 14].

4.2 Conducting Ferroelectric Domain Walls

Domain walls (DWs) in ferroelectrics exhibit physical properties that differ entirely from the domains they delineate. Deployment of these properties coupled with electrical, mechanical, and optical control of DW geometry, position, and density paves the way for the development of highly scalable electronic devices with enhanced functionality [15]. Based on the perspective of electrical conductivity, DWs can be classified as neutral domain walls (NDWs) or charged domain walls (CDWs). NDWs are commonly found in nature, while CDWs are energetically costly and thus are very rare. The screening of the charges at the domain walls by the mobile ions or defects renders the stability of CDWs.

Usually, 180° Ising walls are NDWs, while the 180° head-to-head (H-H) or tail-to-tail (T-T) DWs are electrically charged. The DW conductivity has been observed in a wide variety of ferroelectric thin films and single crystals such as $BiFeO_3$ (BFO) [16, 17, 18], $Pb(Zr,Ti)O_3$ (PZT) [19, 20], BTO [21], $ErMnO_3$ [22], $LiNbO_3$ (LNO) [23, 24, 19, 20], and boracites [25]. Different mechanisms for such conduction have been proposed in the literature, for instance, Schottky barrier modulation [16], tunneling [26], space charge limited conduction [27, 17], and Poole-Frenkel hopping [28].

In ferroelectric thin films, the seminal work on DW conductivity was first carried out using the multiferroic rhombohedral BFO films that display the conductivity of 109° and 180° DWs as compared to non-conducting 71° DWs [Figs. 4.1a,b] [16]. Further, it was explained using transmission electron microscopy (TEM) analysis that there is a discontinuity of polarization perpendicular to the DW, leading to the formation of the electrostatic potential step [Fig.4.1c]. Density functional theory (DFT) further highlights lowering the band gap at the DWs [Fig.4.1d]. A follow-up work on the domain wall conductivity on BFO thin films by Farokhipoor et al, revealed a conducting nature of 71° DWs as well [29].

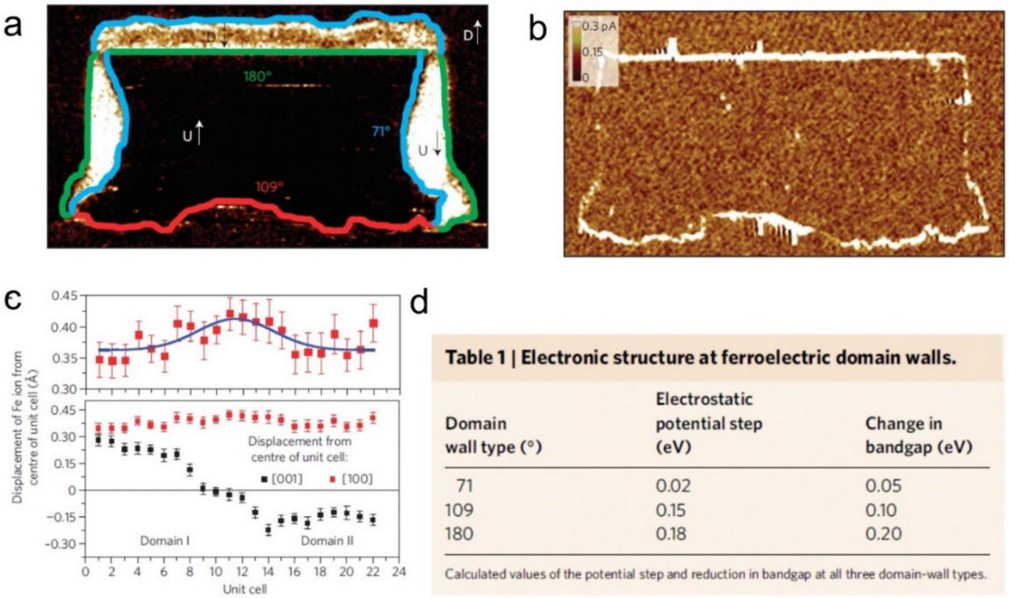

Table 1 | Electronic structure at ferroelectric domain walls.

Domain wall type (°)	Electrostatic potential step (eV)	Change in bandgap (eV)
71	0.02	0.05
109	0.15	0.10
180	0.18	0.20

Calculated values of the potential step and reduction in bandgap at all three domain-wall types.

Figure 4.1: Demonstration of conducting domain walls in $BiFeO_3/SrRuO_3/SrTiO_3$. In-plane PFM image obtained after electrical poling, (b) CAFM taken on the same region showing 109° and 180° DWs are conducting but 71° DW is not, (c) Displacement of Fe atom with respect to Bi atom across the DW extracted from image analysis of TEM obtained data. The top panel represents the increase in the component of polarization normal to the DW. (d) DFT calculated values of electrostatic potential step and reduction in band gap for all three variants of DWs. This figure is taken from reference [16].

In principle, the DW conductance can enhance the leakage, negatively impacting the device performance [30]. However, the creation or erasure of the DW electrically [31] or mechanically [32] offers flexible control over manipulating the density of conducting domain walls. This, in turn, increases the flexibility of using DWs as functional elements in different logic and non-volatile memory devices. A recently demonstrated functional domain wall-mediated memristor in LNO thin films-based capacitor exhibits up to 12 orders of magnitude variation in resistance caused by the injection of strongly inclined conducting DWs [12]. However, due to a high coercive field of LNO, this approach requires high voltages for DW injection or annihilation limiting its application in low-power devices. Also, once the device is set to the ON state by creating a polydomain structure, further modification would require even a higher energy input due to the strong leakage current associated with the presence of conducting DWs.

Another approach to resistance modulation relies upon the change in conductance of the DWs themselves. In the earlier studies on conducting 180° DWs in bulk LNO [24], it was reported that their conductivity could be tuned by manipulating the DW inclination angle with respect to the polar axis. Recent findings by Lu et al show that the DW inclination angle in the LNO thin films can be increased up to 20° by an external bias resulting in a significant enhancement of the DW conductivity [13]. A significant advantage of this approach is its energy efficiency as it does not require any substantial change in domain configuration, hence the resistance modulation can be realized at the voltage level well below the coercive bias. In addition, it allows higher accuracy and reproducibility in programming the resistance states.

4.3 Modulation of domain wall conductance due to super-coercive bias in graphene/$LiNbO_3$/Pt capacitors

In this Chapter 4, we demonstrate and compare the use of both approaches in actual device geometry: the LNO-based memristor with parallel-plate capacitor configuration. We show that partial switching of polarization by application of super-coercive bias allows a change in capacitor resistance by 4 orders of magnitude due to the generation of strongly inclined conducting 180° DWs. A direct correlation between the DW perimeter length and the device resistance is unambiguously established by monitoring the field-induced domain structure evolution and corresponding changes in I-V characteristics. Somewhat smaller but more reproducible modulation of resistance can be achieved by application of sub-coercive bias to the capacitor in the polydomain state due to the change in the DW conductance without polarization reversal. Pulse amplitude and duration serve as the variable parameters in both cases allowing the realization of distinct resistance states.

Now, we uncover the tuning of the device resistance in graphene/LNO/Pt capacitors by varying the domain wall perimeter through partial polarization switching at super-coercive bias. Then, we present an alternative approach that is aimed at modulating the device resistance by varying sub-coercive pulse amplitude or pulse duration that modifies the tilting angle of DWs (instead of altering domain configuration) relative to the polar axis. The results described in this Chapter have been published in reference [14].

The memristive device, investigated in this work, consists of the 500-nm-thick z-cut LNO film prepared by the ion-sliced method [33] on the Pt-coated bulk LNO substrate and multi-layer graphene (Gr) with the thickness of ~20 nm used as a top electrode, yielding a Gr/LNO/Pt parallel plate capacitor. Previous studies have shown that graphene is an efficient top electrode material, which allows domain switching and imaging by PFM [34, 35] Exceptional chemical, mechanical and thermal stability of graphene combined with its high electrical conductivity and low reactivity makes it an attractive top electrode material for the proposed memristive devices.

It has been previously shown that interfacial molecular layers could strongly affect the properties of devices based on a combination of two-dimensional and ferroelectric materials [34, 36]. To achieve well-controlled interfaces between graphene and LNO, the Gr/LNO/Pt structures were fabricated inside a nitrogen-filled glovebox. Prior to the deposition, the LNO surface was cleaned by n-hexane solution. In the as-prepared LNO films, the polarization points away from the bottom electrode in the *z*+, or upward, direction.

Preliminary tests of the bare LNO film reveal a conducting behavior of the 180º DWs created by scanning the film surface with an electrically biased PFM tip. Figures 4.2a,b show PFM and corresponding CAFM images of a series of the periodical stripe domains written by +60 V dc bias where, in agreement with the earlier reports, a strong current signal stems from the DWs only [28]. PFM switching spectroscopy [Fig. 4.2c] yields a strongly shifted hysteresis loop with the coercive voltages of 32 V and -8 V resulting from asymmetric boundary conditions at the top and bottom interfaces. Transmission electron microscopy (TEM) of the sample cross-section [Fig. 4.2d] displays strongly inclined head-to-head DWs with the inclination angle in the range of 10~16°, suggesting that these DWs are charged due to polarization discontinuity.

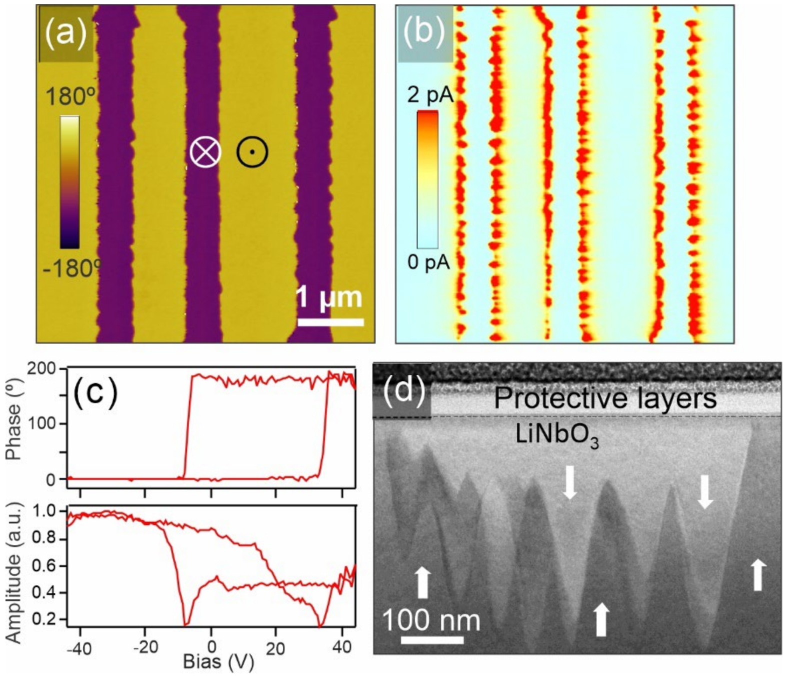

Figure 4.2: Observation of conducting domain walls in LiNbO$_3$ thin films. (a) PFM phase image of the downward stripe domains created by scanning the film surface with the tip under +60 V bias, (b) CAFM map of the written domain pattern acquired using a dc 2 V bias, (c) PFM switching spectroscopy on the bare surface, (d) TEM image of the sample cross-section showing electrically written domains. [Data Courtesy: Zahra Ahmadi for Fig. 4.2d]. This figure is taken from reference [14].

The density of the DWs in Gr/LNO/Pt capacitors can be controlled by controlling the volume fraction of switched domains using a specific combination of super-coercive voltage pulse amplitude and pulse duration. A graphene flake of several square micrometers in size on top of the LNO film [Fig. 4.3a] has been used for electrical biasing of the device. As expected, application of the super-coercive voltage pulse of +33 V to the device initially in the single-domain state results in the formation of the poly-domain structure in an entire area covered by graphene [Figs. 4.3b,c]. Higher magnification PFM imaging in Figs. 4.3d-i illustrates a gradual change in the domain configuration upon increase in the switching pulse amplitude. Domain nucleation initiated by the +31 V pulse [Fig. 4.3d] is followed by the nuclei lateral expansion at +32 V [Fig. 4.3e] and coalescence at +33 V and +34 V resulting in the formation of a maze structure [Figs. 4.3f,g]. Further voltage increase leads to domain merging through annihilation of the DWs and formation of a single-domain state with the downward polarization direction [Fig. 4.3h]. This process is completely reversible as application of the -10 V voltage pulse switched the device back to the upward polarization [Fig. 4.3i].

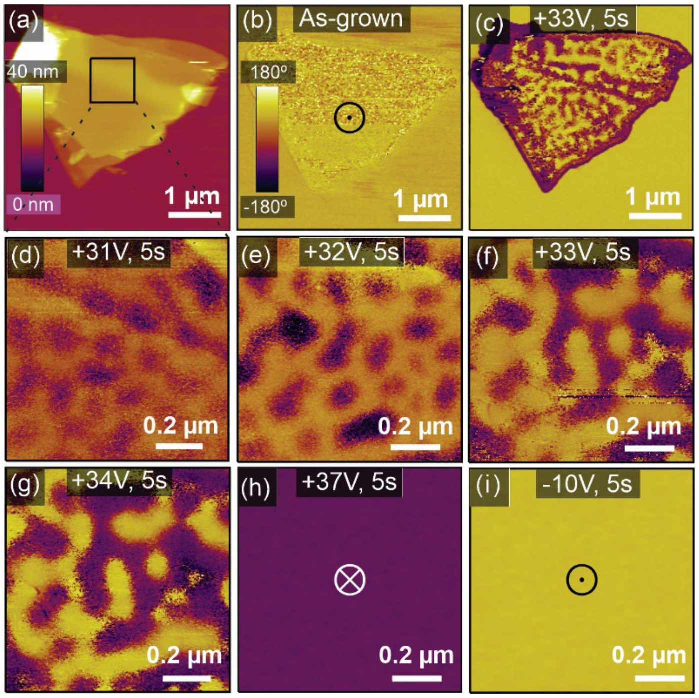

Figure 4.3: Bias-dependent evolution of domain structure in the Gr/LNO/Pt capacitor. (a) Topography of the graphene flake under study, (b-c) PFM phase images of the as-grown state (b), and after +33 V pulse (c), respectively, where polarization is transformed from the upward single-domain state to a polydomain state. (d-i) PFM phase images in the zoomed-in region after application of poling pulses from +31 V to +37 V, and -10 V, respectively. All pulse durations were fixed at 5 s. This figure is taken from reference [14].

The values of resistance of the Gr/LNO/Pt device are measured from the I-V characteristics taken for each domain configuration state [Figs. 4.3d-h]. For the pristine state where the whole LNO volume is polarized upward, these measurements yield a current level as low as 0.2 pA (close to the noise level) [Fig. 4.4a]. As soon as the polydomain state is created by the voltage pulse, the amount of current increases dramatically, from 20 pA for the +31 V up to 1 nA for the +33 V pulse [Fig. 4.4a]. Comparison of this behavior with the corresponding changes in the domain structure in Fig. 4.3 allows us to attribute the current increase to the increasing length of the conductive DWs perimeter in the LNO film. Specifically, using image analysis of the PFM data in Fig. 4.3, we have extracted quantitative information related to domain configuration and plotted the device conductance as a function of the DW perimeter [Fig. 4.4b]. A decrease in the current signal for the +37 V pulse, that drives the device to the downward-oriented single-domain state, is due to the erasure of the DWs in the device interior. The remaining DWs along the edges of the graphene flake (as is mentioned above, the pristine LNO film is in the upward polarization state) explain the finite conductivity of the device completely switched downward. Thus, DW-based memristive devices with the OFF/ON resistance ratio of at least 4 orders of magnitude can be realized in the Gr/LNO/Pt capacitors by employing the control of domain structure by super-coercive voltage.

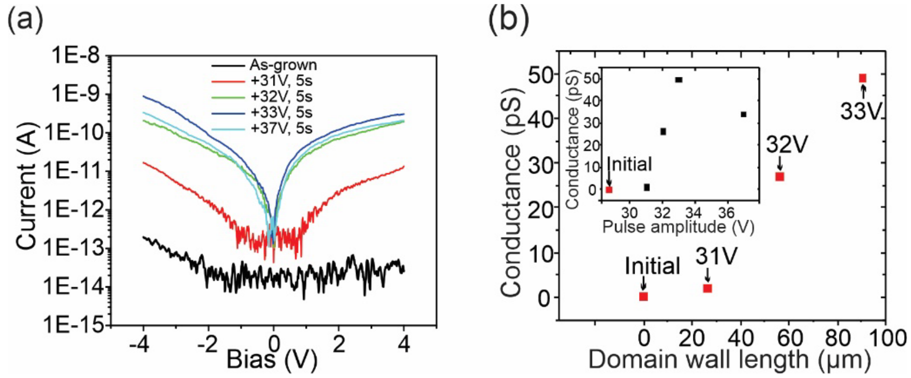

Figure 4.4: Tuning of the Gr/LNO/Pt capacitor resistance by a super-coercive bias. (a) The I-V characteristics in the Gr/LNO/Pt capacitor for the polydomain states created by poling pulses with an amplitude in the range from 31 V to 37 V, corresponding to the states shown in Figs. 2d-2h. (b) Device conductance as a function of total domain wall perimeter length. The inset shows the device conductance as a function of the poling pulse amplitude. This figure is taken from reference [14].

4.4 Modulation of domain wall conductance due to sub-coercive bias

An alternative approach to resistance modulation involves tuning of the DW conductivity rather than changing the domain configuration. As shown in Figs. 4.5a and 4.5b, the device conductance can be tuned by application of the sub-coercive set voltage pulses when the device is in the polydomain state. Figure 4.5a illustrates a dependence of the device conductance on the set pulse amplitude acquired after the poly-domain state was generated by application of the +33 V switching pulse. The set pulse amplitudes (in the range from -3 V to 8 V) are much lower than the coercive voltages, so that the domain structure stays almost intact (there is only a small DW displacement as explained below) while the resistance changes. It can be seen that varying a set pulse amplitude would change the device conductance by 1-2 orders of magnitude and that this process is reproducible. More specifically, an increase in the positive set pulse amplitude will lead to higher conductance, while a negative set pulse would decrease the device conductance. The device conductance could also be modified by varying the set pulse duration [Fig. 4.5b].

Since the domain structure is not affected by the sub-coercive set pulses, the tuning of device resistance must come from the modulation of DW conductance. This effect has been reported in ref [13] on the LNO films without a top electrode and has been attributed to the electrically induced DW bending near the sample surface confirmed by cross-sectional STEM [13]. Specifically, bending the wall away from the polar direction makes it more conducting, while aligning it parallel to the polar axis renders it insulating. This behavior is a result of polarization discontinuity at the inclined walls, which induces electron charge accumulation and a sharp increase in the wall conductivity [37]. In PFM, this DW bending appears as a nanometer-range shift between the DW positions. Indeed, careful comparison of the PFM images of a polydomain structure acquired after application of a positive and negative set bias reveals a DW displacement by about 10 nm even though the domain configuration remains largely intact [Figs. 4.5c and 4.5d].

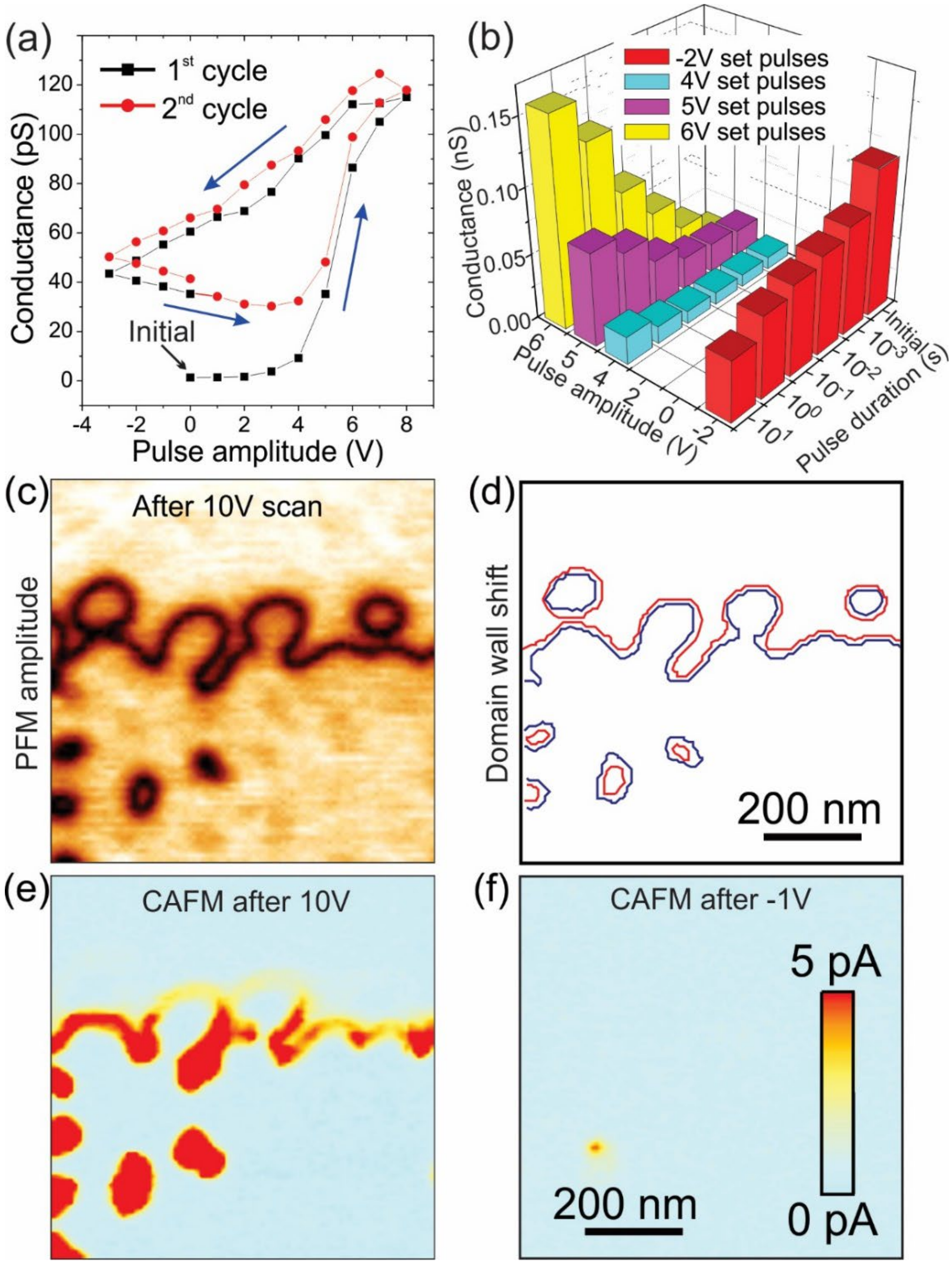

Figure 4.5: Tuning of the Gr/LNO/Pt capacitor resistance by a sub-coercive bias. (a) Conductance in the Gr/LNO/Pt capacitor as a function of set pulse amplitude for a polydomain state created by a poling pulse of 33 V, 1 s. Set pulse duration was fixed at 1 s and conductance readout was at 2 V dc bias. (b) Device conductance as a function of set pulse duration for different set pulse amplitudes. A preset pulse of -2 V, 1 s (for positive

set pulses) or 6 V, 1 s (for negative set pulses) was applied to reset the initial states. (c) PFM amplitude image of polydomain structure on the LNO bare surface. (d) Comparison of the domain wall positions using PFM imaging after application of negative and positive dc set biases: red contour domain lines - after dc 10 V; black contour domain lines - after dc -1 V. While the domain structure is generally intact, there is a slight shift of the domain walls by about 10 nm after dc set biases of opposite polarities. (e,f) CAFM images of the domain walls shown in (c) illustrating a drastic change in domain wall conductance upon application of sub-coercive set bias. This figure is taken from reference [14].

These changes in DW conformation led to the alternation between its high and low conductance states, which could be directly detected by CAFM [Figs. 4.5e and 4.5f, respectively]. Although having a top electrode precludes detection of the individual DW conductance behavior, it can be reliably assumed that the same mechanism results in the conductance change of the polydomain device. Thus, functional low-voltage memristive devices with the OFF/ON resistance ratio of up to 2 orders of magnitude can be realized based on modulation of DW conductance. Note that this approach provides more energy-efficient, precise, and reproducible tuning of device resistance. The resistance ratio could be further enhanced by using the domain structure with a higher density of the DWs. Furthermore, since there is no need for massive electrical cycling of polarization, the fatigue problem ceases to be an issue for this kind of devices.

The poly-domain structures generated in the Gr/LNO/Pt capacitors exhibit remarkably strong retention: we did not observe any noticeable decay over a period of 24 hours. There is a partial decay in the induced conductance states [Fig. 4.6], which could be explained by the gradual change in the DW bending. It should be noted though that, in the

Gr/LNO/Pt capacitors, this relaxation occurs at the time scale that is much longer than that observed for individual DWs [13]. After conductance reduction by about 30% within 1 hour after application of a set pulse, there is a much slower relaxation to the 50% of the initial conductance value within a period of 14 hours. Although not completely non-volatile, this metastable tunable conductance does allow realization of a so-called plasticity effect used in the neuromorphic circuits [12]. Along with the low operation voltage, this renders our Gr/LNO/Pt capacitors viable functional memristors.

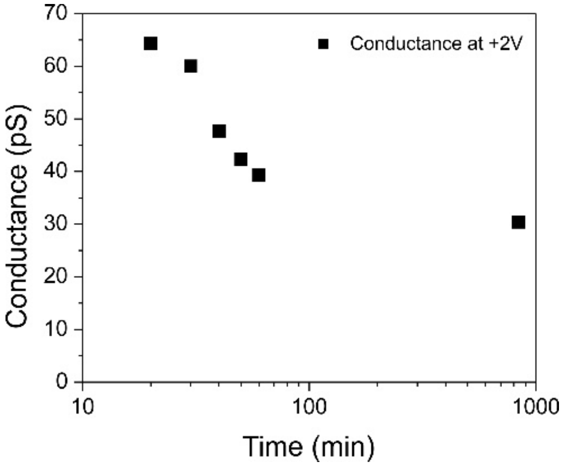

Figure 4.6: A time dependence of conductance of the polydomain graphene/LNO/Pt capacitor. After a relatively significant decay by about 30% within 1 hour after application of a (33V, 5s) set pulse, the conductance stabilizes at about 50% of the initial value. This figure is taken from reference [14].

4.5 Challenges of domain switching using metal top electrode

During our studies, we have also tried using a conducting platinum (Pt) metal as a top electrode to make Pt/LNO/Pt capacitor for polarization switching studies. However, the capacitors easily got burned or delaminated by high current density due to Joule heating, when a voltage close to coercive voltage was applied on it [Figs. 4.7a,b]. This makes the realization of the domain switching and studies of memristive functionality very difficult. Moreover, on using conducting metal-oxide such as ITO as a top electrode, the generated domain structures suffer a relaxation within 24 hours [Figs. 4.8a,b].

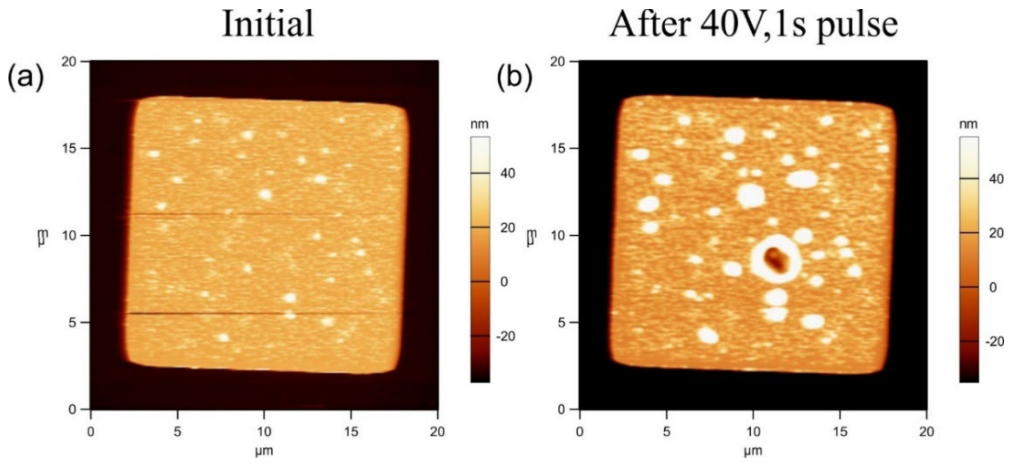

Figure 4.7: AFM topographic images of the 50-nm-thick Pt electrode on top of the LNO thin film: (a) as deposited, (b) after application of a (40V, 1s) pulse. Damage to the electrode can be clearly seen. The capacitor became short-circuited. This figure is taken from reference [14].

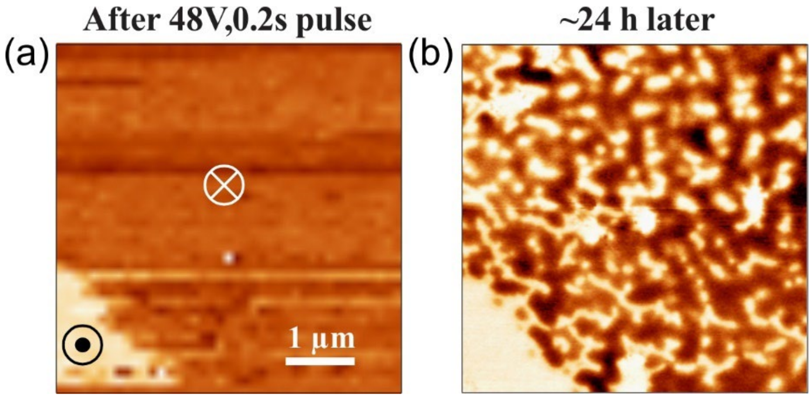

Figure 4.8: Relaxation of domains in the ITO/LNO/Pt capacitors. (a) PFM image of a

domain generated in the LNO capacitor with the ITO top electrode. (b) PFM image of the same region showing relaxation of the generated domain within 24 hours. This figure is taken from reference [14].

On the other hand, graphene, because of its high conductivity and exceptional chemical, mechanical and thermal stability, is robust enough to withstand high current densities and to allow us to generate domain structures with desired density of domain walls by varying the poling pulse amplitude and duration. More importantly, the "transparency" of graphene to PFM imaging allows us to see exactly what happens to the DWs when the capacitor/memristor is in operation. This allowed us to categorically correlate the DW perimeter with the device conductance [Figs. 4.3 and 4.4], which has not been reported elsewhere as the microstructures under the metal top electrodes were inhomogeneous and the entire domain structure could not be imaged at a resolution, at which the perimeters of the DWs could be sensibly monitored. Furthermore, graphene stabilizes the domain structures in Gr/LNO/Pt capacitors as we did not find a significant decay of the domain structures within 24 hours. This might be due to the more efficient screening of polarization charges in Gr/LNO/Pt capacitors.

4.6 Conclusion

In conclusion, we have investigated the resistive switching behavior related to the conducting DWs in the Gr/LNO/Pt capacitors. Two different mechanisms of resistance control have been employed to realize the DW-based memristive devices. The first one involves control of the conducting DW perimeter length via partial polarization reversal induced by super-coercive bias. The second one is based on modulation of the DW conductance via application of non-switching sub-coercive bias to the device in the polydomain state. This mechanism provides significant improvement in terms of energy cost, device resilience, lifetime, accuracy, and reproducibility in controlling the resistance states in the Gr/LNO/Pt DW memristors. A big step forward here is that we have found a solid-state electrode, graphene, which does not get burned by the strong currents induced during the DW writing process in contrast to the delaminating metal electrodes. This finding along with the low-voltage operation paves the way for development of realistic functional memristive devices. Their high tunability demonstrated in this study enables their application in multi-level memory and neuromorphic applications.

References

---

[1] L. O. Chua, IEEE Trans. Circuits. Theory, **18**, 507 (1971).

[2] D. B. Strukov, G. S. Snider, D. R. Stewart, and R. S. Williams, Nature **453**, 80 (2008).

[3] M. H. Boratto, R. A. Ramos Jr, M. Congiu, C. F. O. Graef, L. V. A. Scalvi, Appl. Surf. Sci. **410**, 278 (2017).

[4] D. Lee, D. -J. Seong, I. Jo, F. Xiang, R. Dong, S. Oh, and H. Hwang, Appl. Phys. Lett. **90**, 122104 (2007).

[5] M. Uttig, and N. Yamada, Nat. Mater. **6**, 824 (2007).

[6] D. J. Kim, H. Lu, S. Ryu, C. -W. Bark, C. -B. Eom, E. Y. Tsymbal, and A. Gruverman, Nano Lett. **12**, 5697 (2012).

[7] A. Chanthbouala, V. Gracia, R. O. Cherifi, K. Bouzehouane, S. Fusil, X. Moya, S. Xavier, H. Yamada, C. Deranlot, N. D. Mathur, M. Bibes, A. Barthelemy, and J. Groiller, Nat. Mater. **11**, 860 (2012).

---

[8] A. Chen, W. Zhang, L. R. Dedon, D. Chen, F. Khatkhatay, J. L. MacManus-Driscoll, H. Wang, D. Yarotski, J. Chen, X. Gao, L. W. Martin, A. Roelofs, and Q. Jia, Adv. Funct. Mater. **30**, 200664 (2020).

[9] P. Maksymovych, A. N. Morozovska, P. Yu, E. A. Eliseev, Y. -H. Chu, R. Ramesh, A. P. Baddorf, and S. V. Kalinin, Nano Lett. **12**, 209 (2012).

[10] P. Maksymovich, J. Seidel, Y. H. Chu, P. Wu, A. P. Baddorf, L. -Q. Chen, S. V. Kalinin, and R. Ramesh, Nano Lett. **11**, 1906 (2011).

[11] P. Sharma, Q. Zhang, D. Sando, C. H. Lei, Y. Liu, J. Li, V. Nagarjan, and J. Seidel, Sci. Adv. **3**, e1700512 (2017).

[12] J. P. V. McConville, H. Lu, B. Wang, Y. Tan, C. Cochard, M. Conroy, K. Moore, A. Harvey, U. Bangert, L. -Q. Chen, A. Gruverman, and J. M. Gregg, Adv. Funct. Mater. **30**, 200109 (2020).

[13] H. Lu, Y. Tan, J. P. V. McConville, Z. Ahmadi, B. Wang, M. Conroy, K. Moore, U. Bangert, J. E. Shield, L. -Q. Chen, J. M. Gregg, and A. Gruverman, Adv. Mater. **31**, 1902890 (2019).

[14] P. Chaudhary, H. Lu, A. Lipatov, Z. Ahmadi, J. P. V. McConville, A. Sokolov, J. E. Shield, A. Sinitskii, J. M. Gregg, and A. Gruverman, Nano Lett. **20**, 5873 (2020).

[15] J. R. Whyte, R. G. P. McQuaid, P. Sharma, C. Canalias, J. F. Scott, A. Gruverman, and J. M. Gregg, Adv. Mater. **26**, 293 (2014).

[16] J. Seidel , L. W. Martin, Q. He, Q. Zhan, Y.-H. Chu, A. Rother, M. E. Hawkridge, P. Maksymovych, P. Yu, M. Gajek, N. Balke, S. V. Kalinin, S. Gemming, F. Wang, G. Catalan, J. F. Scott, N. A. Spaldin, J. Orenstein, and R. Ramesh, Nat. Mater. **8**, 229 (2009).

[17] S. Farokhipoor, and B. Noheda, Phys. Rev. Lett. **107**, 127601, (2011).

[18] P. Maksymovych, J. Seidel, Y.-H. Chu, P. Wu, A. P. Baddorf, L. Q. Chen, S. V. Kalinin, and R. Ramesh, Nano Lett. **11**, 1906 (2011).

[19] J. Guyonnet, I. Gaponenko, S. Gariglio, and P. Paruch, Adv. Mater. **23**, 5377 (2011).

[20] P. Maksymovych, A. N. Morozovska, P. Yu, E. A. Eliseev, Y.-H. Chu, R. Ramesh, A. P. Baddorf, and S. V. Kalinin, Nano Lett. **12**, 209 (2012).

[21] T. Sluka, A. K. Tagantsev, P. Bednyakov, and N. Setter, Nat. Commun. **4**, 1808 (2013).

[22] D. Meier, J. Seidel, A. Cano, K. Delaney, Y. Kumagai, M. Mostovoy, N. A. Spaldin, R. Ramesh, and M. Fiebig, Nat. Mater. **11**, 284 (2012).

[23] M. Schröder, A. Haußmann, A. Thiessen, E. Soergel, T. Woike, and L. M. EngAdv. Funct. Mater. **22**, 3936 (2012).

[24] C. Godau, T. Kamfe, A. Thiessen, L. M. Eng, and A. Haußmann, ACS Nano. **11**, 4816 (2017).

[25] R. G. P. McQuaid, M. P. Campbell, R. W. Whatmore, A. Kumar, and J. M. Gregg, Nat. Commun. **8**, 15105 (2017).

[26] J. Seidel, P. Maksymovych, Y. Batra, A. Katan, S.-Y. Yang, Q. He, A. P. Baddorf, S. V. Kalinin, C.-H. Yang, J.-C. Yang, Y.-H. Chu, E. K. H. Salje, H. Wormeester, M. Salmeron, and R. Ramesh, Phys. Rev.Lett. **105**, 197603, (2010).

[27] T. Sluka, A. K. Tagantsev, P. Bednyakov, and N. Setter, Nat. Commun. **4**, 1808 (2013).

[28] M. Schroeder, A. Hauβmann, A. Thiessen, E. Soergel, T. Woike, and L. M. Eng, Adv. Funct. Mater. **22**, 3936 (2012).

[29] S. Farokhipoor, and B. Noheda, Phys. Rev. Lett. **107**, 127601, (2011).

[30] Y. Xiao, V. B. Shenoy, and K. Bhattacharya, Phys. Rev. Lett., **95**, 247603 (2005).

[31] L. McGilly, P. Yudin, L. Feigl, A. Tagantsev, and N. Setter, Nat. Nanotechnol. **10**, 145 (2015).

[32] X. Lu, Z. Chen, Y. Cao, Y. Tang, R. Xu, S. Saremi, Z. Zhang, L. You, Y. Dong, S. Das, H. Zhang, L. Zheng, H. Wu, W. Lv, G. Xie, X. Liu, J. Li, L. Chen, L.-Q. Chen, W. Cao, and L. W. Martin, Nat. Commun. **10**, 3951 (2019).

[33] R. V. Gainutdinov, T. R Volk, and H. H. Zhang, Appl. Phys. Lett. **107**, 162903 (2015).

[34] H. Lu, A. Lipatov, S. Ryu, D. J. Kim, H. Lee, M. Y. Zhuravlev, C. B. Eom, Tsymbal, E. Y. A. Sinitskii, and A. Gruverman, Nat. Commun. **5**, 5518 (2014).

[35] H. Lu, B. Wang, T. Li, A. Lipatov, H. Lee, A. Rajapitamahuni, R. Xu, X. Hong, S. Farokhipoor, L. W. Martin, C. B. Eom, L.-Q. Chen, A. Sinitskii, and A. Gruverman, Nano Lett. **16**, 6460 (2016).

[36] A. Lipatov, A. Fursina, T. H. Vo, P. Sharma, A. Gruverman, and A. Sinitskii, Adv. Electr. Mat. **3**, 1700020 (2017).

[37] E. A. Eliseev, A. N. Morozovska, G. S. Svechnikov, V. Gopalan, and V. Ya. Shur, Phys. Rev. B **83**, 235313 (2011).

Chapter 5

Mechanical Stress Induced Tuning of Resistance in MoS$_2$ Junctions

5.1 Flexoelectricity

One commonly studied electromechanical phenomenon is piezoelectricity, which deals with the linear coupling between the polarization and the homogeneous stress/strain. Inhomogeneous stress applied to a crystal can generate a strain gradient that can induce polarization in the material, leading to a new electromechanical coupling phenomenon called flexoelectricity. In the flexoelectric effect, polarization is linearly coupled with the strain gradient: an electric polarization is generated as a linear response to the applied strain gradient (direct flexoelectric effect), or a polarization gradient in the material generates mechanical stress or strain (converse flexoelectric effect).

In general, the total polarization in a material due to the piezoelectric and the flexoelectric contribution can be given as [1]:

$$P_i = d_{ijk}\sigma_{jk} + \mu_{ijkl}\frac{\partial \varepsilon_{jk}}{\partial x_l} \qquad (4.1)$$

where d_{ijk}, σ_{jk}, μ_{ijkl}, ε_{jk}, and x_l are the tensors of piezoelectric coefficient, stress, flexoelectric coefficient, strain, and position co-ordinate respectively. The first term in equation (4.1) is the polarization due to the piezoelectric effect, and the second term is the polarization associated with the flexoelectric effect. The flexoelectric coefficient tensor (μ_{ijkl}) is a 4-rank tensor. For a cubical symmetry of BaTiO$_3$, the non-vanishing elements of the μ_{ijkl} are

μ_{1111}, μ_{1122}, μ_{1212}, or in matrix notation μ_{11}, μ_{12}, and μ_{44} respectively [2]. Similarly, for bending a beam, the non-vanishing element of μ_{ijkl} is μ_{12} [1].

Flexoelectricity was first theoretically predicted by Mashkevich and Tolpygo [3, 4] and the phenomenological theory was formulated by Kogan [5]. Further, theoretical work on surface and bulk flexoelectric effects due to static and dynamic strain gradient on crystalline solid dielectrics have been elaborated by Tagantsev [6]. Cross and Ma led the seminal experimental work on direct flexoelectricity in the perovskite ferroelectrics [1, 7]. There is a growing interest in scientific research on the effect of flexoelectricity, mainly for two reasons: first, it is a universal phenomenon that is allowed by symmetry to exist in all the crystals of 32-point groups. In centrosymmetric crystals, the application of the strain gradient can break the local inversion symmetry, inducing the polarization. This polarization is analogous to the strain-induced polarization in the piezoelectric materials. Second, flexoelectricity becomes more and more pronounced as the thickness of the materials scales down. A strain difference generated over a small distance can yield a large strain gradient. For instance, in ultrathin films, spatially inhomogeneous strain can produce a giant strain gradient ($\sim 10^8$ m^{-1}), which can lead to a sizeable flexoelectricity making it very useful for the micro-and nano-electromechanical systems.

Owing to the polarity of the flexoelectricity, the strain gradient, unlike stress or strain, can reverse the direction of spontaneous polarization in the ferroelectric materials. The strain gradient can skew the double-well thermodynamic potential and create asymmetric polarization-voltage (P-V) hysteresis loops due to an internal built-in field [8], leading to a preferential polarization state in the ferroelectrics. Therefore, the strain gradient generates an electric field equivalent to an external electric field, also referred to as the flexoelectric field. For ferroelectric thin films grown over a rigid substrate, the substrate-induced strain on the film can be relaxed by a misfit dislocation that can further lead to the flexoelectric effects [9].

The classical theory of the static flexoelectric effect can be explained by considering the Landau-Ginzburg-Devonshire (LGD) theory. The thermodynamic potential density can be expanded in terms of the polarization, strain, and gradient as [6, 10, 11]:

$$\varphi_G = \varphi - \left(\frac{f_1+f_2}{2}\right)\frac{\partial(\varepsilon P)}{\partial x} \tag{4.2}$$

where,

$$\varphi = \frac{1}{2\chi}P^2 + \frac{c}{2}\varepsilon^2 - \frac{f}{2}\left(P\frac{\partial \varepsilon}{\partial x} - \varepsilon\frac{\partial P}{\partial x}\right) - PE - \varepsilon\sigma \tag{4.3}$$

where, $f = f_1 - f_2$ is flexocoupling coefficient tensor. The symbolic notations P, E, χ, c, σ, and ε are polarization, electric field, dielectric susceptibility, elastic constant, stress, and strain respectively. Minimization of the φ_G in equation (4.2) using variational principle and solving the Euler-Lagrange equation ($\frac{\partial \varphi_G}{\partial A} - \frac{d}{dx}\left(\frac{\partial \varphi_G}{\partial\left(\frac{\partial A}{\partial x}\right)}\right) = 0$), ($A = P$ or ε) yields the following equations [6, 10, 11]:

$$P = \chi E + \mu\frac{\partial \varepsilon}{\partial x} \tag{4.4}$$

$$\sigma = c\varepsilon + \frac{\mu}{\chi}\frac{\partial P}{\partial x} \tag{4.5}$$

Equation 4.4 is an electromechanical equation, in which the first term describes the dielectric response, and the second term explains the direct flexoelectric effect where polarization is a linear response to a strain gradient. This second term is called the flexoelectric field, which affects polarization switching in the same way as an external electric field does. In equation 4.5, the first term represents Hooke's law, a linear relationship between the stress (σ) and strain (ε), and the second term describes the converse flexoelectric effect where the stress (σ) is a linear response to a polarization gradient ($\frac{\partial P}{\partial x}$).

Flexoelectricity has several applications in research: for example, in ferroelectrics, it can be used to study the mechanical switching of polarization via strain gradient. Polarization switching in ferroelectric $Pb(Zr,Ti)O_3$ capacitors due to strain gradient generated by the actual bending of the Si substrate has been demonstrated by Gruverman et al [8]. Moreover, mechanical control of polarization reversal in $BaTiO_3$ thin films due to the strain gradient generated by the sharp probe of AFM has been demonstrated by Lu et al [12]. Furthermore, in centrosymmetric materials, the strain gradient can locally break the center of symmetry resulting in the piezoelectric polarization. This, in turn, can induce a significant enhancement of photovoltaic current under illumination, commonly referred to as the flexophotovoltaic effect [13].

In this Chapter, we demonstrate the strain gradient generated by the AFM tip can be used to enhance the electrical transport characteristics of two-dimensional MoS_2 vertical junctions. We have observed continuous modulation of the junction resistance by 4 orders of magnitude achieved by controlling the tip-induced mechanical force. Analysis of the current-voltage (*I-V)* characteristics suggests that both strain and strain gradient play an important role in the tip-induced modification of the MoS_2 band structure: whereas the strain is mainly responsible for the barrier height reduction, the strain gradient imposes a flexoelectric field changing the barrier profile. Furthermore, it has been shown that the tip-induced flexoelectric effect leads to a strong enhancement of the photovoltaic effect in MoS_2. Thus, the electrical resistance of the MoS_2 junctions can be modulated by the combination of light illumination and tip-induced mechanical load. A combination of the optical and mechanical stimuli facilitates the reversible mechanical tuning of resistance of the narrow-band 2D semiconductors and the development of the devices with an enhanced photovoltaic response.

The results described in this chapter are published in the reference [14].

5.2 Mechanical stress-enhanced transport in MoS_2/Pt junctions

MoS_2 flakes were deposited on the Pt/SiO_2/Si substrate by mechanical exfoliation using adhesive tape. The exfoliation process was carried out inside a N_2-filled glovebox. An optical microscope was used to locate and identify few-layered MoS_2 flakes with uniform colors and clean surfaces, which were used in this study. The perpendicular-to-plane electrical transport measurements on exfoliated MoS_2 flakes on Pt substrate were performed using CAFM mode (See Chapter 2, Section 2.1.5 for more details). Figure 5.1a shows an AFM topographic image of a typical MoS_2 flake on the Pt/Si substrate while a sketch in Figure 5.1(b) illustrates the geometry of the experiment. Local *I-V* measurements across the tip/MoS_2/Pt vertical junction performed in the dark [Fig. 5.1c] reveal a significant decrease in junction resistance with the tip load increase. Figure 5.1d summarizes this trend showing almost 4 orders of magnitude decrease in resistance upon the loading force increase from 0.3 μN to 2.1 μN. Note that this force range is well within the elastic deformation regime, and subsequent AFM topographic measurements show no damage to the sample after application of the maximum load. Another noteworthy feature of the *I-V* curves in Figure 5.1c is a transition from the asymmetric rectifying behavior to the more symmetric metallic type with the loading force increase.

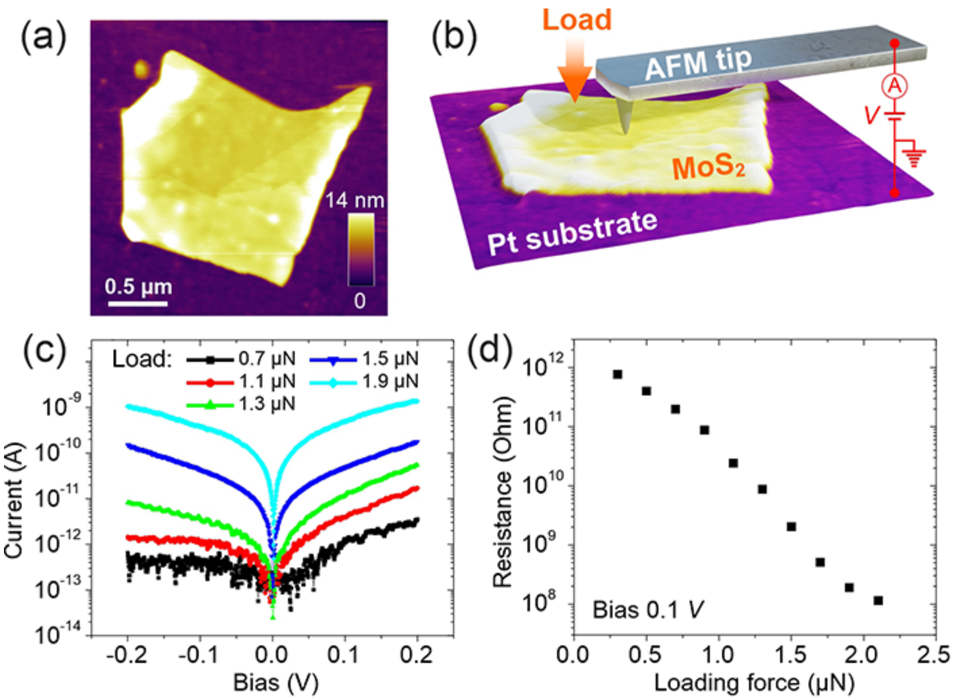

Figure 5.1: Tuning of the MoS_2 resistance by the tip-induced stress. (a) AFM topographic image of an MoS_2 flake on the substrate. (b) Schematic drawing of the experimental setup showing an AFM probe placed on top of the MoS_2 flake to allow transport measurements across the MoS_2 thickness. (c) *I-V* characteristics measured across the 7-nm-thick MoS_2 flake under various AFM tip loading forces. (d) Calculated junction resistance at 0.1 V bias in the tip/MoS_2/Pt junction as a function of tip loading force showing 4 orders of magnitude change in resistance with the tip loading force. This figure is taken from reference [14].

The observed change in the transport characteristics under the mechanical load could be attributed to the contributions of both extrinsic and intrinsic effects. The extrinsic effects are mainly due to the mechanically-induced changes in the tip-sample contact geometry and sample thickness, while the intrinsic effects result from the changes in the MoS_2 band structure and the barrier profile across the junction.

We have estimated the changes in the tip-sample contact geometry and sample thickness within the framework of Hertzian contact mechanics [15] where the tip is modeled as a spherical indenter. It has been found that due to these extrinsic effects, the junction resistance would change only by a factor of less than 4 when the tip loading force was increased from 0.3 μN to 2.1 μN. Therefore, it must be concluded that the observed changes in *I-V* behavior are mainly due to the intrinsic effects related to the modification of the band structure across the junction and not due to the change in the tip-contact geometry.

To understand the conduction mechanism in the tip/MoS_2/Pt junctions, we have fitted the *I-V* curves in Fig. 5.1c by the thermionic emission model, which considers the charge transport over the metal-semiconductor Schottky barrier [16]. In this model, the current density *J* can be expressed as [16]:

$$J = A^{*}T^{2}\exp[-\frac{1}{k_{B}T}(\varphi_{B} - \sqrt{\frac{e^{3}E}{4\pi\varepsilon}})], \tag{4.6}$$

where A^* is the effective Richardson constant, φ_B is the Schottky barrier height, *E* is the electric field across the Schottky barrier, and the rest have their usual meanings. The depletion width (x_d) of the MoS_2 for the metal-semiconductor Schottky contact is calculated as [16]:

$$x_{d} = \sqrt{\frac{2\varepsilon(\varphi_{i} - V)}{eN_{d}}} \tag{4.7}$$

where ε is the dielectric constant of MoS_2, φ_i is the built-in potential, *V* is the applied voltage, and N_d is the carrier concentration. An electron concentration in the order of 10^{17} cm^{-3} was reported for fresh flakes [17], an order of magnitude estimation of the depletion layer width gives $x_d \sim 10$ nm, which is larger than the MoS_2 thickness itself in our junctions. Thus, MoS_2 in the junction is in the fully depleted regime making a flat band model a good approximation implying that log (*I*) should linearly scale with the square root of the applied voltage *V* [1616].

Figure 5.2a shows linear fittings of log (*I*) vs $V^{1/2}$ plots for different loading forces providing strong support for the thermionic emission as a conduction mechanism. Figure 5.2b shows the extracted barrier height as a function of the tip loading force using $A^* = 54$ Acm^{-2} K^{-2} for MoS_2 [18] along with the simplified band structure (the asymmetric barrier profile is due to the built-in field discussed below). The barrier height decreases by almost 0.16 eV at a tip loading of 2.1 μN. This effect could be attributed to the progressive reduction of the interlayer distance in MoS_2 under growing pressure, which effectively reduces its bandgap [19, 20, 21].

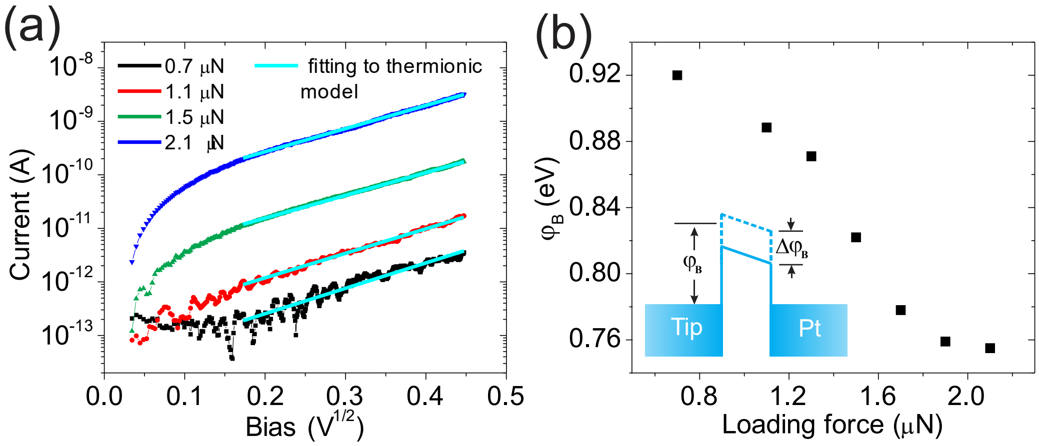

Figure 5.2: Loading force effect on the I-V characteristics and a barrier height. (a) Linear fitting of log (*I*) vs $V^{1/2}$ by the thermionic emission model in the bias range of 0.16 V to 0.45 V. (b) The calculated Schottky barrier height (φ_B) as a function of tip loading force. The inset shows a simplified flat band structure and the lowering of barrier height. This figure is taken from reference [14].

However, this simple picture does not explain the transition from highly asymmetric rectifying *I-V* characteristics to more symmetric *I-V* curves under the increasing load [Fig 5.1c]. The asymmetric *I-V* curves at relatively low loads suggest a presence of the upward (pointing to the tip) built-in electric field in the tip/MoS_2/Pt junction. We attribute this built-in field to the asymmetric tip/MoS_2 and MoS_2/Pt interfaces due to the work function difference between the tip and the substrate. Although both the tip and the substrate are Pt-coated, Pt can exhibit significantly different work functions depending on the deposition method and interface properties [22, 23]. Indeed, our Kelvin probe measurements revealed a tip-substrate potential difference of about 0.34 eV. Symmetrization of the *I-V* curves under pressure implies a reduction of the built-in field, which means that an additional mechanism must be at play.

5.3 Flexophotovoltaic effect in MoS_2

Several experiments have shown that mechanical stress applied via the AFM tip to ultrathin films produces a giant strain gradient resulting in a profound flexoelectric effect that could significantly affect their dielectric, electromechanical and transport properties [12, 13, 24, 25, 26]. With the strain gradient easily reaching 10^6 m^{-1} under the AFM tip [12], a flexoelectric field could be of the order of several MV/cm. It is, thus, reasonable to expect, that tip-induced pressure could modify the band structure of a semiconductor yielding a significant change in resistance [24, 25]. Specifically, for the tip/MoS_2/Pt junction case, at a relatively high tip load, the strain gradient may lead to a downward (pointing to the substrate) flexoelectric field that would compensate the built-in field, resulting in a more symmetric barrier profile across the junction.

Evidence of the tip-induced flexoelectric effect comes from the flexophotovoltaic measurements, where a clear shift of the photocurrent onset with the tip load increase has been observed. Figures 5.3(a) and (d) display two sets of the *I-V* curves measured in the dark and under illumination for a minimum loading force of 50 nN in the tip/MoS_2/Pt junctions with the 8-nm-thick and a 35-nm-thick MoS_2 barriers, respectively. (50 nN is a typical contact force used in the conventional topographic measurements; it is assumed that at this loading force no tip-induced stress effects take place.) It can be seen that in thinner MoS_2, the photocurrent onset occurs at a positive open-circuit voltage [Fig. 5.3d], while in 35-nm-thick MoS_2 it shifts to the negative voltage range [Fig. 5.3a]. As mentioned above, this shift can be attributed to the presence of the upward-oriented built-in field resulting from the asymmetric top and bottom interfaces, which becomes more evident when reducing the MoS_2 thickness. Under the tip-applied pressure, the open-circuit voltage shifts to the right as is illustrated by the I-V curves in Figs. 5.3(b) and (e) and the shift dependences on the loading force for MoS_2 of both thicknesses are shown in Figs. 5.3(c) and (f). This trend can be explained by the effect of the tip-generated flexoelectric field oriented downward, which balances out the oriented-upward built-in field in agreement with the observation of the *I-V* curves becoming more symmetric under the applied pressure. The average flexoelectric field generated by the tip-induced strain is estimated to be in the order of 0.6 MV/cm in the low load regime, which is in the same order of magnitude calculated and measured in $BaTiO_3$ thin films under the AFM tip pressure, assuming the flexoelectric coefficients are in the order of several nC/m [26].

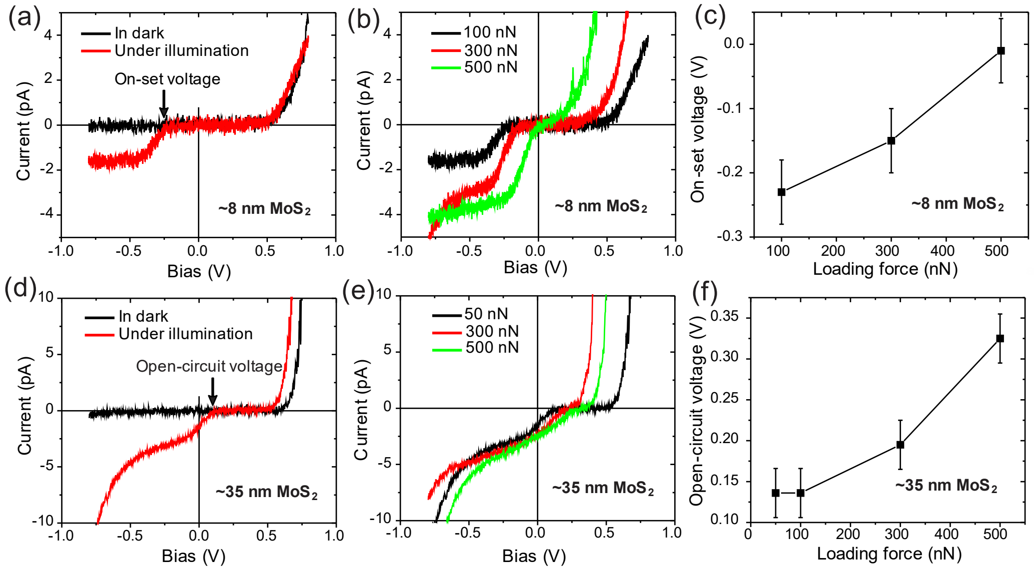

Figure 5.3: Photovoltaic effect in the tip/MoS_2/Pt junctions. (a,d) *I-V* characteristics acquired in the dark and under illumination at a minimum loading force of 50 nN in the 8-nm-thick (a) and 35-nm-thick (d) MoS_2 junctions. (b,e) *I-V* characteristics under illumination for different tip loading forces measured in the 8-nm-thick (b) and 35-nm-thick (d) MoS_2 junctions. (c,f) Tip load dependence of the open-circuit voltage in the 8-nm-thick (c) and 35-nm-thick (f) MoS_2 junctions. This figure is taken from reference [14].

The sharp probe of AFM generates the stress and strain gradient that can modify the barrier of the MoS_2 junctions in our studies. Figure 5.4 presents a simplified illustration of a combined effect of the tip-induced strain and strain gradient on the tip/MoS_2/Pt band structure, which in the absence of the tip-induced stress exhibits an asymmetric barrier profile [Fig. 5.4a] and the rectifying *I-V* characteristics in the absence of the tip-induced stress [Fig. 5.1c]. Homogeneous strain leads to barrier lowering [Fig. 5.4b] due to the MoS_2 bandgap reduction [27, 18], while the strain gradient changes the barrier profile due to the generated flexoelectric field [Fig. 5.4c]. A combination of both effects leads to the overall modification of the barrier profile [Figure 5.4d] resulting in an enhanced conductivity characterized by the symmetric I-V curves. Although this description is in qualitative agreement with the experimental results, in reality, the effect of the highly non-uniform strain generated by the AFM tip is likely more complicated.

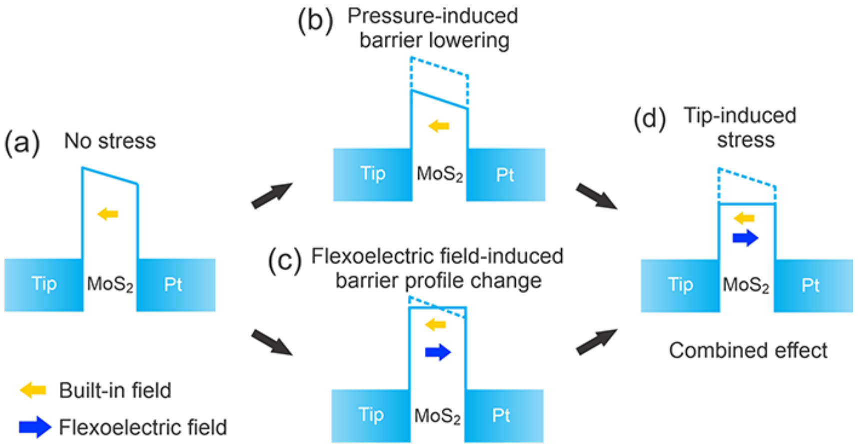

Figure 5.4: Evolution of the energy barrier profile and height in the tip/MoS_2/Pt junctions due to the tip-induced strain and strain gradient. (a) Asymmetric barrier in the absence of applied stress due to the upward built-in field. (b) Lowering of the barrier height due to the homogeneous strain. (c) A change in the barrier profile due to the strain gradient. (d) Overall modification of the barrier shape due to the tip-induced stress. This figure is taken from reference [14].

An interesting outcome of the observed pressure-induced increase in the MoS_2 conductivity is the mechanical enhancement of the photovoltaic effect [28]. Figure 5.5 illustrates the tuning of the tip/MoS_2/Pt junction conductivity by different stimuli. Enhanced conductivity can be achieved by either tip pressure or by optical illumination. Moreover, in the combined excitation approach, when MoS_2 is subjected to tip pressure and illuminated by white light, we observe a further significant (an order of magnitude) increase of the MoS_2 conductivity. This combined excitation opens the possibility of the development of photo-electromechanical devices with broadly tunable transport characteristics.

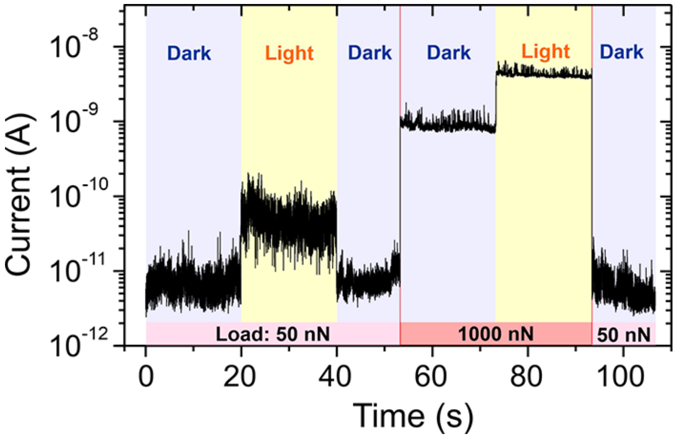

Figure 5.5: Demonstration of tuning of the tip/MoS_2/Pt junction resistance by light, tip load, and a combination of light and tip load. The tip loading force is controlled at low load (50 nN) and high load (1 μN) conditions. Current is recorded at the dc bias of 0.5 V. This figure is taken from reference [14].

5.4 Conclusion

In conclusion, we have analyzed the electrical transport behavior in the tip/MoS_2/Pt junctions under the AFM tip-generated mechanical pressure. It has been shown that both strain and strain gradient play important roles in the modification of the MoS_2 band structure allowing resistance modulation by 4 orders of magnitude. In addition, the tip-induced flexoelectric effect strongly impacts the photovoltaic effect in MoS_2 opening a possibility of combined photomechanical tuning of resistance. It is worth mentioning that this approach is applicable to any narrow-band 2D semiconductor and, as such, could enable devices with enhanced photovoltaic response.

References

---

[1] W. Ma, Phys. Stat. Sol. (B) **245**, 761, (2008).

[2] W. Ma, and L. E. Cross, Appl. Phys. Lett. **78**, 2920 (2001).

[3] V. S. Mashkevich, and K. B. Tolpygo, I. Sov. Phys. JETP **5**, 435 (1957).

[4] K. B. Tolpygo, Sov. Phys. Solid State **4,** 1297 (1963).

[5] S. M. Kogan, Sov. Phys. Solid State **5**, 2069 (1964).

[6] A. K. Tagantsev, Phys. Rev. B **34**, 5883 (1986).

[7] L. E. Cross, J. Mat. Sci. **41**, 53 (2006).

[8] A. Gruverman, B. J. Rodrigues, A. I. Kington, and R. J. Nemnich, Appl. Phys. Lett. **83**, 728 (2003).

[9] J. W. Matthews, A. E. Blakeslee, J. Cryst. Growth **27**, 118 (1974).

[10] P. V. Yudin, and A. K. Tagantsev, Nanotechnology **24**, 432001 (2013).

[11] P. Zubko, G. Catalan, and A. K. Tagantsev, Annu. Rev. Mater. Res. **43**, 387 (2013).

[12] H. Lu, C. -W. Bark, D. Esque de los Ojos, J. Alcala, C. B. Eom, G. Catalan, and A. Gruverman, Science **336**, 59 (2012).

[13] M. M. Yang, D. J. Kim, and M. Alexe, Science **360**, 904 (2018).

[14] P. Chaudhary, H. Lu, M. Loes, A. Lipatov, A. Sinitskii, and A. Gruverman, Nano Lett. **22**, 1047 (2022).

[15] A. C. Fischer-Cripps, *Introduction to Contact Mechanics* (Springer, New York, 2000).

[16] S. M. Sze and K. K. Ng, *Physics of Semiconductor Devices*, *3rd edition* (John Wiley & Sons, Inc., Hoboken, 2006).

[17] M. D. Siao, W. C. Shen, Z. W. Chang, M. C. Shih, Y. P. Chiu, and C. -M. Cheng, Nat. Commun. **9**, 1442 (2018).

---

[18] Y.-F. Lin, W. Li, S.-L. Li, Y. Xu, A. Aparecido-Ferreira, K. Komatsu, H. Sun, S. Nakaharai, and K. Tsukagoshi, Nanoscale **6**, 795 (2014).

[19] A. C. Gomez, R. Roldan, E. Cappelluti, M. Buscema, F. Guinea, H. S. J. van der Zant, and G. A. Steele, Nano Lett. 13, 11, 5361 (2013).

[20] T. Li, and G. Galli, J. Phys. Chem. C **111**, 16192 (2007).

[21] E. Scalise, M. Houssa, G. Pourtois, V. Afanas'ev, and A. Stesmans, Nano Res. **5**, 43 (2012).

[22] G. N. Derry, and J.-Z. Zhang, Phys. Rev. B, **39**, 1940 (1989).

[23] J. Billy, and M. Abon, Surf. Sci. **146**, L525 (1984).

[24] L. Wang, S. Liu, X. Feng, C. Zhang, L. Zhu, Y. Qin, and Z. L. Wang, Nat. Nanotechnol. **15**, 661 (2020).

[25] S. M. Park, B. Wang, T. Paudel, S. Y. Park, S. Das, J. R. Kim, E. K. Ko, H. G. Lee, N. Park, L. Tao, D. Suh, E. Y. Tsymbal, L. -Q. Chen, T. W. Noh, and D. Lee, Nat. Commun. **11**, 2586 (2020).

[26] J. Očenášek, H. Lu, C. W. Bark, C. B. Eom, J. Alcalá, G. Catalan, and A. Guverman, Phys. Rev. B **92**, 035417 (2015).

[27] A. P. Nayak, S. Bhattacharyya, J. Zhu, J. Liu, X. Wu, T. Pandey, C. Jin, A. K. Singh, D. Akinwande, and J. -F. Lin, Nat Commun. **5**, 3731 (2014).

[28] J. Jiang, Z. Chen, Y. Hu, Y. Xiang, L. Zhang, Y. Wang, G. -C. Wang, J. Shi, Nat. Nanotechnol. **16**, 894 (2021).

Chapter 6 Demonstration of ferroelectric polarization in two-dimensional 1T”-MoS_2

6.1 Two-dimensional ferroelectricity

One of the long viewed topics in classical physics is the ferroelectricity as evident from the abundant research works on the ferroelectric properties in traditional perovskites (structural formula: ABO_3): $BaTiO_3$ [1], $Pb(Zr,Ti)O_3$ [2], $BiFeO_3$ [3], $PbTiO_3$ [4] etcetera, and organic ferroelectrics: polyvinylidene fluoride (PVDF) and its copolymers: polyvinylidene fluoride trifluoroethylene (PVDF-TrFE) [5]. Many of these ferroelectric materials have already been used in technologically important applications such as non-volatile memory [6], field-effect transistors [7], and photonic devices [8]. Earlier reports on these materials have found that robust ferroelectricity can occur in millimeter-thick single crystals, bulk ceramics, and thin films of film thickness in a range from 100 nm to several microns. As the size of the ferroelectric materials scales down to a two-dimensional (2D) limit, then the size-dependent factors, such as depolarization field and structural instabilities due to the surface reconstruction, become more predominant, which can affect the ferroelectricity. A reduction in the Curie temperature and the disappearance of the ferroelectricity in perovskites have been reported to occur while scaling down the film thickness below the critical film thickness [9, 10]. However, with the appropriate choice of the electrodes (for example, electrodes with short screening lengths) and the growth of better-quality thin films, the ferroelectricity has been demonstrated in the ultrathin ferroelectric thin films with thickness in the order of several unit cells such as $Pb(Zr_{0.2}Ti_{0.8})O_3$ (1.5 uc) [11], $BaTiO_3$ (2 uc) [12], and $BiFeO_3$ (1 uc) [13].

Nowadays, there is a growing interest in research in 2D materials due to their distinct physical, chemical, optical, electrical, and electronic properties that may increase their potential for applications in nanoelectronics [14]. 2D van der Waals materials are layered structures that have strong in-plane covalent bonds between the atoms and weak interlayer van der Walls bonds. 2D van der Waals ferroelectric materials have been shown to exhibit ferroelectricity, which is ascribed to the loss of a center of inversion symmetry.

The possibility of a stable polar state in 2D van der Waals materials has been explained by different mechanisms such as polar distortion [15, 16], defect engineering [17], surface functionalization [18, 19], and interlayer charge transfer [20]. The theory has predicted that the in-plane trimerization in monolayer 1T-MoS_2, one of the polymorphs of MoS_2, could break the inversion symmetry and introduce the out-of-plane polarization [15]. In addition, stacking of structurally symmetric nonpolar monolayers can break the inversion symmetry and introduce ferroelectricity in the bulk structure, as was observed experimentally for T_d-WTe_2 [21]. Ferroelectricity in In_2Se_3 is related to the intrinsic polar symmetry and polarization was predicted to arise due to the vertical displacement of Se atoms [16]. Chemical functionalization can also transform 2D materials into the ferroelectric state as predicted for functionalized phosphorene[18] and graphanol [19]. Furthermore, first-principles calculations reveal an induced switchable out-of-plane polarization in CrI_3 via the engineering of iodide (I) vacancies [22]. Density functional theory (DFT) predicts that the transfer of charges between the interlayers of bilayer hexagonal boron nitride (h-BN) leads to an induced out-of-plane polarization that can be switched by the interlayer translation by one B-N bond length [20]. The integration of the miniaturization of the next-generation non-volatile memory and logic devices.

So far, the occurrence of ferroelectricity has been theoretically predicted in the monolayer to few-layered thick 2D materials; however, the experimental verification of the ferroelectricity is very limited due to the generally small values of polarization and increased leakage, which make any dielectric and ferroelectric measurements challenging [14]. Several notable examples of experimental observation include the out-of-plane polarization in multilayered α-In_2Se_3 using a combination of structural, optical, and electrical characterization [23, 24], polarization-dependent bi-stable conductance in 2-3 layered WTe_2 [25], robust in-plane polarization in SnTe and SnS [26, 27], domain structure in WTe_2 single crystals [25] and $CuInP_2S_6$ flakes [28], and switchable in-plane polarization in thin flakes of hybrid perovskites [29].

In this Chapter, we demonstrate emergent ferroelectricity in the recently reported 1T”-MoS_2 phase [30]. The distorted trigonal 1T”-MoS_2 phase belongs to the space group $P3m1$, which has two topologically equivalent crystal structures related to each other by the inversion symmetry operation, designating its ferroelectric nature. Polarization reversal in the 1T”-MoS_2 phase has been realized via a voltage-free approach by using a tip of a scanning probe microscope (SPM) pressed against the sample surface. Facilitated by the flexoelectric effect, a tip-induced strain gradient generates a flexoelectric field much like an applied external voltage, but in a manner more resilient to the electronic screening and leakage, resulting in a stable bi-domain configuration with out-of-plane polarization detected by piezoresponse force microscopy (PFM). First-principles calculations confirm the presence of spontaneous polarization in 1T”-MoS_2 as well as the existence of stable head-to-head (H-H) and tail-to-tail (T-T) dipole configurations, which have been experimentally revealed by the experiments involving the flipped MoS_2 flakes.

The results of this chapter have been published in reference [31].

6.2 Structural characterization of 1T” MoS_2

The 1T-MoS_2 samples were prepared by the lithiation of the multilayer 2H-MoS_2 nanosheets with thicknesses ranging from 5 to 20 nm deposited on conductive Pt/SiO_2/Si substrates [32, 33]. Observation of the color change of the lithiated flakes provides preliminary verification of the intended 2H phase conversion to the 1T phase, which has darker color [Fig. 6.1a] [Data courtesy: Alexey Lipatov for synthesis and structural characterization of 1T”-MoS_2 flakes in Figs. 6.1a-e]. The emergence of additional Raman peaks at 155, 225, 289, and 328 cm^{-1} corresponding to the J_1, J_2, E_{1g}, and J_3 modes of the 1T phase further confirms the transition from the 2H to the 1T phase [31, 34, 35, 36, 37]. To perform high-resolution structural characterization, the pristine and lithiated MoS_2 flakes were transferred on a transmission electron microscopy (TEM) grid. As expected, selected area electron diffraction (SAED) patterns (acquired from the regions of several hundred nanometers in the lateral dimensions) show a significant difference between the two phases [Fig. 6.1b,c]. While the 2H-MoS_2 flakes exhibit a hexagonal arrangement of bright reflection spots in the SAED pattern [Fig. 6.1b], the emergence of the superstructure spots can be seen in SAED of the lithiated MoS_2 flakes, which corresponds to the doubling of the unit cell parameters [Fig. 6.1c]. This pattern is indicative of the formation of the 1T’’ phase [Fig. 6.1d], one of the distorted variants of 1T-MoS_2, which has ~$2a_o$×$2a_o$ superstructure, where a_o is the lattice parameter of 2H-MoS_2 [38]. The uniform appearance of the lithiated flakes in TEM [Fig. 6.1e] confirms a complete transformation of the pristine flake to the 1T”-MoS_2 phase. This experimentally established 1T” phase formation is further verified by image simulation, which shows perfect matching of the theoretical diffraction patterns with the experimental SAED images [Figs. 6.1b,c]. The experimental and simulated SAED patterns for other MoS_2 polymorphs can be found in Appendix A. The first-principles calculations of 1T”-MoS_2 [31], carried out both for monolayer and bulk cases confirm the ferroelectric nature of this structural phase. The 1T”-MoS_2 phase features a distorted octahedral unit cell [see Fig. 6.1d and Appendix A] with an out-of-plane dipole moment. Specifically, the in-plane displacement of certain Mo atoms results in a periodic sublattice of Mo trimers centered at S atoms (termed here as “polar”) embedded into a S-Mo-S matrix with atoms located near their ideal positions in the undistorted octahedral structure [34]. Due to the reduced distance between the trimerized Mo atoms, the polar S atoms [marked by the dashed blue circles in Fig. 6.1d], as well as those bridging the trimers [marked by the dashed red circles in Fig. 6.1d] are pushed up from their original positions to maintain their bond lengths to the shifted Mo atoms. This vertical displacement of the S atoms is tantamount to the occurrence of an out-of-plane polarization. Furthermore, the electronic band structures calculation reveals a sizeable value of the dipole moment (0.04 $\mu C\ cm^{-2}$) for an isolated monolayer [31]. Interestingly, the obtained sign for the polarization [Fig. 6.1d] is opposite to what one would expect from the polar ionic displacements: the polarization is aligned in the direction of the visible S anion shift, instead of being opposite to it.

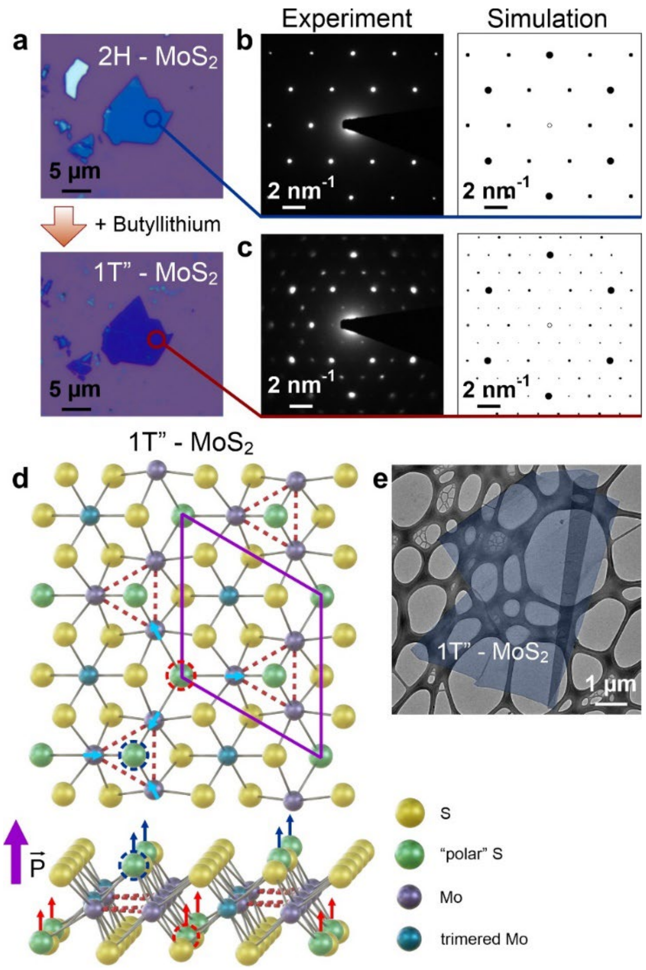

Figure 6.1: Synthesis and structural characterization of 1T”-MoS_2 flakes. (a) MoS_2 flake on Si/SiO_2 substrate before and after the treatment with *tert*-butyllithium. (b,c) Experimental SAED patterns of the MoS_2 flakes before (b) and after (c) the lithiation treatment and the corresponding theoretical SAED patterns constructed using the calculated atomic positions in the unit cell with the trigonal symmetry (see Appendix A). The SAED patterns in (b) and (c) correspond to 2H-MoS_2 and 1T”-MoS_2 phases, respectively. (d) Atomic structure of 1T”-MoS_2 (upper panel - top view, lower panel - side view). A unit cell is marked by the purple rhombus in the upper panel. Arrows in the upper panel illustrate the displacements of the Mo atoms forming trimers (marked by dashed triangles). The Mo and S atoms located close to the ideal positions in the undistorted 1T-

MoS_2 structure are shown as blue and yellow spheres, respectively. Arrows in the lower panel illustrate the vertical displacements of the polar sulfur atoms in the centers of the trimers and sulfur atoms bridging the trimers (marked by the dashed blue and red circles, respectively) from their ideal positions. Vertical displacement of the S atoms results in the emergence of an out-of-plane polarization. (e) TEM image of a representative 1T"-MoS_2 flake (shown in blue for clarity) on a lacey carbon TEM grid. [Data Courtesy: Alexey Lipatov for Figs. 6.1a-e]. This figure is taken from reference [31].

6.3 Flexoelectric control of polarization in 1T" MoS_2

The experimental testing of the polar state of 1T"-MoS_2 has been carried out by measuring the electromechanical response of the flakes by PFM. The flake thickness in these studies is in the range from 5 nm to 20 nm. Figures 6.2a-c show the topography of a representative as-prepared (pristine) 8-nm-thick 1T"-MoS_2 flake along with its corresponding PFM amplitude and phase images. Although the PFM amplitude exhibited by this particular sample is rather weak, a number of other pristine 1T"-MoS_2 flakes exhibit the PFM amplitude signal that is about 3-4 times above the noise level [Fig. 6.3b] providing initial evidence of the robust electromechanical activity and a polar state of pristine 1T"-MoS_2. Yellow color in the PFM phase image [Fig. 6.2c] represents an "in-phase" electromechanical response to a sensing ac field (i.e. an increase in the sample thickness for a positive half of the applied ac bias cycle, and sample thickness decrease for negative half of the ac bias cycle) and corresponds to the downward polarization direction (toward the substrate).

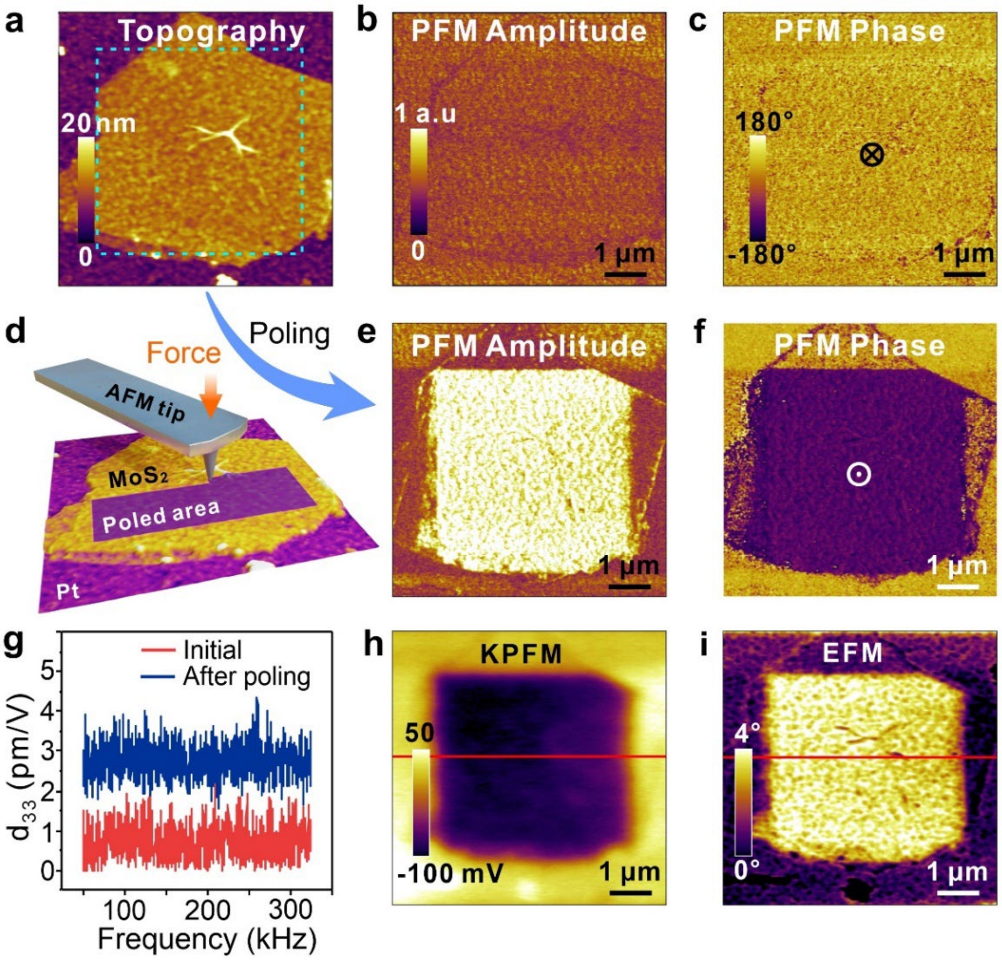

Figure 6.2: Probing the electromechanical and electrical properties of 1T"-MoS_2. (a) Topographic image of the pristine 8-nm-thick flake. The dashed line represents the 5×5 μm^2 region that subjected to a mechanical load of 1100 nN. (b,c) PFM amplitude (b) and phase (c) images of the pristine 1T"-MoS_2 flake. (d) Schematics of an experiment on application of mechanical stress by a PFM tip. (e,f) PFM amplitude (e) and phase (f) images of the same 1T"-MoS_2 flake after application of mechanical stress. (g) The frequency-dependent piezoelectric response acquired by LDV in the pristine and mechanically-poled regions of the 1T"-MoS_2 flake. (h,i) KPFM (h) and EFM (i) maps of the 1T"-MoS_2 flake after application of mechanical stress. A bright region in the EFM phase image (i) acquired with a dc read bias of +3V corresponds to the negative surface charge, which is further

corroborated by the reduced contact potential difference in the same region seen in the KPFM image (h). This figure is taken from reference [31].

A natural next step in establishing the ferroelectric properties of 1T”-MoS_2 would be the investigation of its polarization response under an applied electric field [39]. However, high electrical conductance of 1T”-MoS_2 (note the metallic ground state of bulk 1T”-MoS_2 predicted by our DFT calculations [31]) precludes the use of this standard approach. On the other hand, it has been previously demonstrated that strain gradients can play a role of an effective electric field due to the flexoelectric effect [40]. Hence, highly concentrated non-uniform stress produced by the PFM tip pressed against the sample surface [Fig. 6.2d] can be used as an efficient tool for polarization reversal in highly conductive MoS_2 samples, thereby eliminating the need for electric field application. The outcome of this approach is illustrated in Figs 6.2e,f. Scanning a 5x5 µm2 area with the PFM tip under an applied load of 1100 nN (well above the 100 nN load used during conventional PFM measurements) results in an enhanced PFM amplitude signal [Fig. 6.2e] and PFM phase reversed by 180^o [Fig. 6.2f], which is a strong indication of the robust polarization switched by the tip-induced mechanical stress. Topographic imaging does not show any sample damage and only minor (about 0.5 nm) depression on the flake surface subjected to stress. The switched polarization state is highly stable as the PFM amplitude and phase signals monitored over a period of several weeks did not show any significant decay. It is worth mentioning that the observed effect is independent of the type of substrate material as it has been observed in the flakes on Pt, Au, and $La_{0.67}Sr_{0.33}MnO_3$ electrodes [Figure 6.3]. Furthermore, it becomes evident from Figure 6.3 that some pristine 1T” MoS_2 flakes exhibit PFM amplitude signal that is comparable to that after mechanical poling and is well above the noise level suggesting a robust polarization in pristine 1T" MoS_2 flake [Fig. 6.3b]. Also, it can be inferred that mechanically-induced switching could be effective in flakes with thickness of up to 30 nm [Figs. 6.3d-f]. For reference, the same mechanical switching approach has been applied to the non-polar semiconducting allotrope of molybdenum disulphide with hexagonal symmetry, 2H-MoS_2 [Fig. 6.4]. Notably, no change in the PFM response has been observed indicating that the induced switching seen in Figure 6.2e,f is inherently related to the ferroelectric nature of 1T"-MoS_2.

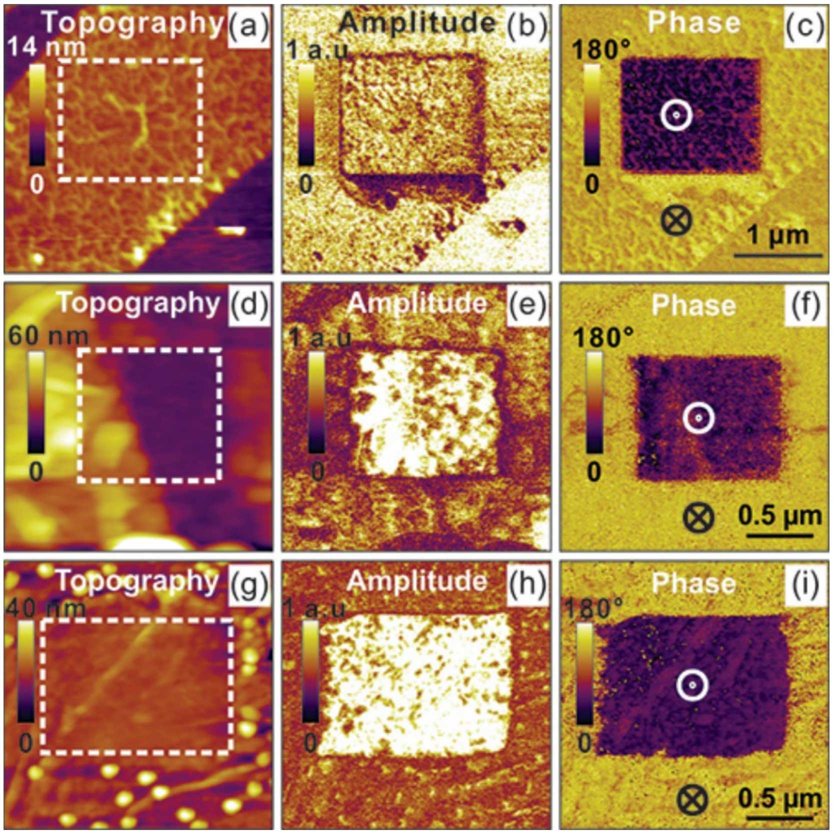

Figure 6.3: Mechanical switching observed in 1T"-MoS_2 flakes deposited on different substrates: Pt/SiO_2/Si (a-c), Au/SiO_2/Si (d-f), and $La_{0.67}Sr_{0.33}MnO_3$/$SrTiO_3$ (g-i). (a) Topographic image of the 6-nm-thick 1T''-MoS_2 flake on the Pt/SiO_2/Si substrate. The white dashed box indicates a region subjected to the loading force of 1.1 µN by the

scanning tip. (b,c) PFM amplitude (b) and phase (c) images of the flake after application of mechanical pressure. (d) Topographic image of the 1T” MoS_2 flake on the $Au/SiO_2/Si$ substrate showing a topographic step of about 15 nm. The brighter area on the left corresponds to the flake thickness of 28 nm and the darker area on the right indicates the thickness of 13 nm. The white dashed box indicates the region subjected to the loading force of 1.8 μN by the scanning tip. (e,f) PFM amplitude (e) and phase (f) images of the flake after application of the tip-induced mechanical pressure. (g) Topographic image of the 12-nm-thick 1T’’-MoS_2 flake on the $La_{0.67}Sr_{0.33}MnO_3/SrTiO_3$ substrate. The white dashed box indicates a region subjected to the loading force of 1.8 μN by the scanning tip. (h,i) PFM amplitude (h) and phase (i) images of the flake after application of mechanical pressure. This figure is taken from reference [31].

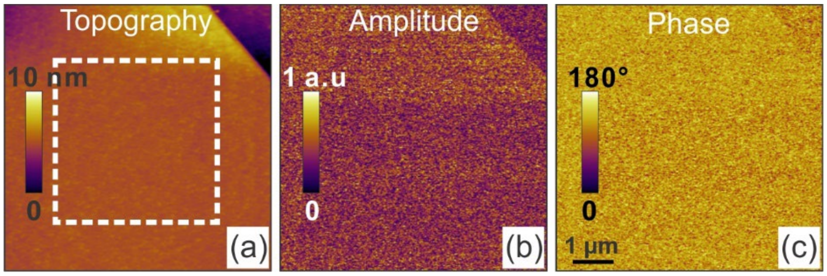

Figure 6.4: PFM probing of the tip-induced pressure effect in the 2H-MoS_2 flake. (a) Topographic image of the 7.5-nm-thick flake on the $Pt/SiO_2/Si$ substrate. The white dashed box indicates the region subjected to the loading force of 1.1 μN by the scanning tip. (b,c) PFM amplitude (b) and phase (c) images of the flake after application of the tip-induced mechanical pressure. This figure is taken from reference [31].

Further characterization of 1T”-MoS_2 with respect to its ferroelectric behavior involved testing of the mechanically-switched state by a set of complementary local probe microscopy techniques. Results of the application of Laser Doppler Vibrometer (LDV) spectroscopy, which enables quantitative measurements of the piezoelectric response by direct measurements of the cantilever displacement in PFM experiments [41], are shown in Fig. 6.2g. It is seen that while the pristine area of the 1T”-MoS_2 flake exhibits a measurable piezoelectric coefficient d_{33} of 0.7 ± 0.4 pm/V (which is slightly above the noise level of 0.3 pm/V), the mechanically poled region is characterized by a much higher d_{33} value of 2.8 ± 0.4 pm/V [31].

6.4 Electrical Characterization

To further corroborate the stress-induced switching of polarization in 1T”-MoS_2, electrical characterization of the 1T”-MoS_2 flakes were performed using scanning probe microscopy in different operating modes such as Kelvin probe force microscopy (KPFM), and electrostatic force microscopy (EFM) [See Chapter 2 for details]. Typically, in the case of perovskite ferroelectrics, such as $BaTiO_3$, the strain gradient due to the tip pressure switches polarization from the upward to the downward direction (Appendix B) [42]. However, 1T”-MoS_2 displays an opposite response: KPFM reveals a potential drop of 0.12 V in the region subjected to the tip-induced stress (as opposed to the potential increase in $BaTiO_3$ shown in Appendix B), which can be attributed to the negative screening charges compensating the bound charges of the upward polarization. EFM imaging [Fig. 6.2i] of the same region also shows a contrast change consistent with the upward polarization corroborating the KPFM results. The KPFM/EFM data are in agreement with the PFM phase results [Fig. 6.2f]. Overall, these findings indicate that the tip pressure switches 1T”-MoS_2 to the upward polarization state, i.e. opposite to that in perovskite ferroelectrics. This effect, which requires further investigation, might be related either to the anomalous behavior of polarization in 1T”-MoS_2, where the induced polarization is pointing in the same direction as the displacement of S anions rather than opposite to it, or to the negative value of the flexoelectric coefficient.

Based on the obtained structural data, computational modeling, and SPM characterization results, it is evident that pristine 1T”-MoS_2 exhibits a switchable polar state, i.e., 1T”-MoS_2 is ferroelectric. To explain a relatively weak PFM amplitude signal intermittently encountered in some pristine 1T”-MoS_2 samples, we performed additional testing experiments on the flakes that have been flipped over [Fig. 6.5a] [31]. It is natural to expect that after flipping a polarized pristine 1T”-MoS_2 flake would exhibit a different PFM phase contrast due to the reversed polarization direction, while its PFM amplitude signal would remain the same. However, the obtained results turned out to be more complicated than expected. Figure 6.5 shows two 1T”-MoS_2 flakes (#1 and #2) with the downward polarization in the pristine state [Fig. 6.5b] where the central regions were poled upward by the tip-induced mechanical stress [Fig. 6.5c]. After flipping them over, flake #1 exhibited the inverted PFM phase contrast corresponding to the upward polarization, while flake #2 still displayed the phase contrast consistent with the downward polarization [Fig. 6.5d]. Moreover, both flakes displayed a uniform phase contrast showing no traces of the mechanically poled regions. After the flakes had been flipped back, the previously poled regions were still present manifesting their remarkable stability against the changing chemical and mechanical boundary conditions [Fig. 6.5e].

These results can be understood if one assumes that oppositely polarized layers can coexist within a 1T”-MoS_2 flake, thus forming head-to-head (H-H) and tail-to-tail (T-T) dipole configurations [Fig. 6.5f], which we term as “antipolar.” From this point of view, the fact that, upon flipping, flake #2 exhibits unchanged PFM phase contrast with respect to the pristine state indicates that both the top and bottom layers in this flake exhibit inward polarization [Fig. 6.5h], while in flake #1 these layers are aligned in the same direction [Fig. 6.5g]. A stress gradient applied to the flake with the downward polarization is expected to induce switching to the upward state, but only in the topmost layers and not across the whole thickness of the flake, as the strain is concentrated in a small volume right underneath the pressing tip [42, 43]. It has been found that even flakes as thin as 5 nm could not be switched completely across their thickness, which explains the non-appearance of the poled regions in the thicker flipped flakes in Fig. 6.5d. Thicker flakes might have irregular combinations of the oppositely poled layers with H-H and T-T dipole configurations, which would explain a variability of the PFM amplitude signals in the pristine and poled 1T”-MoS_2 flakes. Furthermore, the existence of stable antipolar dipole configurations is also confirmed by the second harmonic generation (SHG) measurements [44], which reveal a significant difference between the signals from the pristine and mechanically poled regions in 1T”-MoS_2. A reduction in SHG intensity is observed in the mechanically poled area with respect to the surrounding region, which is consistent with an incomplete reversal of the polarization across the flake thickness: its lower SHG contrast is due to the destructive interference between the two π-shifted signals [31].

A coexistence of highly stable oppositely polarized layers in 1T”-MoS_2 requires additional consideration. The H-H and T-T interfaces should be charged due to the polarization discontinuity, i.e., $\nabla \cdot P \neq 0$. In conventional perovskite ferroelectric materials, such as $PbTiO_3$ or $BaTiO_3$, such charged domain walls are hard to obtain; however, they are frequently observed in ferroelectrics with a small value of spontaneous polarization and efficient electronic screening (for example, hexagonal manganites [45]). Since 1T”-MoS_2 displays a weak polarization and metallic conductivity along the stacking direction, it clearly belongs to the latter category. To verify the feasibility of the stable H-H and T-T dipole alignments, we performed first-principles calculations of the antipolar 1T”-MoS_2 [31]. It has been found that in the antipolar state, the individual MoS_2 monolayers retain their polarization. The calculated antipolar interface energy (an average of the H-H and T-T cases, as they appear in pairs in the periodically-repeated simulation supercell) is 18 mJ m^{-2}, which is very small compared to a typical value of the domain-wall energy in classic ferroelectric materials (for example, the energies of neutral domain walls commonly observed in $PbTiO_3$ range between 30 and 130 mJ m^{-2}) [46]. This result confirms that the antipolar H-H and T-T dipole alignments in 1T”-MoS_2 are thermodynamically stable.

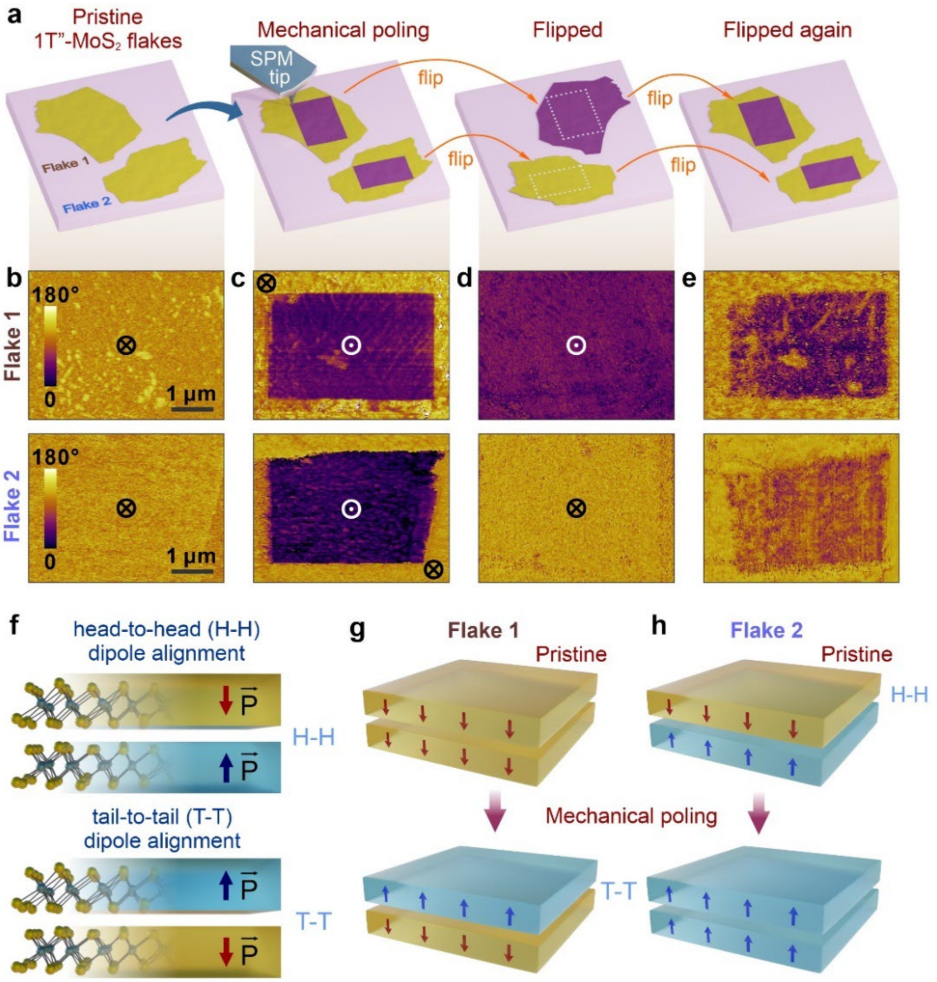

Figure 6.5: Observation of the PFM signals in the flipped 1T”-MoS$_2$ flakes. (a) Scheme of the experiment that involves mechanical poling and flipping of the flakes. (b) PFM phase images of two pristine 8-nm-thick 1T”-MoS$_2$ flakes with downward polarization. (c) PFM phase images of the same flakes after application of a mechanical load of 1100 nN to their central regions resulting in the switching to the upward polarization state. (d) PFM phase images of the same flakes after they were flipped over and placed on the same substrate. The entire flake #1 exhibits the upward polarization, while the entire flake #2 exhibits the downward polarization. (e) PFM phase images of the same flakes after they were flipped back to their original orientation. (f) Illustrations of the antipolar H-H and T-T dipole

alignments. (g,h) Schemes of the dipole alignments in flakes #1 and #2 in their pristine state and after mechanical poling corresponding to the experimental results shown in (b-e). [Data Courtesy: Alexey Lipatov for Figs. 6.5a,f]. This figure is taken from reference [31].

6.5 Conclusion

In summary, using a combination of the state-of-the-art synthesis, first-principles modeling, structural characterization, and SPM probing of the electromechanical properties, we have demonstrated the ferroelectric behavior of two-dimensional 1T”-MoS_2 - a polar metal with a switchable polarization. We have found unambiguous evidence of a stable antipolar structure consisting of oppositely polarized layers where polarization can be switched by tip-induced mechanical pressure due to the flexoelectric effect. The head-to-head and tail-to-tail dipole arrangements give rise to a wide variability of piezoresponse and associated electronic properties of 1T”-MoS_2 due to the formation of the charged interfaces between adjacent polar layers. The coexistence of switchable polarization and metallic conduction makes 1T”-MoS_2 a member of a handful of materials with this unique property. Overall, the experimental demonstration of ferroelectricity in 2D molybdenum disulphide opens new perspectives for the fundamental studies of this compound and enables new functionality, which could be exploited in novel electronic applications.

References

---

[1] B. Matthias, and A. von Hippel, Phys. Rev. **73**, 1378 (1948).

[2] A. Gruverman, O. Auciello, and H. Tokumoto, J. Vac. Sci. Technol. B **14**, 602 (1996).

---

[3] F. Zavaliche, S. Y. Tang, T. Zhao, Y. H. Chu, M. P. Cruz, C. B. Eom, and R. Ramesh, Phase Transit. **79**, 991 (2006).

[4] V. R. Palkar, S. C. Purandare, and R. Pinto, J. Phys. D: Appl. Phys. **32**. R1 (1999).

[5] X. Chen, X. Han, and Q. -D. Shen, Adv. Electron. Mater. **3**, 1600460 (2017).

[6] J. F. Scott, and C. A. Paz de Araujo, Science **246**, 1400 (1989).

[7] S. Mathews, R. Ramesh, T. Venkatesan, and J. Benedetto, Science **276**, 238 (1997).

[8] Y. Zhang, W. Jie, P. Chen, W. Liu, and J. Hao, Adv. Mater. **30**, 1707007 (2018).

[9] J. Junquera, and P. Ghosez, Nature **422**, 506 (2003).

[10] D. D. Fong, G. B. Stephenson, S. K. Streiffer, J. A. Eastman, O. Auciello, P. H. Fuoss, and C. Thompson, Science **304**, 1650 (2004).

[11] P. Gao, Z. Zhang, M. Li, R. Ishikawa, B. Feng, H. Liu, Y. Huang, N. Shibata, X. Ma, S. Chen, J. Zhang, K. Liu, E. Wang, D. Yu, L. Liao, Y. Chu, and Y. Ikuhara, Nat. Commun. **8**, 15549 (2017).

[12] S. R. Lee, L. Baasandorj, J. W. Chang, I. W. Hwang, J. R. Kim, J. Kim, K. Ko, S. B. Shim, M. W. Choi, M. You, C. Yang, J. Kim, and J. Song, Nano Lett. **19**, 2243 (2019).

[13] H. Wang, Z. R. Liu, H. Y. Yoong, T. R. Paudel, J. X. Xiao, R. Guo, W. N. Lin, P. Yang, J. Wang, G. M. Chow, T. Venkatesan, E. Y. Tsymbal, H. Tian, and J. S. Chen, Nat. Commun. **9**, 3319 (2018).

[14] C. Cui, F. Xue, W. -J. Hu, and L. -J. Li, npj 2D Mater. Appl. **2**, 18 (2018).

[15] S. N. Shirodkar, and U. V. Waghmare, Phys. Rev. Lett. **112**, 157601 (2014).

[16] W. Ding, J. Zhu, Z. Wang, Y. Gao, D. Xiao, Y. Gu, Z. Zhang, and W. Zhu, Nat. Commun. **8**, 14956 (2017).

---

[17] Y. Zhao, L. Lin, Q. Zhou, Y. Li, S. Yuan, Q. Chen, S. Dong, and J. Wang, Nano Lett. **18**, 2943 (2018).

[18] Q. Yang, W. Xiong, L. Zhu, G. Gao, and M. Wu, J. Am. Chem. Soc. **139**, 11506 (2017).

[19] M. Wu, J. D. Burton, E. Y. Tsymbal, X. C. Zeng, and P. Zena, Phys. Rev. B **87**, 081406 (2013).

[20] L. Li, and M. Wu, ACS Nano **11**, 6382 (2017).

[21] Z. Fei, W. Zhao, T. A. Palomaki, B. Sun, M. K. Miller, Z. Zhao, J. Yan, X. Xu, and D. H. Cobden, Nature **560**, 336 (2018).

[22] Y. Zhao, L. Lin, Q. Zhou, Y. Li, S. Yuan, Q. Chen, S. Dong, and J. Wang, Nano Lett. **18**, 2943 (2018).

[23] Y. Zhou, D. Wu, Y. Zhu, Y. Cho, Q. He, X. Yang, K. Herrera, Z. Chu, Y. Han, M. C. Downer, H. Peng, and K. Lai, Nano Lett. **17**, 5508 (2017).

[24] C. Zheng, L. Yu, L. Zhu, J. L. Colliins, D. Kim, Y. Lao, C. Xu, M. Li, Z. Wei, Y. Zhang, M. T. Edmonds, S. Li, J. Seidel, Y. Zhu, J. Z. Liu, W. -X. Tang, and M. S. Fuhrer, Sci. Adv. **4**, eaar7720 (2018).

[25] P. Sharma, F. -X. Xiang, D. -F. Shao, D. Zhang, E. Y. Tsymbal, A. R. Hamilton, and J. Seidel, Sci. Adv. **5**, 7 (2019).

[26] K. Chang, J. Liu, H. Lin, N. Wang, K. Zhao, A. Zhang, F. Jin, Y. Zhong, X. Hu, W. Duan, Q. Zhang, L. Fu, Q. -K. Xue, X. Chen, and S. -H. Ji, Science **353**, 6296 (2016).

[27] N. Higashitarumizu, H. Kawamoto, C. -J. Lee, B. -H. Lin, F. -H. Chu, I. Yonemori, T. Nishimura, K. Wakabayashi, W. -H. Chang, and K. Nagashio, Nat. Commun. **11**, 2428 (2020).

---

[28] F. Liu, L. You, K. L. Seyler, X. Li, P. Yu, J. Lin, X. Wang, J. Zhou, H. Wang, H. He, S. T. Pantelides, W. Zhou, P. Sharma, X. Du, P. M. Ajayan, J. Wang, and Z. Liu, Nat. Commun. **7**, 12357 (2016).

[29] L. You, F. Liu, H. Li, Y. Hu, S. Zhou, L. Chang, Y. Zhou, Q. Fu, G. Yuan, S. Dong, H. J. Fan, A. Gruverman, Z. Liu, and J. Wang, Adv. Mater. **30**, 1803249 (2018).

[30] S. S. Chou, N. Sai, P. Lu, E. N. Coker, S. Liu, K. Artyushkova, T. S. Luk, B. Kaehr, and C. J. Brinker, Nat. Commun. **6**, 8311 (2015).

[31] A. Lipatov, P. Chaudhary, Z. Guan, H. Lu, G. Li, O. Crégut, K. D. Dorkenoo, R. Proksch, S. C. Hertel, D. -F. Shao, E. Y. Tsymbal, J. Íñiguez, A. Sinitskii, and A. Gruverman, npj 2D Mater. Appl. **6**, 18 (2022).

[32] Y. Gip, D. Sun, B. Ouyang, A. Raja, J. Song, T. F. Heinz, and L. E. Brus, Nano Lett. **15**, 5081 (2015).

[33] C. H. Sharma, A. P. Surendran, A. Varghese, and M. Thalakulam, Sci. Rep. **8**, 12463 (2018).

[34] Y. Yu, G. -H. Nam, Q. He, X. -J. Wu, K. Zhang, Z. Yang, J. Chen, Q. Ma, M. Zhao, Z. Liu, F. -R. Ran, X. Wang, H. Li, X. Huang, B. Li, Q. Xiong, Q. Zhang, Z. Liu, L. Gu, Y. Du, W. Huang, and H. Zhang, Nat. Chem. **10**, 638 (2018).

[35] L. Liu, J. Wu, L. Wu, M. Ye, X. Li, Q. Wang, S. Hou, P. Lu, L. Sun, J. Zheng, L. Xing, L. Gu, X. Jiang, L. Xie, and L. Jiao, Nat. Mater. **17**, 108 (2018).

[36] C. Guo, J. Pan, H. Li, T. Lin, P. Liu, C. Song, D. Wang, G. Mu, X. Lai, H. Zhang, W. Zhou, M. Chen, and F. Huang, J. Mater. Chem. C **5**, 10855 (2017).

[37] D. Yang, S. J. Sandoval, W. M. R. Divigalpitiya, J. C. Irwin, and R. F. Frindt, Phys. Rev. B **43**, 12053 (1991).

---

[38] K. Chrissafis, M. Zamani, K. Kambas, J. Stoemenos, and N. A. Economou, Mater. Sci. Eng. B **3**, 145 (1989).

[39] A. Gruverman, M. Alexe, and D. Meier, Nat. Commun. **10**, 1661 (2019).

[40] H. Lu, C. -W. Bark, D. Esque de los Ojos, J. Alcala, C. B. Eom, G. Catalan, and A. Gruverman, Science **336**, 59 (2012).

[41] A. Labuda, and R. Proksch, Appl. Phys. Lett. **106**, 253103 (2015).

[42] J. Očenášek, H. Lu, C. W. Bark, C. B. Eom, J. Alcala, G. Catalan, and A. Gruverman, Phys. Rev. B **92**, 035417 (2015).

[43] H. Lu, B. Wang, T. Li, A. Lipatov, H. Lee, A. Rajpitamahuni, R. Xu, X. Hong, S. Farokhipoor, L. W. Martin, C. -B. Eom, L. -Q. Chen, A. Sinitskii, and A. Gruverman, Nano. Lett. **16**, 6460 (2016).

[44] J. Xio, H. Zhu, Y. Wang, W. Feng, Y. Hu, A. Dasgupta, Y. Han, Y. Wang, D. A. Muller, L. W. Martin, P. Hu, and X. Zhang, Phys. Rev. Lett. **120**, 227601 (2018).

[45] Q. N. Meier, M. Lilienblum, S. M. Griffin, K. Conder, E. Pomjakushina, Z. Yan, E. Bourret, D. Meier, F. Lichtenberg, E. K. H. Salje, N. A. Spaldin, M. Fiebig, and A. Cano, Phys. Rev. X **7**, 041014 (2017).

[46] J. Íñiguez (eds D. Meier, J. Seidel, M. Gregg, & R. Ramesh), *First-Principles Studies of Structural Domain Walls. in Domain Walls: From Fundamental Properties to Nanotechnology Concepts* (Oxford, New York, 2020).

Chapter 7

Summary and Outlook

7.1 Summary

This thesis summarizes the research works on the study of the polarization-dependent electronic transport behavior in the ferroelectric thin films, 2D materials, and their heterostructures using SPM techniques. In ferroelectrics, the spontaneous polarization, hysteretic reversal of polarization, and domain walls can facilitate the development of micro-and nano-electromechanical systems, ferroelectric random-access memory, memristors, and ferroelectric diodes. Similarly, the robust mechanical and optoelectronic properties of nanometer-thick 2D materials may have the potential for the development of light-weight and highly-dense information storage systems such as field-effect transistors and photonic devices. 2D/ferroelectric hybrid structures may reveal some interesting phenomena, such as giant electroresistance due to a cross-coupling between their material properties. In this respect, PFM, CAFM, KPFM, and EFM have proven to be indispensable tools, enabling the nanoscale studies of domain dynamics and electronic transport due to domain/domain wall conduction in ferroelectrics and the 2D/FE heterostructures, mapping of the local surface charges and the surface potential. Similarly, the sharp AFM probe acts as a nano-indenter, thus can generate a huge local strain gradient, enabling the studies of the flexoelectric phenomenon in any materials, either centrosymmetric or non-centrosymmetric. Chapter 1 focuses on the detailed introduction of the piezoelectric and the ferroelectric properties: piezoelectric strain loops, domains, and domain walls in ferroelectrics, polarization reversal and hysteresis, 2D TMDs such as

MoS_2, and some of their applications. Similarly, Chapter 2 provides a detailed description of PFM theory, DART-PFM, SSPFM, CAFM, KPFM, and EFM.

In Chapter 3, we have investigated the direct correlation between the polarization and the tunneling resistance in the ferroelectric HfO_2-based FTJs by employing semiconducting MoS_2 as a top electrode. The coupling between the polarization and the semiconducting properties of the MoS_2 has led to an observation of polarization-mediated enhanced tunneling electroresistance (TER) up to 10^3 measured at 0.8 V read bias. Specifically, the underlying mechanism for such TER is the polarization-induced accumulation or depletion of the majority carriers (electrons) at the $MoS_2/Hf_{0.5}Zr_{0.5}O_2$ interface that leads to a change in the effective barrier profile for the transport electrons. The conduction of the electrons across the $Hf_{0.5}Zr_{0.5}O_2$ barrier in these FTJs occurs through Fowler-Nordheim (F-N) tunneling.

In Chapter 4, we have shown that the conducting ferroelectric domain walls as functional elements in $LiNbO_3$ can facilitate the development of memristors, one of the types of resistive switching devices. We have presented two different approaches for the realization of the memristive functionality of the conducting domain walls in graphene/$LiNbO_3$/Pt capacitors. The first approach is the conventional method based on the manipulation of the perimeter of the conducting domain walls via partial polarization switching caused by the super-coercive bias. The high-energy cost of polarization reversal and the high leakage current makes this method deleterious. The second method is an alternative method based on tuning the domain wall conductance through the application of the non-switching sub-coercive bias to the capacitor set in a certain polydomain configuration. This alternative approach is a more reliable and feasible method in terms of the energy cost, device resilience, lifetime, accuracy, and reproducibility of the resistance control in graphene/$LiNbO_3$/Pt memristors.

In Chapter 5, we have demonstrated that in centrosymmetric 2D MoS_2, the resistive switching can be induced by the mechanical stress generated by the sharp probe of AFM. We have revealed that tip-induced strain and strain gradient can modify the energy barrier profile in tip/MoS_2/Pt junctions, resulting in the reversible tuning of the junction resistance by up to 4 orders of magnitude. Furthermore, we have highlighted that the tip-generated flexoelectric effect favors the significant enhancement of the photovoltaic effect in MoS_2 junctions.

Finally, in Chapter 6, we have experimentally demonstrated the observation of the stable room-temperature out-of-plane polarization in the 2D distorted trigonal 1T”-MoS_2. The switching of polarization from the downward direction to the upward direction is realized by the tip-induced strain gradient via the flexoelectric effect. The occurrence of the stable bidomain patterns is further corroborated by the electrical characterization of the surface potential and screening charges via KPFM and EFM. Moreover, from the PFM experiments performed over the flipped flakes, we have highlighted the possibility of coexistence of the oppositely polarized layers of 1T”- MoS_2, thus forming head-to-head and tail-to-tail dipole arrangements.

7.2 Outlook

7.2.1 Domain wall conductivity in 2D ferroelectrics

Scanning probe microscopy has led to a significant contribution toward the systematic studies of the charge transport properties of the domains and domain walls in ferroelectrics. PFM, in conjunction with CAFM, can be employed for the investigation of the presence of the charged domain walls and their conductivity in 2D ferroelectrics. As explained in chapter 4, it is seen that charged domain walls in ferroelectrics are not rigid conductors and their conductivity can be electrically tuned by changing the domain wall perimeter or changing the domain wall inclination angle relative to the polar axis that results in the memristive functionalities. Exploring the conducting domain walls in the 2D ferroelectrics may provide a possible pathway for the development of high-density multilevel data storage devices and information systems.

7.2.2 Flexoelectric effect in electrical transport in organic and inorganic halide perovskites

The universality of the flexoelectric effect, coupling between the polarization and the strain gradient, in any dielectric materials can be exploited to study the electrical transport and the photovoltaic properties of the centrosymmetric semiconducting halide perovskites (ABX_3: A, B are cations and X is halide anion). Halide perovskites have been shown to have superior performance and higher photovoltaic power conversion efficiency reaching up to 24% [1]. In Chapter 5 of this thesis, we have demonstrated that the tip-induced strain and strain gradient via flexoelectric effect modulates the barrier of MoS_2, leading to a decrease in resistance by 4 orders of magnitudes [2]. Using the same analogy, the centrosymmetric halide perovskites can be subjected to the mechanical pressure applied via the AFM tip that can induce a sufficiently large strain gradient, which eventually can break the local inversion symmetry inducing a local polarization in this material. The strain gradient may modify the carrier concentration, carrier mobility, or the band structures of the halide perovskites affecting the charge transport in halide perovskites. Investigation of the effect of the tip loading pressure on the bulk conductivity of the halide perovskites requires further studies. Also, in figure 5.4 of Chapter 5, it is shown that the flexoelectric field modifies the barrier profile of MoS_2 from an asymmetric to a symmetric barrier resulting in the transition of I-V curves from rectifying behavior at low tip load to a symmetric nature at high tip load. Also, the MoS_2 conductivity is further enhanced by 3 orders of magnitude due to the combined effects of tip-induced strain/strain gradient and optical illumination [2]. Moreover, the flexoelectric field may promote the separation of the photogenerated charge carriers when the halide perovskites are subjected to an optical illumination. A detailed exploration of the photovoltaic effect upon the simultaneous application of the mechanical pressure can be the next future direction of the research.

References

---

[1] E. Aydin, M. De Bastiani, and S. De Wolf, Adv. Mater. **31**, 1900428 (2019).

[2] P. Chaudhary, H. Lu, M. Loes, A. Lipatov, A. Sinitskii, and A. Gruverman, Nano Lett. **22**, 1047 (2022).

Appendices

Appendix A: MoS_2 polymorphs and SAED patterns

The easily changeable intralayer stacking structure of the S-Mo-S layers in MoS_2 gives rise to a variety of 2D MoS_2 polymorphs, which include semiconducting 2H [1] and semi-metallic 1T [2] phases. Figure A1 shows crystal structures of different MoS_2 polymorphs along with their simulated selected area electron diffraction (SAED) patterns. Simulations were performed using CrysTBox software [3]. The most thermodynamically stable 2H phase has a layered structure, in which Mo atoms are surrounded by six S atoms in a trigonal prismatic coordination [Fig. A1(a)]. In centrosymmetric 1T-MoS_2, the Mo atoms are coordinated with six S atoms in an ideal octahedral arrangement [Fig. A1(b)]. The 1T-MoS_2 phase is, however, unstable with respect to the Peierls distortion resulting in the formation of the monoclinic (distorted octahedral) 1T'-MoS_2 phase, which is characterized by Mo zigzag chains and S atoms arranging in deformed trigonal antiprisms around the Mo atoms [4]. The experimentally observed SAED diffraction pattern (Fig. A1(f)) matches the simulated pattern of the 1T"-MoS_2 phase, a distorted version of the 1T-MoS_2 phase with ~$2a_o \times 2a_o$ superstructure, where a_o is the lattice parameter of 2H-MoS_2.

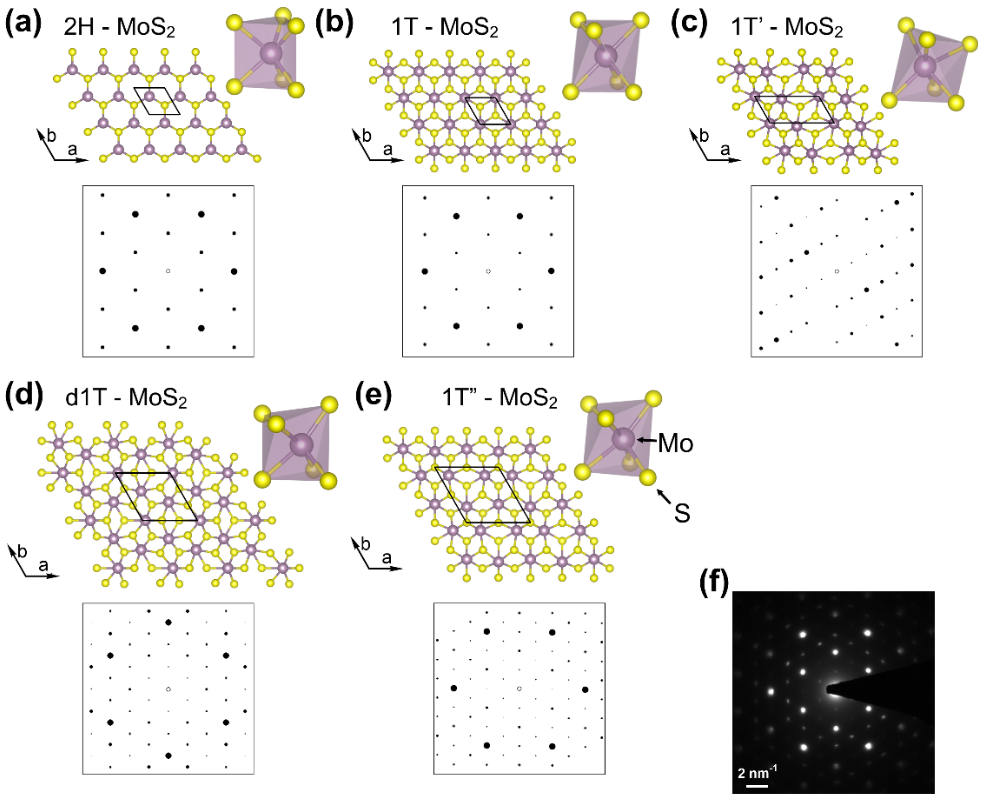

Figure A1: Comparison of crystal structures and reconstructed SAED patterns for different MoS_2 phases. (a) 2H-MoS_2; (b) 1T-MoS_2; (c) 1T'-MoS_2; (d) d1T-MoS_2; (e) 1T"-MoS_2. (f) Experimental SAED diffraction pattern for the MoS_2 flakes treated with *tert*-butyllithium used in this study matching the simulated pattern for the 1T"-MoS_2 phase. [Data Courtesy: Alexey Lipatov for Figs. A1 (a-f)]. This figure is taken from reference [5].

Appendix B: Reference testing of the mechanically-induced switching in $BaTiO_3$ thin films

To obtain reference data, the mechanical poling experiments using a set of scanning probe microscopy (SPM) techniques have been carried out in the archetype ferroelectric films of $BaTiO_3$ with a thickness of 4.8 nm and uniform upward polarization. A 1x1 μm^2 area of the film was scanned with the electrically grounded tip under a loading force of

1000 nN. After that, a larger area of 2x2 μm^2 has been imaged by conventional PFM with a low load of 30 nN [Figs. B1(a) and B1(b)] as well as by Kelvin probe force microscopy (KPFM) [Fig. B1(c)] and electrostatic force microscopy (EFM) [Fig. B1(d)]. PFM imaging reveals a change in the phase contrast from dark to bright [Fig. B1(b)]. This finding along with a stable and uniform PFM amplitude signal across the domain boundary in Fig. B1(a) indicates that tip-induced stress leads to a complete polarization reversal from the upward to the downward state in agreement with the earlier reported results [6]. A KPFM map Fig. B1(c) shows an elevated surface potential in the mechanically poled downward domain while the surface potential stays intact in the as-prepared region. At the same time, EFM reveals a reduced EFM phase signal in the mechanically switched region. The KPFM/EFM data are consistent with the presence of surface positive charges that screen the negative polarization bound charge of the mechanically switched region.

Comparison of the PFM/KPFM/EFM data obtained in the mechanically poled $BaTiO_3$ thin film with the corresponding data acquired in the mechanically poled 1T”-MoS_2 sample [Fig. 6.2] provides unambiguous evidence that the tip-induced stress results in the opposite polarization states in these two materials: downward polarization in $BaTiO_3$ thin film and upward polarization in the 1T”-MoS_2 flake. This ultimately infers a negative value of the flexoelectric coefficient in 1T”-MoS_2.

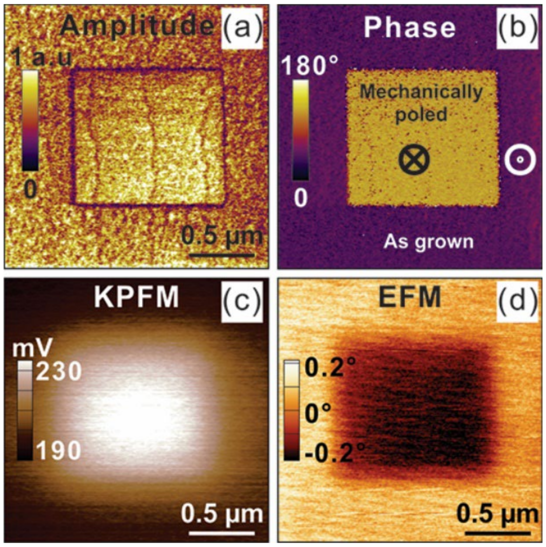

Figure B1: SPM electromechanical and electrical testing of mechanically poled $BaTiO_3$ thin film. (a,b) PFM amplitude and PFM phase images, respectively, obtained after application of a loading force by the probing tip. (c,d) KPFM (c) and EFM (d) maps of the same mechanically switched region. This figure is taken from reference [5].

References

---

[1] B. Radisavljevic, A. Radenovic, J. Brivio, V. Giacometti, and A. Kis, Nat. Nanotechnol. **6**, 147 (2011).

[2] R. Kappera, D. Voiry, S. E. Yalcin, B. Branch, G. Gupta, A. D. Mohite, and M. Chhowalla, Nat. Mater. **12**, 1128 (2014).

[3] M. Klinger, J. Appl. Crystallogr. **50**, 1226 (2017).

[4] Y. Zhou, D. Wu, Y. Zhu, Y. Cho, Q. He, X. Yang, K. Herrera, Z. Chu, Y. Han, M. C. Downer, H. Peng, and K. Lai, Nano Lett. **17**, 5508 (2017).

---

[5] A. Lipatov, P. Chaudhary, Z. Guan, H. Lu, G. Li, O. Crégut, K. D. Dorkenoo, R. Proksch, S. C. Hertel, D. -F. Shao, E. Y. Tsymbal, J. Íñiguez, A. Sinitskii, and A. Gruverman, npj 2D Mater. Appl. **6**, 18 (2022).

[6] L. You, F. Liu, H. Li, Y. Hu, S. Zhou, L. Chang, Y. Zhou, Q. Fu, G. Yuan, S. Dong, H. J. Fan, A. Gruverman, Z. Liu, and J. Wang, Adv. Mater. **30**, 1803249 (2018).